UNIVERSITAT POLITÈCNICA DE VALÈNCIA

TELECOM ESCUELA TÉCNICA VLC SUPERIOR DE INGENIERÍA DE TELECOMUNICACIÓN

Image-Based Assessment of the Modulation Transfer Function of Optical Remote Sensing Instruments

Sergio Pérez-López

Supervisor: Luis Guanter

Master thesis presented at the Escuela Técnica Superior de Ingenieros de Telecomunicación of the Universitat Politècnica de València, to obtain the Master's Degree in Telecommunications Engineering

Year 2019-20

Valencia, 25th March of 2020

Resumen

Los satélites con instrumentos ópticos pasivos son ampliamente utilizados para la teledetección de la superficie terrestre, con aplicaciones que abarcan desde la cartografía hasta la monitorización de recursos naturales. Los componentes ópticos que componen el sensor producen imágenes de la radiación solar reflejada por la superficie terrestre en diferentes canales espectrales entre 400 y 2500 nm. La calidad de las imágenes obtenidas depende de la respuesta espectral, radiométrica y espacial del instrumento. En este último caso, la respuesta espacial determina la resolución espacial de las imágenes, y viene definida por la función de transferencia de modulación (MTF, por sus siglas del inglés). En este trabajo se han implementado dos métodos para la evaluación de la MTF del instrumento a partir de las imágenes captadas por satélite. Uno de los métodos permite estimar la MTF utilizando transiciones abruptas de brillo, mientras que el otro utiliza elementos con forma de pulso identificados en la imagen, como por ejemplo los puentes. Una vez validado el funcionamiento de ambos algoritmos mediante simulaciones y el *Reference Dataset* proporcionado por el *Committee on Earth Observation Satellites* (CEOS), se han realizado estimaciones de la MTF del instrumento *Multispectral Imager* de la misión Sentinel-2 de la Agencia Espacial Europea. Los resultados obtenidos son similares a los publicados en los *Data Product Quality Report* oficiales de la agencia. Finalmente, se ha estimado el efecto que tiene en la calidad de la imagen la corrección geométrica aplicada a los datos de Sentinel-2 recibidos por los usuarios.

Resum

Els satèl.lits amb instruments òptics passius són àmpliament utilitzats per a la teledetecció de la superfície terrestre, amb aplicacions que abasten des de la cartografia fins a la monitorització de recursos naturals. Els components òptics que componen el sensor produeixen imatges de la radiació solar reflectida per la superfície terrestre en diferents canals espectrals entre 400 i 2500 nm. La qualitat de les imatges obtingudes depèn de la resposta espectral, radiomètrica i espacial de l'instrument. En aquest últim cas, la resposta espacial determina la resolució espacial de les imatges, i ve definida per la funció de transferència de modulació (MTF, per les seues sigles de l'anglès). En aquest treball s'han implementat dos mètodes per a l'avaluació de la MTF de l'instrument a partir de les imatges captades per satèl.lit. Un dels mètodes permet estimar la MTF utilitzant transicions abruptes de brillantor, mentre que l'altre utilitza elements amb forma de pols identificats en la imatge, com per exemple els ponts. Una vegada validat el funcionament dels dos algoritmes mitjançant simulacions i el *Reference Dataset* proporcionat pel *Committee on Earth Observation Satellites* (CEOS), s'han realitzat estimacions de la MTF de l'instrument *Multispectral Imager* de la missió Sentinel-2 de l'Agència Espacial Europea. Els resultats obtinguts són similars als publicats en els *Data Product Quality Report* oficials de l'agència. Finalment, s'ha estimat l'efecte que té en la qualitat de la imatge la correcció geomètrica aplicada a les dades de Sentinel-2 rebuts pels usuaris.

Abstract

Satellites with passive optical sensors are widely used for remote sensing of the Earth's surface, with applications ranging from cartography to the monitoring of natural resources. The optical

components of the sensor generate images of the reflected solar radiation by the Earth's surface in different spectral channels between 400 and 2500 nm. The quality of the resulting images is defined by the instrument spectral, radiometric, and spatial responses. In the later case, the spatial response conditions the spatial resolution of the images, and it is defined by the Modulation Transfer Function (MTF). In this work, two methods to assess the MTF of the optical instrument using in-flight satellite images are implemented. On of them allows to estimate the MTF response from sharp contrast edges, while the other uses pulse targets identified within the image. Once the performance of both algorithms is validated with ideal simulations and the Reference Dataset provided by the Committee on Earth Observation Satellites (CEOS), MTF estimations of the European Space Agency Sentinel-2 Multispectral Imager are carried out. The obtained results are similar to those reported at the official Data Product Quality Report of the agency. Finally, the effect of the geometric correction on the final spatial quality of the image has been analyzed for Sentinel-2 images.

Contents

List of Figures

List of Tables

Chapter 1

Introduction

1.1 Remote sensing

Remote sensing can be defined as the measurement of object properties on the Earth's surface using data acquired form aircraft and satellites [1, 2], that is, retrieving information about objects or phenomena at a distance. This information can be used in many applications in various fields, including geography, agriculture, climate change studies, meteorology, and military surveillance. Since the measuring instrument is not in physical contact with the object of interest, the information has to be obtained from some kind of electromagnetic waves. In this work, we are going to focus on the optical waves, ranging from 400 to 2500 nm, as optical remote sensing is the most widely used technology for Earth observation. The information retrieved from the surface of the Earth can be used to monitor short and long-term changes and the impact of mankind activities. This information can be used in many applications in various fields, including geography, agriculture, climate change and global warming, meteorology, and military surveillance.

Optical instruments on Earth observation satellites have several to hundreds of so-called spectral channels at which images of the Earth's surface are produced. Evaluating what wavelengths are absorbed by a specific object, it is possible to gain information on its composition. The modern era of optical remote sensing began when the USA launched the first Landsat Multispectral Scanner System (MSS), in 1972 [1, 3]. Landsat 1 had 4 spectral bands with a spectral resolution of 100 nm and a pixel size of 80 m. From that moment on, many new remote sensing missions have been deployed, with increasingly better spectral and spatial resolution coverage.

1.2 Earth observation using passive optical sensors

The reflectance spectrum in the region from 400 to 2500 nm (which includes visible, near infrared and short wave infrared bands, as shown in Table 2.1) can be used to identify a large range of surface cover materials [4]. This identification is possible because many common materials have characteristic absorption features that are 20-40 nm wide at half the band depth.

The main radiation source in the V, NIR and SWIR bands is the solar radiation. Passive optical sensors of remote sensing satellites take advantage of the solar radiation reflected from the Earth to retrieve information of the Earth's surface. The Sun nearly behaves as a blackbody radiator, which

Band name	Wavelength range
Visible (V)	400-700 nm
Near InfraRed (NIR)	700-1100 nm
Short Wave InfraRed (SWIR)	1100-2500 nm

Table 1.1: Spectral bands in the 400-2500 nm spectra.

means that the spectral radiant exitance, M_λ, can be modeled by Planck's blackbody equation [1, 2]:

$$M_\lambda = \frac{C_1}{\lambda^5 \left(e^{\frac{C_2}{\lambda T}} - 1\right)}, \tag{1.1}$$

where T is the blackbody temperature in Kelvin, $C_1 = 3.74151 \cdot 10^8$ $\text{Wm}^{-2}\mu\text{m}^{-4}$, $C_2 = 1.43879 \cdot 10^4$ μmK and λ is the wavelength in μm. Empirical measurements show that a blackbody temperature of $T \cong 5900$ K is a good approximation to model M_λ in the case of the Sun.

The spectral radiant exitance represents the power per unit area of the surface of the Sun, per unit of wavelength, and it is measured in $\text{Wm}^{-2}\mu\text{m}^{-1}$. The spectral irradiance that reaches the Earth, E^0_λ, can be calculated by propagating M_λ, that is,

$$E^0_\lambda = \frac{M_\lambda}{\pi} \cdot \frac{\text{Area of the solar disk}}{(\text{Distance to Earth})^2}, \tag{1.2}$$

which has units of spectral flux density, $\text{Wm}^{-2}\mu\text{m}^{-1}$.

From the incident radiation E^0_λ, there are three main reflected and scattered contributions that affect the optical detectors of remote sensing instruments. These contributions are:

- L^{su}_λ, which represents the unscattered surface reflected radiation.
- L^{sd}_λ, which corresponds to the down-scattered surface reflected radiation.
- L^{sp}_λ, which represents the up-scattered radiation from the atmosphere.

1.2.1 Unscattered surface reflected radiation – L^{su}_λ

The unscattered surface reflected radiation represents the main contribution to the final radiance detected at the optical sensor of the satellite, as it is caused by a direct reflection of the incident irradiance at theEarth's surface, as shown in Figure 1.1(a). The spectral flux density that reaches the Earth's surface, E_λ, is influenced by the atmosphere. This influence is modeled as a transmittance function $\tau_d(\lambda)$, which represents the fraction of incident radiation that goes trough the atmosphere. In addition, the spectral irradiance at the Earth's surface also depends on the angle of incidence, θ, measured from the incident path to the normal direction of the Earth's surface. Therefore, E_λ can be calculated as

$$E_\lambda = \tau_d(\lambda) E^0_\lambda \cos(\theta). \tag{1.3}$$

When the incident irradiance finally reaches the surface of the Earth, it is reflected and then influenced again by the atmosphere until it finally reaches the optical instrument of the remote

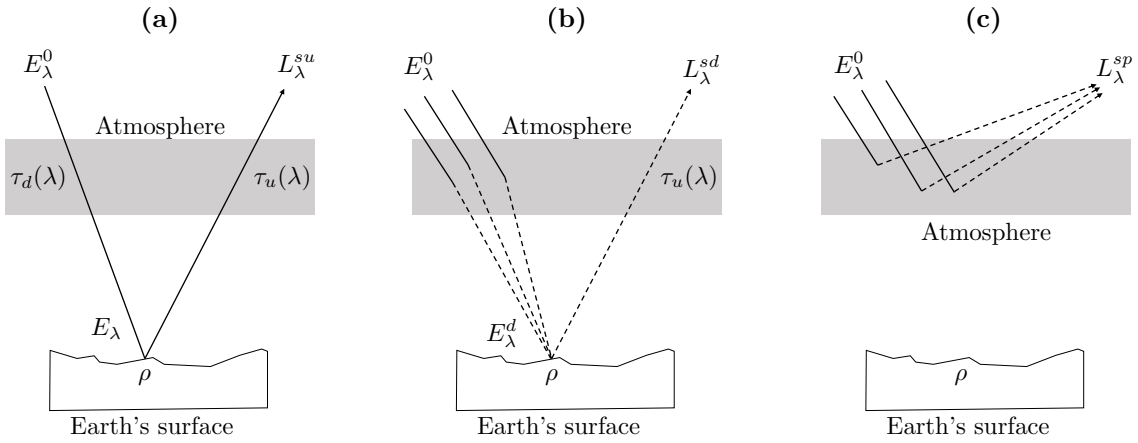

Figure 1.1: Scheme of the three main radiation contributions: (a) Unscattered surface reflected radiation, (b) down-scattered surface reflected radiation, and (c) up-scattered radiation from the atmosphere.

sensing satellite. If the surface is assumed to be Lambertian, that is, it provides an isotropic radiance reflection [1, 5, 6], the surface radiance can be finally calculated as

$$L_\lambda^{su} = \rho(\lambda)\frac{\tau_u(\lambda)\tau_d(\lambda)}{\pi}E_\lambda^0\cos(\theta), \tag{1.4}$$

with $\tau_u(\lambda)$ being the atmosphere transmittance in the Earth-sensor path and $\rho(\lambda)$ the diffuse surface spectral reflectance. The surface radiance is measured in $\mathrm{Wm}^{-2}\mathrm{srad}^{-1}\mu\mathrm{m}^{-1}$.

For remote sensing applications, the signal of interest is the surface reflectance, $\rho(\lambda)$, which depends on the surface material. Different materials have different reflectance responses as a function of the wavelength, which allows the remote identification of the material composition from its spectral signature. To showcase this phenomenon, Figure 1.2 depicts reflectance spectra for four different materials: green vegetation, soil, kaolinite and water. As it can be observed from the figure, all the materials have distinctive absorption features that allow for their identification and classification.

1.2.2 Down-scattered surface reflected radiation – L_λ^{sd}

The optical instrument of the satellite detects, in addition to unscattered reflected radiance, radiance down-scattered from the atmosphere to the surface of the Earth and then reflected to the satellite sensor. This case corresponds to the situation depicted at Figure 1.1(b). The down-scattered radiation is often known as "skylight". The skylight reflected radiance, L_λ^{sd}, can be calculated as

$$L_\lambda^{sd} = F\rho(\lambda)\frac{\tau_u(\lambda)}{\pi}E_\lambda^d, \tag{1.5}$$

where F represents a shape factor due to obstruction of terrain slope or adjacent objects and E_λ^d corresponds to the Earth's surface irradiance due to skylight.

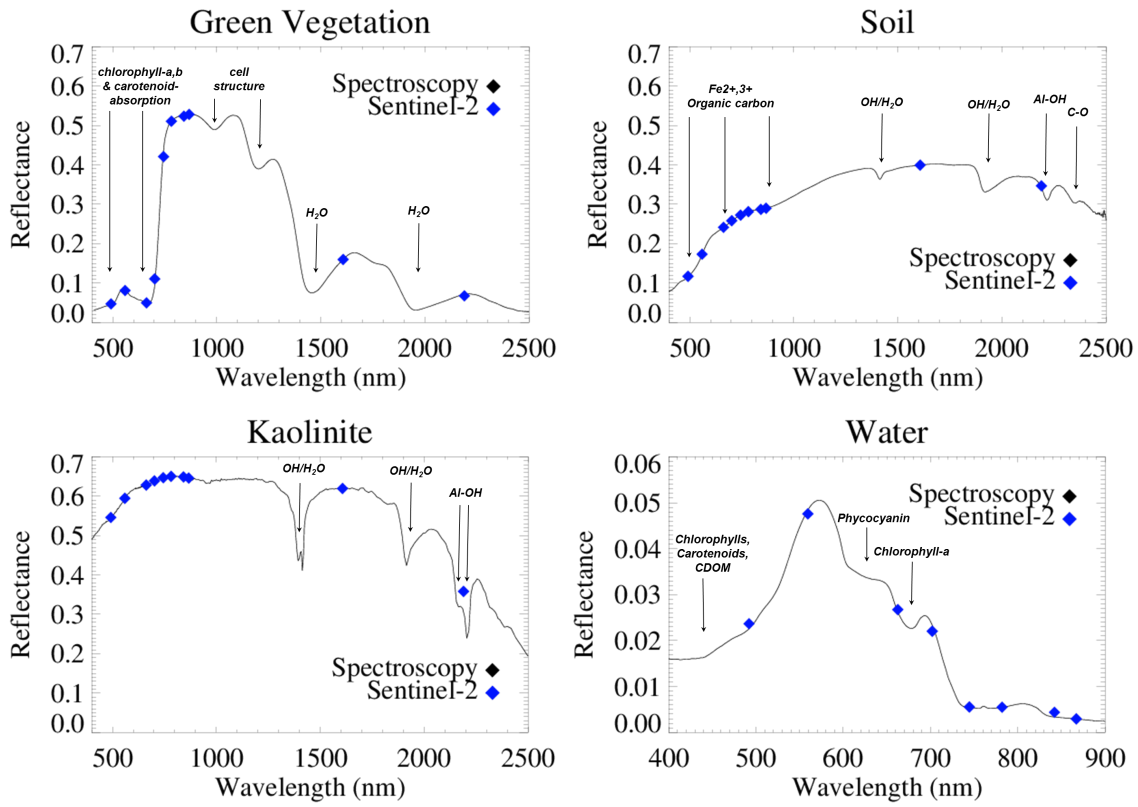

Figure 1.2: Reflectance as a function of the wavelength for green vegetation, soil, kaolinite and water. Black solid lines correspond to spectroscopy (continuous 10-nm spectral sampling), while blue dots corresponds to the spectral resampling of the spectroscopy case to the spectral response of Sentinel-2 Multispectral Imager. (Image extracted from [7]).

1.2.3 Up-scattered radiation from the atmosphere – L_λ^{sp}

The last of the three main contributions to the detected radiance at the satellite sensor is the up-scattered radiation from the atmosphere, which corresponds to Figure 1.1(c) scenario. The up-scattered radiation is generated by a combination of Rayleigh scattering and Mie scattering in molecules with different sizes present at the atmosphere [1, 6]. Empirical measurements show that for homogeneous scenes the up-scattered radiance, L_λ^{sp}, can be approximately assumed to be constant.

1.2.4 Total radiance at the optical sensor – L_λ^{s}

In remote sensing satellites, the surface reflectance is estimated from measured radiance values at the optical instrument. The final radiance contribution at the sensor can be calculated as the sum of the three main components described above, that is,

$$L_\lambda^s = L_\lambda^{su} + L_\lambda^{sd} + L_\lambda^{sp} = \rho(\lambda)\frac{\tau_u(\lambda)}{\pi}\left(\tau_u(\lambda)E_\lambda^0\cos(\theta) + FE_\lambda^d\right) + L_\lambda^{sp}. \tag{1.6}$$

1.3 Main parameters of passive remote sensing data

Each pixel of the resulting spectral image of the satellite is generated at the optical sensor as a result of integrating the reflected scene radiance, L^s_λ, along three dimensions, including time, space, and wavelength. The effect of the integration along time dimension can be usually neglected, as integration times are very low. In contrast, the spatial and wavelength integrations play a very important role in the final quality of the image, as they define important parameters, such as spatial and spectral resolution.

Remote sensing satellites with optical sensor payloads generate three dimensional images of the Earth's surface radiance as a function of (x,y,λ), with (x,y) being spatial coordinates and (λ) the spectral coordinate. This means that the satellite generates one 2D image for each one of the spectral channels it samples. As a result of the integration along the spatial axis, each (x,y) pixel of the image does not only contain information about that specific spatial point, but it also includes information about surrounding points. This fact is a consequence of the spatial resolution of the sensor, given by the sensor Point Spread Function (PSF), which will be discussed in later chapters. Similarly, for a given (x,y,λ) pixel, the spectral information contains information not only of the center wavelength (λ) of the detector, but also about contiguous wavelengths, depending on the spectral response of the detector.

1.3.1 Spatial resolution

The grid of (x,y,λ) pixels of the spectral image is generated as a combination of scanning in both along-track and across-track directions. The along-track axis represents the direction aligned to the satellite motion, while the across-track axis is defined perpendicular to the satellite motion. There are three main scanning methods:

- **Line scanner**: a single detector is used to scan all the scene. The satellite requieres moving parts to scan an entire line along the across-track axis.
- **Whiskbroom scanner**: an array of detectors aligned along-track is used to achieve parallel scanning in the across-track axis. The satellite requieres moving parts to perform the scan in the across-track axis.
- **Pushbroom scanner**: an array of detectors aligned across-track is used to achieve parallel scanning in the along-track axis. The satellite does not requiere moving parts.

The most common scanning method is the pushbroom scanning, depicted in Figure 1.3(a), as it provides high spectral resolution and avoids the use of moving parts in the satellite optical subsystem. Figure 1.3 shows some of the main parameters characterising the image acquisition. The field of view (FOV) is defined as the full angular coverage of the satellite, whereas the instantaneous field of view ($IFOV$) represents the angular coverage of a single detector element. The distance projected on the Earth's surface is known as ground-projected field of view ($GFOV$) in the case of the full angular coverage, and ground-projected instantaneous field of view ($GIFOV$) in the case of a single detector element. In the figure, f represents the focal distance of the optical system and w is the detector width. Another important parameter is the ground sampling distance, GSD, which represents the distance between two contiguous pixels. Typically, remote sensing satellites are designed for $GSD \cong GIFOV$.

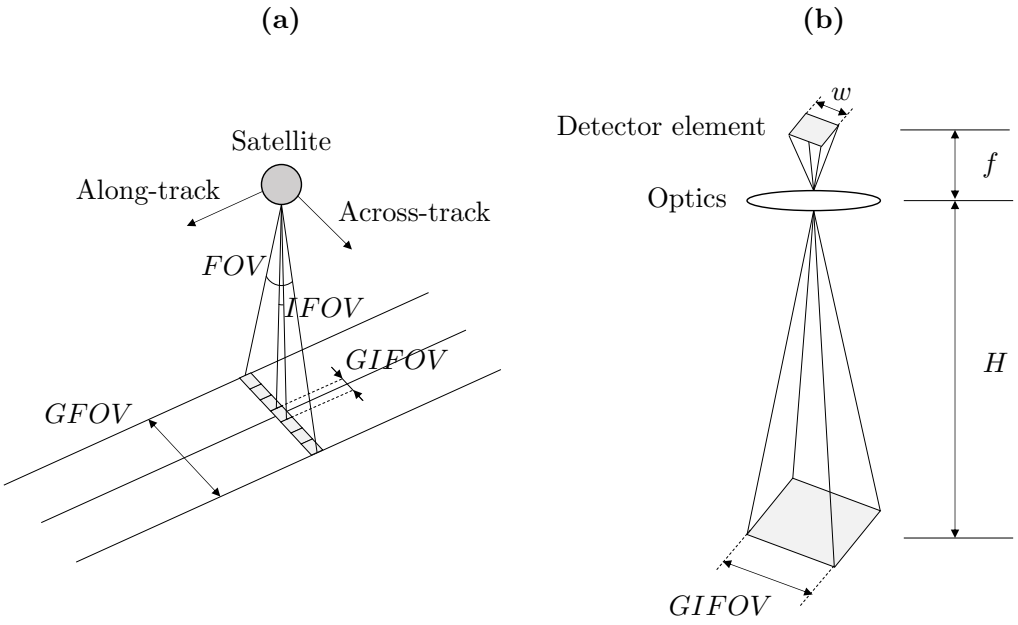

Figure 1.3: (a) Scheme of a pushbroom scanner with its main parameters and (b) geometric description of one detector element.

The $GFOV$, also known in the literature as swath width, can be calculated directly from the FOV parameter as

$$GFOV = 2H \tan\left(\frac{FOV}{2}\right), \tag{1.7}$$

being H the nadir distance between Earth and satellite.

Analogously to the $GFOV$ parameter, the $GIFOV$ can be calculated as

$$GIFOV = 2H \tan\left(\frac{IFOV}{2}\right), \tag{1.8}$$

which, keeping in mind that $\tan(IFOV/2) = w/(2f)$, can be simplified to

$$GIFOV = w\frac{H}{f}. \tag{1.9}$$

On the other hand, the GSD can be calculated from the inter-detector distance (d) and the focal distance of the optical system :

$$GSD = d\frac{H}{f}. \tag{1.10}$$

Therefore, if the inter-detector distance is equal to the detector width ($d \cong w$), the GSD is equal to the ground-projected instantaneous field of view. Another important parameter that defines the spatial quality of spectral images is the spatial resolution of the optical instrument, which should not be confused with the GSD. The spatial resolution is usually defined as the full-width half maximum ($FWHM$) of the optical system PSF. The information at the input of the optical detector corresponds to the top-of-atmosphere Earth's surface scene convoluted with the PSF, which means the output image is going to be more blurred or sharper depending on the $FWHM$

of the PSF. Remote sensing optical instruments are usually designed for $FWHM$ ranging from $1GSD$ to $1.6GSD$, and thus each pixel contains mainly information about its $GIFOV$ scene. The Fourier transform of the PSF is known as the modulation transfer function (MTF), and it specifies the spatial frequency response of the instrument. A critical parameter defined from the MTF is the MTF value at Nyquist frequency. All the information containing spatial frequencies above Nyquist frequency will translate into aliasing artifacts at the image, and thus a high MTF value at this frequency means that the spectral image will have those aliasing artifacts. Therefore, ideally, to reduce aliasing the MTF of the instrument should be designed to provide a low MTF value at Nyquist. However, as the MTF is the Fourier transform of the PSF, a narrower MTF response results in a wider PSF in the spatial domain and, therefore, a lower spatial resolution (wider $FWHM$). In this sense, simulations show that a normalized MTF value at Nyquist between 0.2 and 0.5 is a good trade-off between aliasing and resolution [8].

1.3.2 Spectral resolution

For a given (x,y) point, the spectral information for that pixel (x,y,λ) is the result of a convolution between the incoming spectral radiance and the instrument spectral response. The main spectral parameters of the sensor are: spectral resolution, spectral coverage, and spectral sampling. The spectral resolution is defined as the width of the spectral channels of the instrument, while the spectral sampling corresponds to the spectral distance between consecutive channels. On the other hand, the spectral coverage refers to the spectral range sampled by the instrument. Depending on these spectral parameters, the optical sensors can be classified in three types:

- **Panchromatic**: one single spectral channel with a large bandwidth (typically >100 nm).
- **Multispectral**: several spectral channels with a medium bandwidth (typically >20 nm).
- **Hyperspectral**: large amount of contiguous spectral channels (typically 100 or more) with bandwidths from 5 to 20 nm.

1.3.3 Product types

The output information produced by the sensor has to be preprocessed in order to generate a reliable spectral image. Thus, the objective of the preprocessing step is to produce high quality reflectance data in a given map projection from the raw data acquired by the sensor. In this sense, the scientific community has established a name convention for remote sensing products, classified depending on the type of preprocessing corrections applied to the data:

- **Level 0 (L0)**: raw data from the sensor (digital numbers).
- **Level 1B (L1B)**: radiometrically calibrated radiance data (L^s_λ).
- **Level 1C (L1C)**: radiometrically calibrated radiance data (L^s_λ) in a map projection. Depending on the mission, sometimes L1C products correspond to top-of-atmosphere reflectance in a map projection (*e.g.* Sentinel-2 European mission).
- **Level 2A (L2A)**: surface reflectance data ($\rho(\lambda)$) in a map projection.

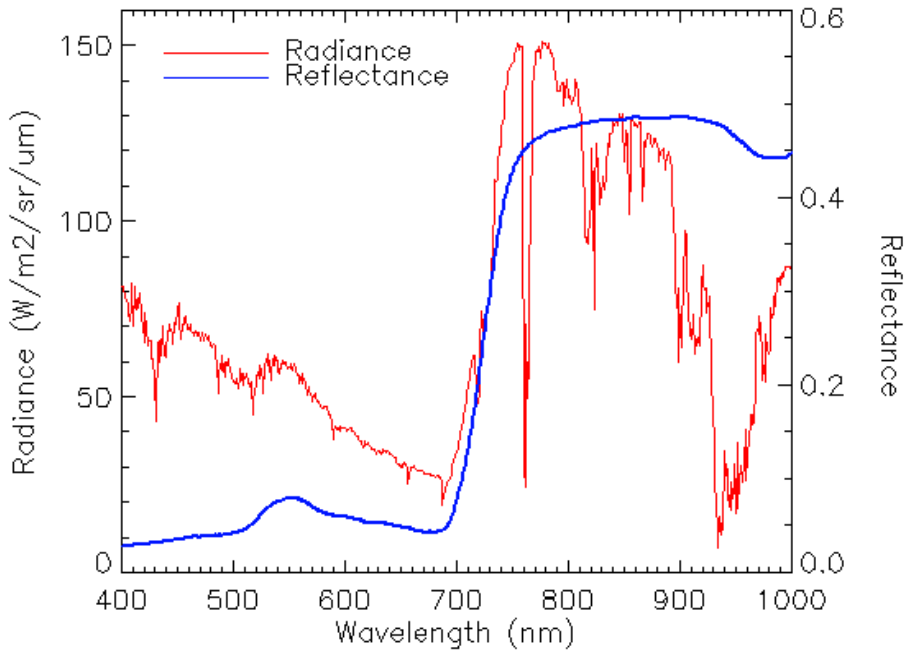

Figure 1.4: Surface reflectance (blue) calculated from the measured radiance at the sensor (red).

L1B products are obtained as a result of the radiometric correction of L0 data. The radiometric corrections allows to obtain calibrated top-of-atmosphere radiance data from the digital numbers stored by the sensor. After the radiometric corrections, geometric corrections are applied to L1B products, which correct spatial distortions and project L1B products to conventional map coordinates, in order to generate L1C images. Then, atmospheric corrections convert L1C radiance data to surface reflectance data, which contains the spectral signatures of the Earth's surface components. Figure 1.4 shows an example of the measured spectral radiance L^s_λ information for one pixel of a L1B product in red color, and the resulting reflectance $\rho(\lambda)$ spectrum after applying the atmospheric corrections in blue.

Chapter 2

Methodology

2.1 Objectives

The main objective of this master thesis is to implement a method to estimate the modulation transfer function (MTF) of optical imagers using images acquired during regular mission operations. Two different algorithms are selected by reviewing current state of the art MTF assessment techniques, and then implemented in Python using Open Source libraries. As explained in the previous chapter, the MTF represents the spatial frequency response of the optical sensor, and therefore it conditions the spatial resolution and quality of the resulting images. The algorithms are developed in Python, a widely used programming language among scientist and professional developers. The performance and the accuracy of the estimation algorithms are tested using both simulations and real images from remote sensing satellites in order to validate the MTF assessments.

2.2 Thesis structure

This master thesis has been structured along three phases. The first phase consists on the bibliographic review of how remote sensing satellites work, with special attention to passive optical instruments. The results of this phase are summarized in Chapter 1. The second phase consists on a bibliographic review of MTF estimation methods and their theoretical models, which corresponds to Chapter 3. The third and last thesis phase is to develop and validate the MTF estimation algorithms, which corresponds to Chapter 4.

In order to complete all three phases, the project has been divided in the following tasks:

1. Bibliographic review of optical remote sensing instruments for earth observation.
2. Bibliographic review of theoretical MTF estimation methods for remote sensing satellites.
3. Design and development of MTF estimation algorithms in Python.
4. Develop an algorithm to simulate ideal images to test the estimation algorithm.
5. Test the MTF algorithms with ideal simulations.

6. Test the MTF algorithms with calibrated real images.
7. Estimate the MTF of real remote sensing missions with the developed algorithms.
8. Write the Master thesis with the obtained results.

2.3 Task schedule

The tasks described in the previous section have been arranged following the next schedule:

Task	October 19	November 19	December 19	January 20	February 20
1	×				
2	×	×			
3		×	×		
4			×		
5			×		
6				×	
7				×	
8					×

Table 2.1: Schedule of the Master thesis tasks.

Chapter 3

Modulation Transfer Function

3.1 Definition

As introduced in Chapter 1, the modulation transfer function (MTF) plays a very important role in the spatial quality of the image. Physically, the MTF of an optical instrument relates the output amplitude of a given spatial frequency component with its input amplitude. The spatial domain equivalent of the MTF is the point spread function (PSF), which is given as a function of the imaging optics, detector, electronics, and satellite motion spatial responses.

Figure 3.1 depicts a block diagram of the optical instrument of a remote sensing satellite. The function of the spectral filter, or the dispersion element, is to split the incoming image into the different wavelengths λ_i of the detectors, where $i = 1, 2, ..., N$, being N the total number of detectors. In the figure, $i(x, y, \lambda)$ stands for the input radiance at the imaging optics subsystem, while $i'(x, y, \lambda_i)$ represents the output radiance of the imaging optics for each spectral band λ_i, and DN_{λ_i} represents the output digital numbers of each spectral band.

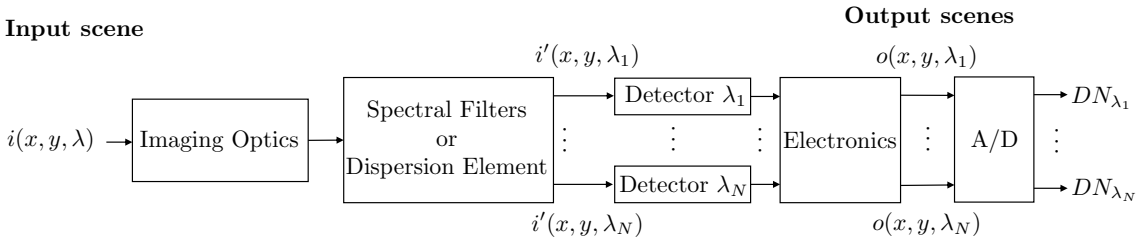

Figure 3.1: Block diagram of the optical instrument.

It results more intuitive to start with the explanation and mathematical analysis of the PSF, and then translate the results from spatial to spatial frequency domain to explain the MTF and its different contributions.

3.1.1 Point Spread Function

The total point spread function of the optical instrument, PSF_t, can be calculated as the convolution of the PSF of each one of their parts [1, 9, 10], that is,

$$PSF_t(x, y) = PSF_o * PSF_m * PSF_d * PSF_e, \tag{3.1}$$

where PSF_o corresponds to the optical imaging subsystem, PSF_m models the effect of the satellite motion on the image, PSF_d corresponds to the detector, and PSF_e corresponds to the electronics. At this step, it is worth noting that, depending on the instrument subsystem, its PSF can be given as a function of the focal plane spatial coordinates (x',y') or the earth's surface coordinates (x,y). Thus, focal plane coordinates (x',y') can be easily converted to earth's surface coordinates (x,y), and viceversa, using the following equivalences:

$$\frac{x'}{f} = \frac{x}{H}, \tag{3.2}$$

and

$$\frac{y'}{f} = \frac{y}{H}. \tag{3.3}$$

Analogously, the convolution can be performed in the spatial frequency domain. The Fourier transform of the PSF is known as the optical transfer function (OTF). Therefore, the total optical transfer function, OTF_t, is given by

$$OTF_t(f_x, f_y) = OTF_o \cdot OTF_m \cdot OTF_d \cdot OTF_e. \tag{3.4}$$

with (f_x,f_y) being the spatial frequencies in the across-track and along-track axis, respectively.

First, the optical imaging introduces blur at the input scene as a consequence of its limited spatial resolution. In addition, the satellite is moving during the integration time of each pixel, which decreases the resolution along the motion direction of the satellite. Then, each detector introduces blur because of their limited spatial size. Finally, the electronics further degrade the image quality as a consequence of the low-pass filtering. Therefore, the image at the input of the analog/digital (A/D) converter for the λ_i band, $o(x, y, \lambda_i)$, can be calculated as $i(x, y, \lambda_i) * PSF_t(x, y, \lambda_i)$:

$$o(x, y, \lambda_i) = \int_{-\infty}^{+\infty} \int_{-\infty}^{+\infty} i(\mu, \tau, \lambda_i) PSF_t(x - \mu, y - \tau, \lambda_i) d\mu d\tau. \tag{3.5}$$

Analogously, in the spatial frequency domain, $o(f_x, f_y, \lambda_i)$ is given by

$$o(f_x, f_y, \lambda_i) = i(f_x, f_y, \lambda_i) \cdot OTF_t(f_x, f_y). \tag{3.6}$$

3.1.1.1 Imaging optics – PSF_o

The resolution of the imaging optics of the satellite is limited by diffraction, as an ideal point source $i(x, y, \lambda_i) = \delta(x, y)$ at the input will not generate an ideal point source at the focal plane. The energy of the point source will be spread over a limited area at the focal plane. The size of this area depends on the resolution of the imaging optics. If we consider an ideal circular pupil function, the

resulting optical point spread function, PSF_o, will be an Airy pattern, with a main circular lobe and surrounding rings with decreasing intensity:

$$PSF_o(\theta, \lambda_i) = \left(\frac{2J_1(kD\sin(\theta)/2)}{kD\sin(\theta)/2} \right)^2, \tag{3.7}$$

being D the aperture diameter of the optics, $k = 2\pi/\lambda_i$ the wavenumber, θ the angle referred to the nadir direction, and J_1 the first kind and first order Bessel function. Keeping in mind that $\sin(\theta) = r/\sqrt{r^2 + f^2} \cong r/f$, where $r = \sqrt{(x')^2 + (y')^2}$ is the radial distance over the focal plane, the above expression can be simplified to

$$PSF_o(r, \lambda_i) = \left(\frac{2J_1\left(\frac{\pi D}{\lambda_i f} r\right)}{\frac{\pi D}{\lambda_i f} r} \right)^2. \tag{3.8}$$

Depending on the imaging optics subsystem, it may not be possible to describe the PSF_o analytically. In these cases, the PSF_o has to be experimentally measured and characterized. A common function used to describe PSF_o in these cases is the 2D gaussian function:

$$PSF_o(x, y, \lambda_i) = \frac{1}{2\pi\sigma_{x,\lambda_i}\sigma_{y,\lambda_i}} e^{-\frac{x^2}{2\sigma^2_{x,\lambda_i}}} \cdot e^{-\frac{y^2}{2\sigma^2_{y,\lambda_i}}}. \tag{3.9}$$

The parameters σ_{x,λ_i} and σ_{y,λ_i} determine the optical resolution in the across-track and along-track directions, respectively. For an ideal gaussian function, the resolution is given by $FWHM_i = 2\sigma_i\sqrt{\ln(4)}$. Figure 3.2 shows an example of an Airy pattern as a function of the normalized radial coordinate (r/λ) for a lens with $f/D = 1$, compared to its gaussian approximation function. The gaussian approximation for an Airy function is optimum for $\sigma = 0.42\lambda f/D$. In the case of the figure, the resolution of the optical point spread function is $FWHM = 1.03\lambda$.

3.1.1.2 Satellite motion – PSF_m

The effect of the satellite motion can be modeled as a rectangular pulse aligned in the scanning direction. Therefore, for a pushbroom scanner, the scanning is produced in the along-track direction (y-axis), which yields to the following PSF_m response:

$$PSF_m(x, y) = \delta(x) \cdot \text{rect}\left(\frac{y}{s_d}\right), \tag{3.10}$$

where s_d represents the distance that the satellite covers during the integration time of one pixel, that is,

$$s_d = \text{satellite velocity} \times \text{integration time}. \tag{3.11}$$

3.1.1.3 Detector – PSF_d

The blur caused by the detector is due to its non-zero size, which means that the detector is measuring information of the point (x, y) and its surroundings. Thus, if we consider a square detector with dimensions $w \times w$, its spatial response can be modeled by

$$PSF_d(x', y') = \text{rect}\left(\frac{x'}{w}\right) \cdot \text{rect}\left(\frac{y'}{w}\right). \tag{3.12}$$

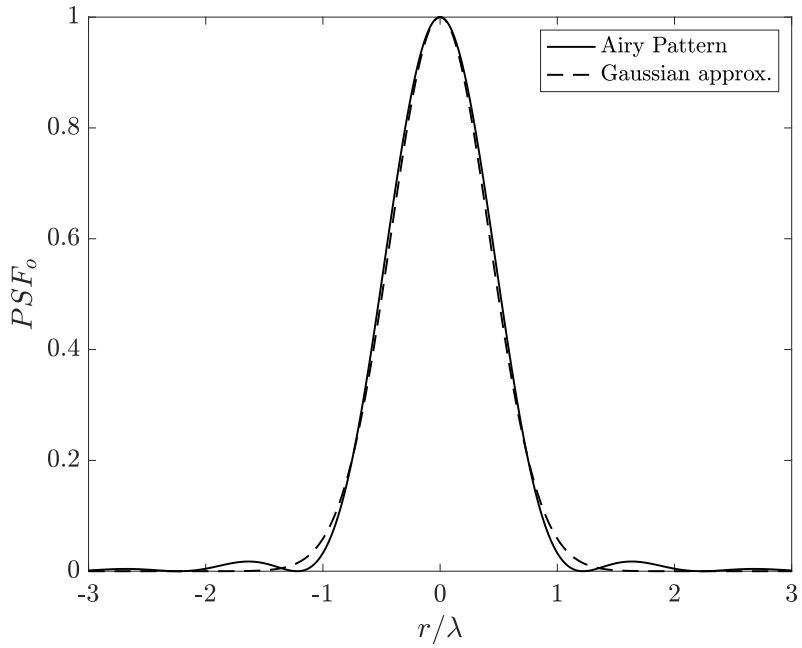

Figure 3.2: Optical point spread function along the normalized radial coordinate: airy pattern (solid line) and gaussian approximation (dashed line).

3.1.1.4 Electronics – PSF_e

The last element of the block diagram of Figure 3.1 that degrades the image quality is the electronic subsystem. The signal at the output of the detector has to be electronically filtered to reduce noise an avoid aliasing due to frequency components above the Nyquist frequency of the A/D. As the low pass filter is performed in the time domain, time-dependence has to be converted to spatial dependence. For a pushbroom scanner, this is achieved by

$$y = \text{satellite velocity} \times \text{time}. \tag{3.13}$$

As the motion direction is aligned with the along-track axis, the low pass filtering affects the frequency components of the along-track axis, that is,

$$OTF_e(f_x, f_y) = H(f_y), \tag{3.14}$$

where $H(f_y)$ represents the spatial low-pass frequency response of the electronics. This response can be implemented as any kind of low-pass filter, e.g. a 3^{rd} order Butterworth filter. The low-pass filter is not always implemented, depending on the mission and scanning type.

3.1.1.5 Total response – PSF_t

As stated before, the total response is calculated as the convolution of each one of the point spread function of its components. In this sense, Figure 3.3 depicts a simulation of an instrument PSF and the contributions of the different subsystems, as a function of the normalized spatial coordinates in the focal plane. Figure 3.3(a) corresponds to the optical PSF_o, while 3.3(b) corresponds to

the motion contribution PSF_m, and 3.3(c) represents the detector response PSF_d. Finally, Figure 3.3(d) represents the total PSF_t of the instrument. In the simulation, a 2D gaussian response with a resolution of $FWHM_{x',y'} = 0.8w$ and a motion distance of $s_d = 0.7w$ have been considered for the imaging subsystem and the motion contribution, respectively. For simplicity, no electronic filtering has been used. As it can be observed from the figure, the motion contribution only degrades the PSF_t quality along the motion direction, and the most significan contribution to the PSF_t is the detector PSF_d.

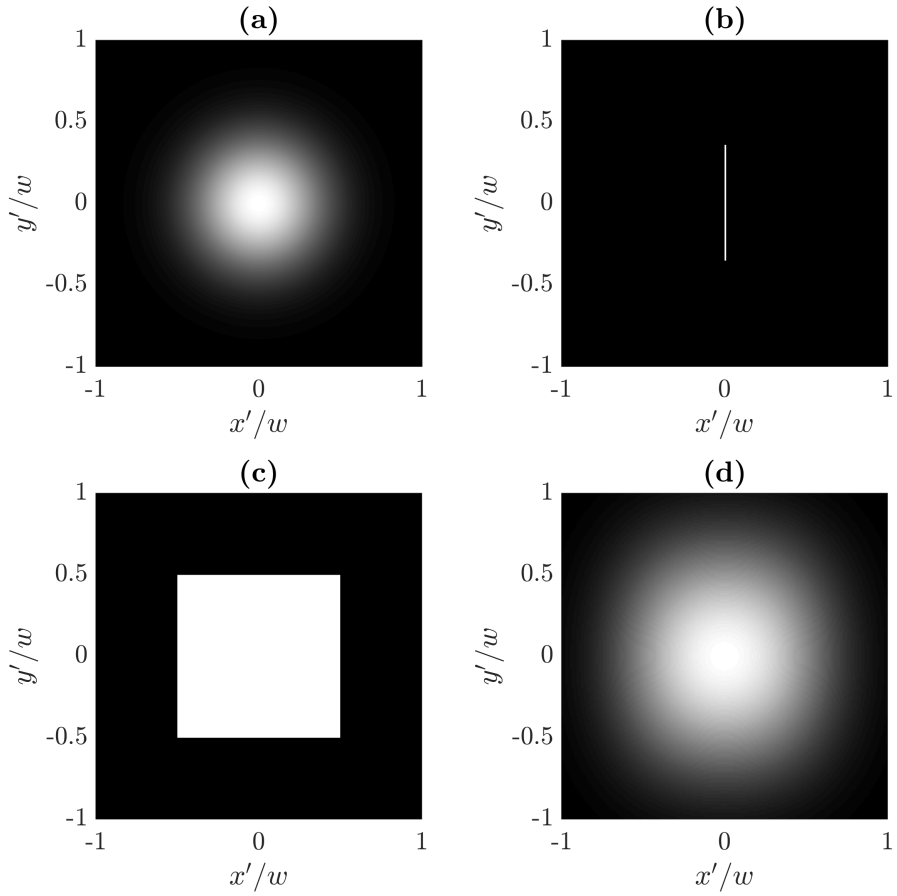

Figure 3.3: PSF as a function of the focal plane spatial coordinates (x',y') normalized by the detector width w: (a) Optical imaging PSF_o, (b) motion contribution PSF_m, (c) detector PSF_d, and (d) total response PSF_t.

Figures 3.4(a) and 3.4(b) depict across-track and along-track total PSF_t, respectively, and the corresponding contributions of the different elements to the final instrument response shown in Figure 3.3. Blue lines represent the imaging optics PSF_o, while red lines correspond to the detector PSF_d and gray lines to the motion degradation PSF_m. Black lines are for the total PSF_t of the instrument. Figure 3.4 reveals that, as mentioned before, the main source of spatial resolution degradation is the non-zero size of the detector, PSF_d. Considering an inter-detector separation of $d = w$ and using equations 1.10, 3.2 and 3.3, total spatial resolutions of $FWHM_{x'} = 1.04w$ and $FWHM_{y'} = 1.14w$ along the focal plane correspond to spatial resolutions along the earth's

surface of

$$FWHM_x = \frac{H}{f} FWHM_{x'} = 1.04 \cdot GSD \tag{3.15}$$

and

$$FWHM_y = \frac{H}{f} FWHM_{y'} = 1.14 \cdot GSD, \tag{3.16}$$

proving that, as expected, in pushbroom scanning instruments across-track resolutions are usually higher than along-track resolutions.

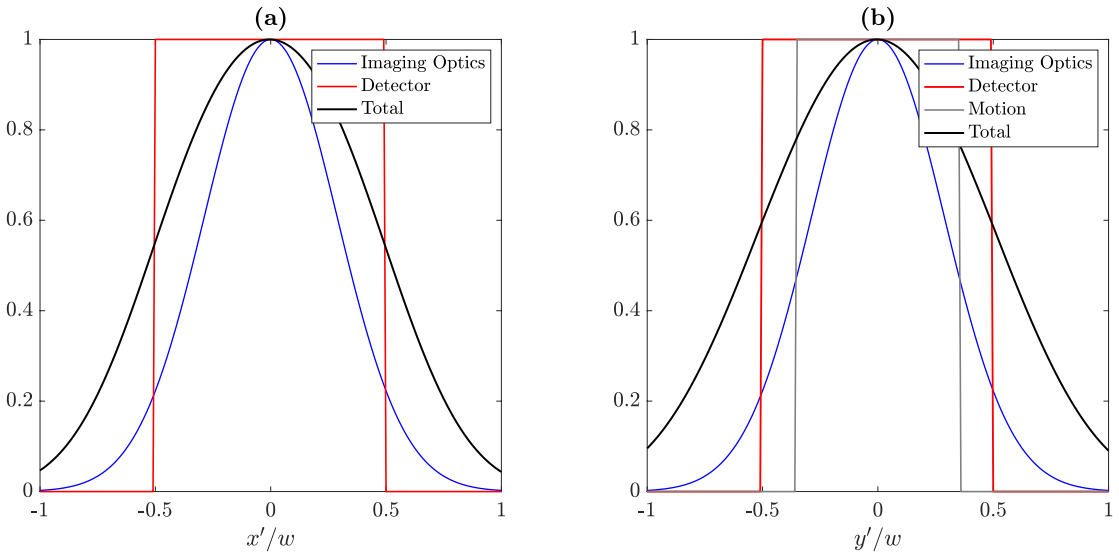

Figure 3.4: PSF_t and their different contributions as a function of the focal plane coordinates normalized by the detector width w: (a) Across-track ($y' = 0$) and (b) along-track ($x' = 0$).

3.1.2 Modulation Transfer Function

Mathematically, the modulation transfer function (MTF) is defined as the absolute value of the OTF, and it represents the instrument response as a function of the spatial frequency [1, 9, 10]. In this sense, dealing with the MTF assessment of an instrument is equivalent to dealing with its PSF evaluation, and viceversa, as the only difference is that the first function is given along spatial coordinates and the later along spatial frequency coordinates. Due to the limited spatial resolution of the instrument components, the instrument acts as a low-pass filter in the spatial frequency domain. This means that, depending on the PSF_t resolution, the sharper details of the image, which correspond to higher spatial frequencies, will be attenuated or lost in the imaging and detection process. Thus, the higher the spatial resolution is, the sharper the details the optical instrument can detect. The total MTF of the instrument, MTF_t, can be calculated as the product of the MTF responses of each element of the system, that is,

$$MTF_t = |OTF_t| = |OTF_o| \cdot |OTF_m| \cdot |OTF_d| \cdot |OTF_e|. \tag{3.17}$$

3.1.2.1 Imaging optics – MTF_o

If we consider an ideal 2D gaussian function as the optical PSF_o (Equation 3.9), the contribution of the imaging optics to the MTF response is simply given by

$$MTF_o = |\mathcal{F}_{xy}\{PSF_o\}| = e^{-2\pi^2\sigma_x^2 f_x^2} \cdot e^{-2\pi^2\sigma_y^2 f_y^2}, \tag{3.18}$$

where $\mathcal{F}_{xy}\{\cdot\}$ represents the Fourier transform along the (x,y) axis.

3.1.2.2 Satellite motion – MTF_m

Analogously to the imaging optics, the contribution of the satellite motion to the final MTF_t of the instrument can be calculated as the Fourier transform of its point spread function, PSF_m, that is,

$$MTF_m = |\mathcal{F}_{xy}\{PSF_m\}| = s_d|\text{sinc}(s_d f_y)|, \tag{3.19}$$

with $\text{sinc}(x) = \frac{\sin(\pi x)}{\pi x}$.

3.1.2.3 Detector – MTF_d

The modulation transfer function of a square detector with an area of $w \times w$, MTF_d, is given by

$$MTF_d = |\mathcal{F}_{xy}\{PSF_d\}| = w^2|\text{sinc}(wf_x) \cdot \text{sinc}(wf_y)|. \tag{3.20}$$

3.1.2.4 Electronics – MTF_e

As the low-pass filter is usually designed in the frequency domain, the contribution of the electronic subsystem to MTF_t is simply calculated as

$$MTF_e = |OTF_e| = |H(f_y)|. \tag{3.21}$$

3.1.2.5 Total response – MTF_t

As mentioned earlier, the total modulation transfer function of the instrument is calculated as the product of its different contributions. Figure 3.5 shows a simulation of the MTF responses as a function of the spatial frequency coordinates (f_x,f_y), normalized by the spatial sampling frequency (f_s). On the focal plane, the sampling distance corresponds to the inter-detector separation, d, while on the earth's surface this sampling distance is converted to the GSD. Therefore, the sampling frequency on the focal plane is given by the inverse of the sampling distance, that is, $f_s = 1/d$. Keeping in mind that, in this case, $d = w$, the sampling frequency is finally given by $f_s = 1/w$. In the figure, all the results have been calculated from the PSF simulations depicted in Figure 3.3. Thus, Figure 3.5(a) corresponds to the imaging optics MTF_o, whereas 3.5(b) corresponds to the satellite motion degradation MTF_m, 3.5(c) represents the detector MTF_d, and 3.5(d) represents the total response MTF_t. As expected from the theoretical model, the satellite motion only affects the along-track spatial frequencies, and remains constant along the across-track spatial frequencies.

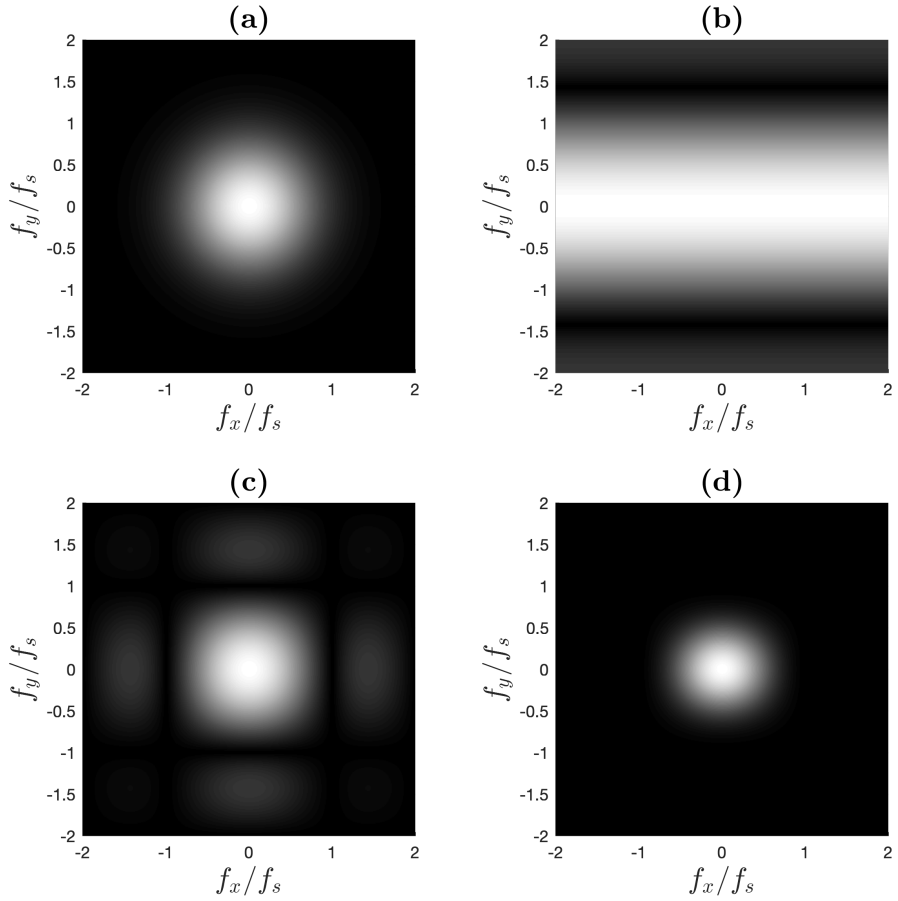

Figure 3.5: MTF **as a function of the spatial frequency coordinates (**f_x**,**f_y**): (a) Optical imaging** MTF_o**, (b) motion contribution** MTF_m**, (c) detector** MTF_d**, and (d) total response** MTF_t**.**

Figures 3.6(a) and 3.6(b) represent the across-track and along-track MTF responses, respectively. As in Figure 3.4, blue lines represent the optical imaging subsystem contribution, red lines represent the detector response, gray lines correspond to the satellite motion effect, and black lines represent the final MTF_t. As can be seen in the figure, the most significant contribution is that from the detector, MTF_d, which agrees with the fact that the detector is also the main source of spatial resolution degradation. As mentioned in Chapter 1, one important parameter that scientists use to characterize the MTF is the MTF value at Nyquist frequency, MTF^{nyq}. All the information with spatial frequencies above Nyquist frequency will produce aliasing artifacts at the image. Therefore, to reduce the amount of aliasing artifacts, a low MTF^{nyq} is required. However, as analyzed in this section, the MTF is calculated as the Fourier transform of the PSF, which means that a narrower MTF will produce a wider PSF and, thus, decrease the resolution of the instrument. This is why an MTF^{nyq} value between 0.2 and 0.5 is considered a good trade-off between resolution and aliasing.

The Nyquist frequency is calculated as half the sampling frequency, which in the case of the Earth's surface (x,y) yields to

$$f_{nyq} = \frac{f_s}{2} = \frac{1}{2 \cdot GSD}, \tag{3.22}$$

while in the case of the focal plane (x',y') it yields to

$$f_{nyq} = \frac{1}{2 \cdot d}. \tag{3.23}$$

Therefore, in this case, as $d = w$, the Nyquist frequency is given by $f_s = 0.5/w$. The MTF values at Nyquist frequency for the across-track and along-track total responses are $MTF_x^{nyq} = 0.42$ and $MTF_y^{nyq} = 0.34$, respectively. Thus, as expected from the results depicted in Figure 3.4, the across-track value at Nyquist frequency is higher than the along-track value at the same frequency, meaning that the across-track spatial resolution is higher than that of the along-track.

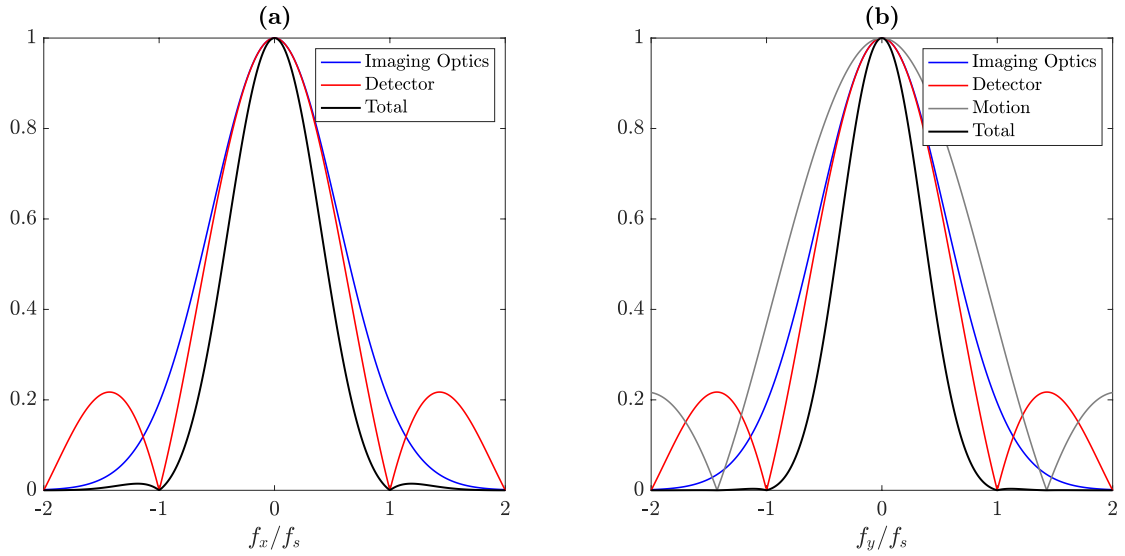

Figure 3.6: MTF_t and their different contributions as a function of the spatial frequency coordinates (f_x,f_y): (a) Across-track ($f_y = 0$) and (b) along-track ($f_x = 0$).

3.2 Influence on the image quality

The MTF of the instrument relates the input amplitude $i(f_{x_i}, f_{y_j})$ of a given spatial frequency (f_{x_i},f_{y_j}) with its amplitude at the output of the instrument $o(f_{x_i}, f_{y_j})$, that is,

$$MTF(f_{x_i}, f_{y_j}) = \frac{|o(f_{x_i}, f_{y_j})|}{|i(f_{x_i}, f_{y_j})|}. \tag{3.24}$$

Therefore, as the MTF response decreases with the spatial frequency, the output amplitude of higher spatial frequency components is lower than that of lower spatial frequency components. In order to showcase this phenomenon, Figure 3.7 shows a simulation of an ideal MTF and its effect on the output signal of the instrument. Figure 3.7(a) depicts the simulated MTF, while Figure 3.7(b) shows the input signal (blue color) and the output signal (red color). As can be observed from the figure, the input signal is an ideal sinusoidal function along the spatial coordinate, that is,

$$i(x) = \sin(2\pi f_0 x), \tag{3.25}$$

being $f_0 = 1/T_x$ the spatial frequency of the signal and T_x its spatial period. The frequency response of an ideal sinusoidal function is given by

$$i(f_x) = \mathcal{F}_x\{i(x)\} = \frac{\delta(f_x - f_0) - \delta(f_x + f_0)}{2j}. \tag{3.26}$$

where $j = \sqrt{-1}$. Thus, in this case, the output signal can be calculated using Equation 3.24 as

$$o(f_x) = MTF(f_x) \cdot i(f_x) = \frac{MTF(f_x)\delta(f_x - f_0) + MTF(f_x)\delta(f_x + f_0)}{2j}. \tag{3.27}$$

Using the translation property of the delta function, which states that $f(x)\delta(x-x_0) = f(x_0)\delta(x-x_0)$, the above equation can be simplified to

$$o(f_x) = MTF(f_0)\frac{\delta(f_x - f_0) + \delta(f_x + f_0)}{2j} = MTF(f_0)i(f_x). \tag{3.28}$$

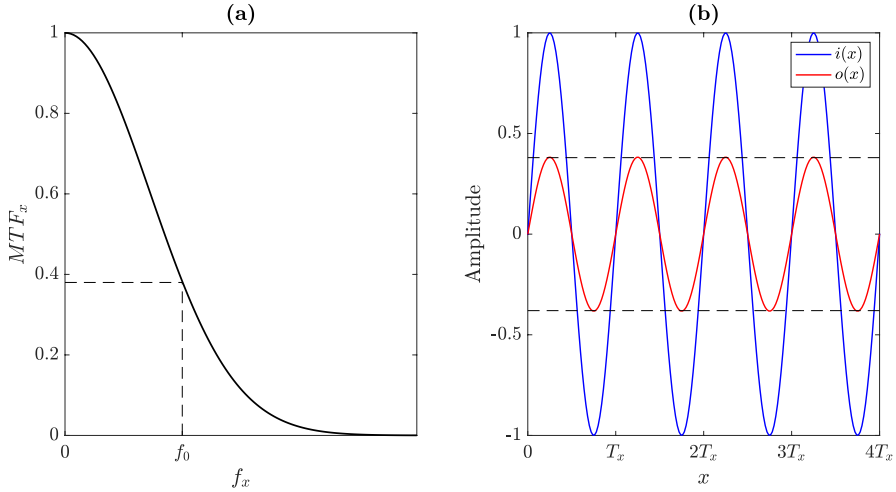

Figure 3.7: (a) MTF and (b) input (blue color) and output (red color) signals. The input signal is an ideal sinusoidal function of frequency f_0.

As $MTF(f_0)$ is a constant value, the output signal in the spatial domain can be finally calculated as

$$o(x) = \mathcal{F}_x^{-1}\{o(f_x)\} = MTF(f_0)\mathcal{F}_x^{-1}\{i(f_x)\} = MTF(f_0)i(x), \tag{3.29}$$

where $\mathcal{F}_x^{-1}\{\cdot\}$ denotes the inverse Fourier transform. Thus, the signal of spatial frequency f_0 is attenuated by the MTF value at that specific frequency. For instance, Figure 3.7(a) shows that, for the frequency f_0, the modulation transfer function is $MTF(f_0) = 0.38$, and 3.7(b) depicts that the output amplitude of an ideal sinusoidal function of frequency f_0 is 0.38, which agrees with the theoretical equations. Therefore, lower spatial frequencies than f_0 will be less affected, while higher spatial frequencies will be more strongly attenuated by the MTF of the instrument. In order to demonstrate this fact, Figure 3.8 depicts a simulation of a sinusoidal signal with increasing frequency along the spatial distance. As can be observed from Figure 3.8(b), the output amplitude decreases as the frequency increases.

Figure 3.9 depicts a simulation of a high resolution image filtered with two different PSFs, being both of them ideal 2D gaussian functions (Equation 3.9). Figure 3.9(a) corresponds to an

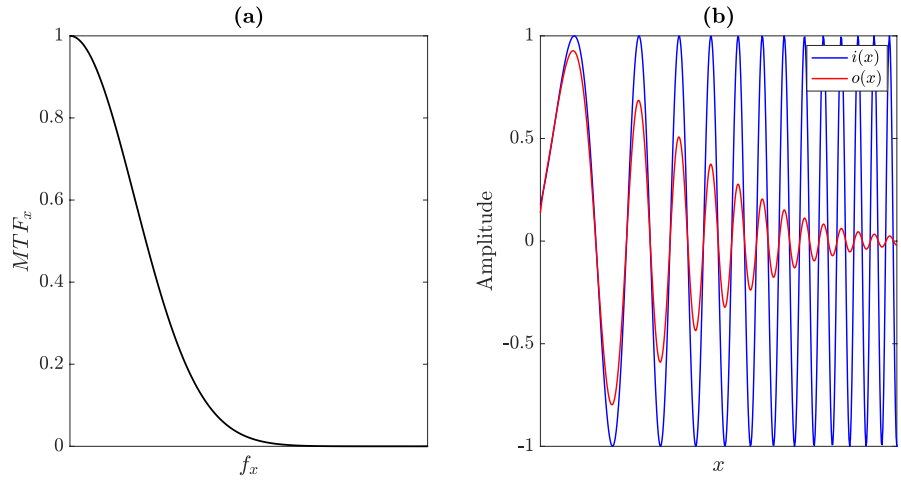

Figure 3.8: Same as Figure 3.7, but with increasing frequency along the spatial dimension.

image filtered with a PSF with spatial resolution $FWHM = 1GSD$, while Figure 3.9(b) is obtained using a PSF with $FWHM = 1.6GSD$. The MTF value at Nyquist frequency in Figures 3.9(a) and 3.9(b) are $MTF^{nyq} = 0.41$ and $MTF^{nyq} = 0.10$, respectively. As can be seen in the figure, the image with a wider MTF, and therefore higher spatial resolution, looks sharper than the image with a narrower MTF. The simulation process used to obtain these images will be described in Chapter 4.

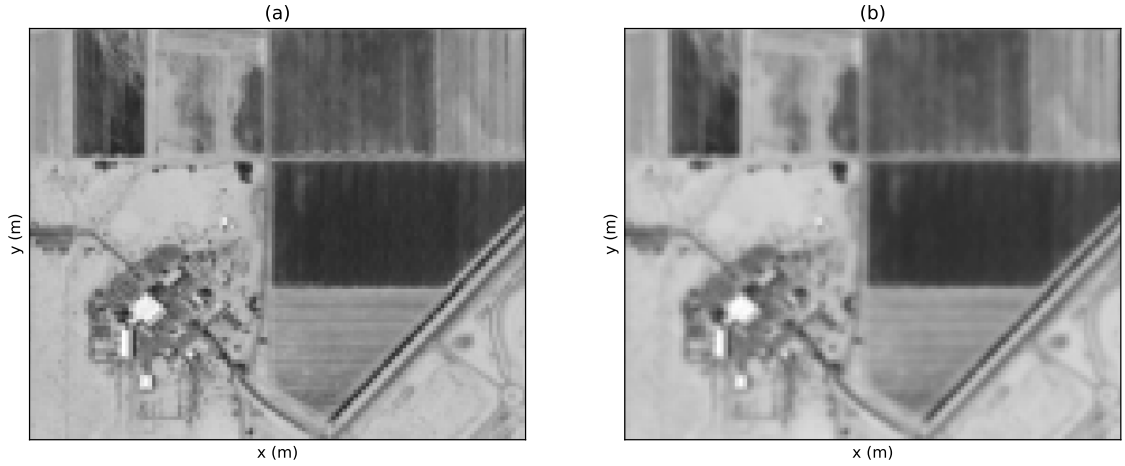

Figure 3.9: High resolution image filtered with: (a) PSF with resolution $FWHM = 1GSD$ and (b) PSF with resolution $FWHM = 1.6GSD$.

3.3 Image-based estimation methods

In the past decades, scientists and engineers have developed different techniques that allow to estimate the MTF response of an instrument from experimental measurements. These techniques can be classified intro two big groups: ground-based techniques and in-flight methods. Ground-based techniques measure the MTF and PSF responses in the laboratory under controlled conditions,

following standardized procedures such as the ISO12233 [11]. On the other hand, in-flight methods use in-orbit satellite images to estimate the MTF response of the instrument from specific ground targets [10, 12, 13, 14, 15, 16, 17, 18]. In this work, we are going to focus on these kind of techniques. The main methods used for in-flight MTF estimation are:

- Slanted edge methods.
- Pulse target methods.
- Double-pulse target methods.

3.3.1 Slanted edge

Slanted edges methods employ ground targets that can be modeled as perfect sharp contrast edges [10, 13, 14]. From these targets, an oversampled edge spread function (ESF) is estimated, then the line spread function (LSF) is calculated, and, finally, the MTF function is evaluated. The ESF represents the 1D output signal of the instrument when the input is an ideal step function, $u(z)$, defined as

$$u(z) = \begin{cases} 0 & ; z < 0 \\ 1 & ; z \geq 0 \end{cases} \tag{3.30}$$

Therefore, the ESF is given as a function of the spatial direction aligned perpendicularly to the contrast edge, z. Analogously, the LSF represents the 1D PSF along the same spatial direction than the ESF. Thus, the ESF can be calculated as the convolution of the step function and the LSF along the z-axis:

$$ESF(z) = u(z) * LSF(z). \tag{3.31}$$

Figure 3.10 represents a scheme of an ideal 2D image with a sharp contrast edge slanted θ degrees respect to the x-axis. The fact that the edge is not perfectly aligned to the vertical y-axis allows to combine different x-axis cuts of the 2D image to form an oversampled ESF, which provides sub-pixel accuracy. Therefore, for each row y_i of the image, the horizontal edge location of the x-axis cut, $x_0(y_i)$, has to be estimated. Once $x_0(y_i)$ is obtained, the x-axis ESF is centered and then projected onto the z-axis, obtaining the edge spread function of that row, $ESF_i(z)$. The equivalence between x-axis coordinates and z-axis coordinates is given by

$$z = (x - x_0(y_i)) \cdot \cos(\theta). \tag{3.32}$$

This $ESF_i(z)$ centering and projection process is repeated for each one of the image rows, and the final oversampled ESF is calculated as

$$ESF(z) = \sum_{i=1}^{N} ESF_i(z), \tag{3.33}$$

where N is the total number of rows. As the z-axis evaluation points are different for each row (which provides the sub-pixel resolution), the combined ESF is unevenly sampled. This means that the final ESF has to be interpolated from the combined ESF_i samples, usually using a resolution between 0.1 and 0.2 pixels.

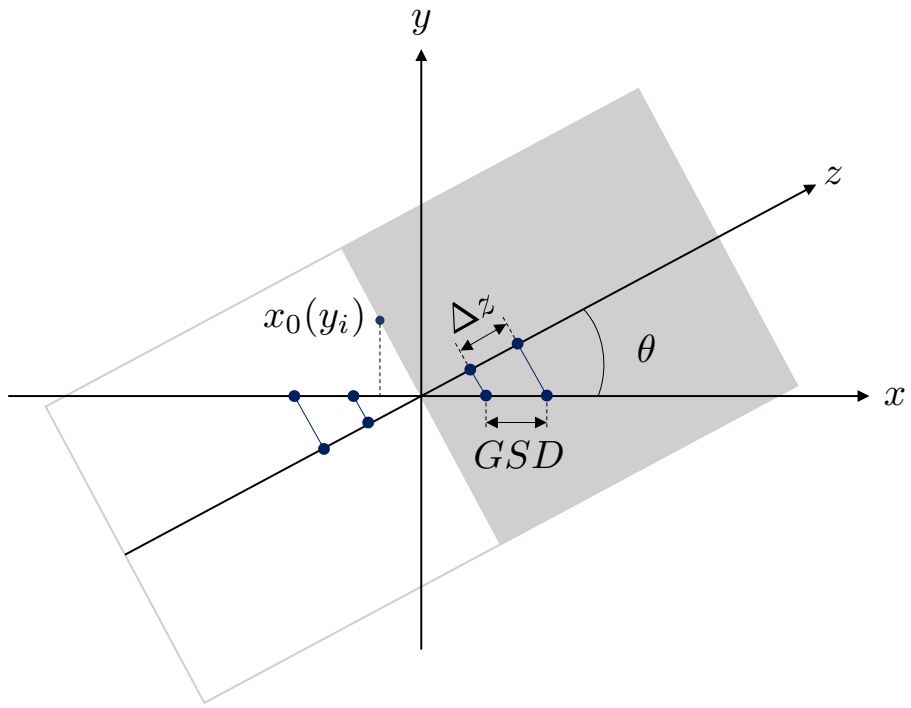

Figure 3.10: Slanted edge scheme used to estimate an oversampled ESF.

At this step, it is worth noting that the sampling distance of the profile along the z-axis, Δz, is no longer the GSD, but it is given by

$$\Delta z = GSD \cdot \cos(\theta), \tag{3.34}$$

and therefore the spatial sampling frequency for the z-axis is $f_s' = 1/\Delta z = f_s/\cos(\theta)$. It is important to use this sampling frequency when calculating the MTF, in order to avoid estimation errors.

Once the ESF is estimated, its derivative is numerically calculated. Theoretically, the derivative of the ESF is given by

$$\frac{dESF(z)}{dz} = \frac{d}{dz}\left(u(z) * LSF(z)\right). \tag{3.35}$$

Keeping in mind that $\frac{d}{dx}\left(f(x) * g(x)\right) = \left(\frac{df(x)}{dx} * g(x)\right) = \left(f(x) * \frac{dg(x)}{dx}\right)$, the above expression can be simplified to

$$\frac{dESF(z)}{dz} = \frac{du(z)}{dz} * LSF(z), \tag{3.36}$$

which, given that the derivative of an ideal step function is an ideal delta function, can be finally expressed as

$$\frac{dESF(z)}{dz} = \delta(z) * LSF(z) = LSF(z). \tag{3.37}$$

Therefore, the derivative of the ESF profile directly provides the LSF, which can be used to estimate the spatial resolution of the instrument along the z-axis. Finally, the MTF as a function

of the z-axis spatial frequency can be calculated as the absolute value of theFourier transform of the LSF:

$$MTF(f_z) = |\mathcal{F}_z\{LSF(z)\}|. \tag{3.38}$$

Figure 3.11 depicts an example of the MTF estimation process using the slanted edge technique. Figure 3.11(a) shows the 2D input image of an ideal slanted edge, whereas Figure 3.11(b) depicts the oversampled ESF along the z-axis. Then, this ESF is numerically differentiated in order to obtain the LSF of Figure 3.11(c) and, finally, the MTF of Figure 3.11(d) is computed as the Fourier transform of the LSF. Therefore, in order to estimate the MTF in the across-track direction (x-axis), ground targets with approximately ideal contrast edges in that direction have to be used. Simulations show that optimal performance is achieved for edge inclinations between 5º and 20º. Likewise, along-track MTF estimations (y-axis) have to be performed using slightly slanted vertical ground targets with sharp contrast edges. However, it is important to keep in mind that the MTF estimation is not exactly calculated in the across-track or along-track directions, but in the z-axis direction of the slanted edge. A good ground target that approximates an ideal contrast edge is the transition between vegetation and land of crop fields.

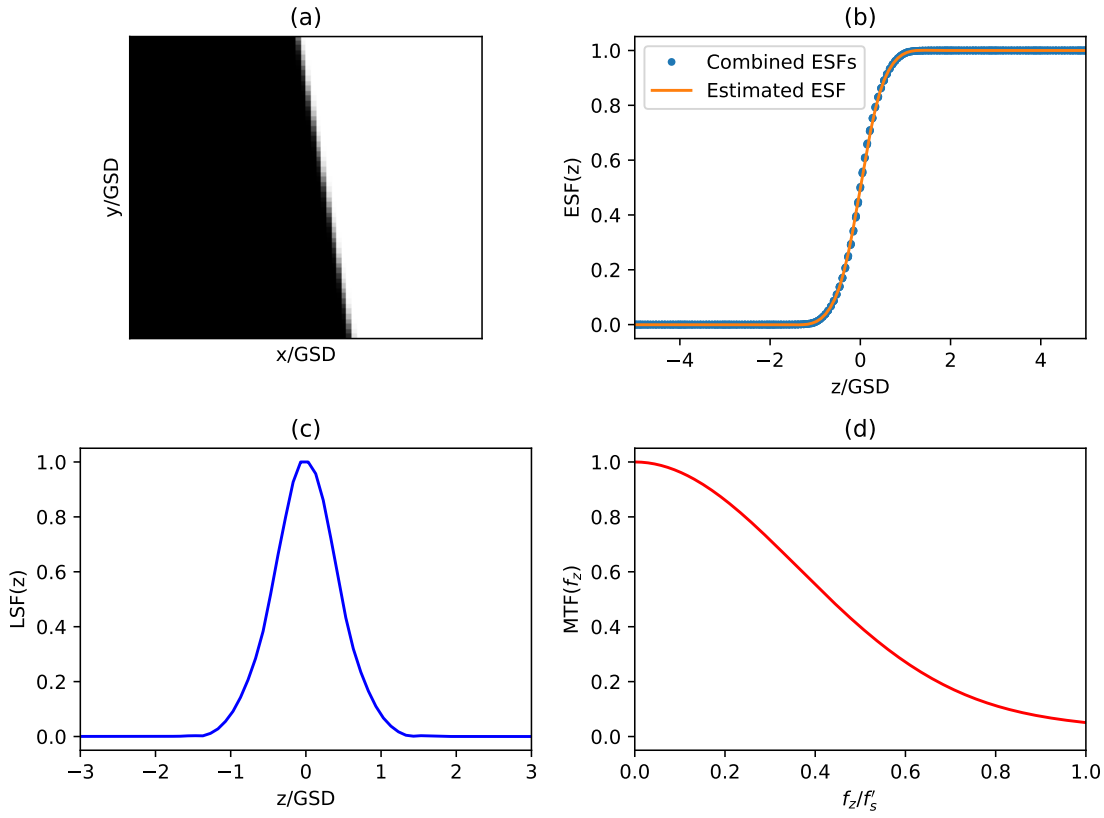

Figure 3.11: Slanted edge technique to estimate the MTF: (a) input image, (b) oversampled ESF, (c) calculated LSF, and (d) estimated MTF.

3.3.2 Pulse target

Another common target type used for MTF assessment is the pulse target. In this sense, bridges are typical ground targets which shape can be approximated by a pulse function. This technique requires a high resolution model of the pulse target, $r(z)$, and an oversampled profile of the pulse at the output of the satellite instrument, $o(z)$ [16, 17]. As in the slanted edge case, the z-axis represents the direction perpendicular to the pulse target. Once both $r(z)$ and $o(z)$ are calculated, the MTF is estimated using Equation 3.24:

$$MTF(f_z) = \frac{|o(f_z)|}{|r(f_z)|}, \tag{3.39}$$

where $o(f_z) = \mathcal{F}_z\{o(z)\}$ and $r(f_z) = \mathcal{F}_z\{r(z)\}$.

The high resolution model can be estimated from ground-based measurements or using high resolution satellite images (higher resolution than the instrument under consideration). If an ideal pulse is considered, the high resolution model is given by

$$r(z) = A \cdot \text{rect}\left(\frac{z}{W_z}\right), \tag{3.40}$$

being W_z the pulse width and A an amplitude factor. Therefore, as $r(f_z) = \mathcal{F}_z\{r(z)\} = AW_z \cdot \text{sinc}(W_z f_z)$, the MTF can be expressed as

$$MTF(f_z) = \frac{|o(f_z)|}{AW_z|\text{sinc}(W_z f_z)|}. \tag{3.41}$$

Keeping in mind that the $\text{sinc}(x)$ function is 0 for $x = 1, 2, 3, ...$, the above expression tends to $+\infty$ at spatial frequencies

$$f_z = \frac{n}{W_z}, \tag{3.42}$$

where $n = 1, 2, 3, ...$ This means that, nearby those frequencies, the MTF estimation error will increase considerably. Thus, as the interest frequency range for MTF evaluation is $0 < f_z < f_s'$, being $f_s' = 1/(GSD\cos(\theta))$, the following condition has to be fulfilled to avoid estimation errors:

$$\frac{1}{W_z} > f_s' \rightarrow W_z < GSD\cos(\theta). \tag{3.43}$$

The above condition ensures that the firs zero value of $r(f_z)$ is outside the spatial frequency region of interest, which reduces the estimation error. Therefore, at the first step, the high resolution pulse model $r(z)$ has to be estimated either using an analytical approach or using high resolution satellite images. If high resolution satellite images are used, the high resolution model has to be created by combining centered x-axis or y-axis profiles (depending on the estimation direction), and then projecting them onto the z-axis using Equation 3.32, as in the slanted edge case. Then, the output profile of the instrument $o(z)$ has to be calculated in a similar way, by centering, combining and projecting onto the z-axis different x-axis or y-axis profiles of the 2D image, therefore providing sub-pixel resolution.

Figure 3.12 shows an example of the MTF estimation process along the z-axis using a pulse target of width $W_x = (5/3) \cdot GSD$ along the across-track direction, and an inclination of $\theta = 10°$.

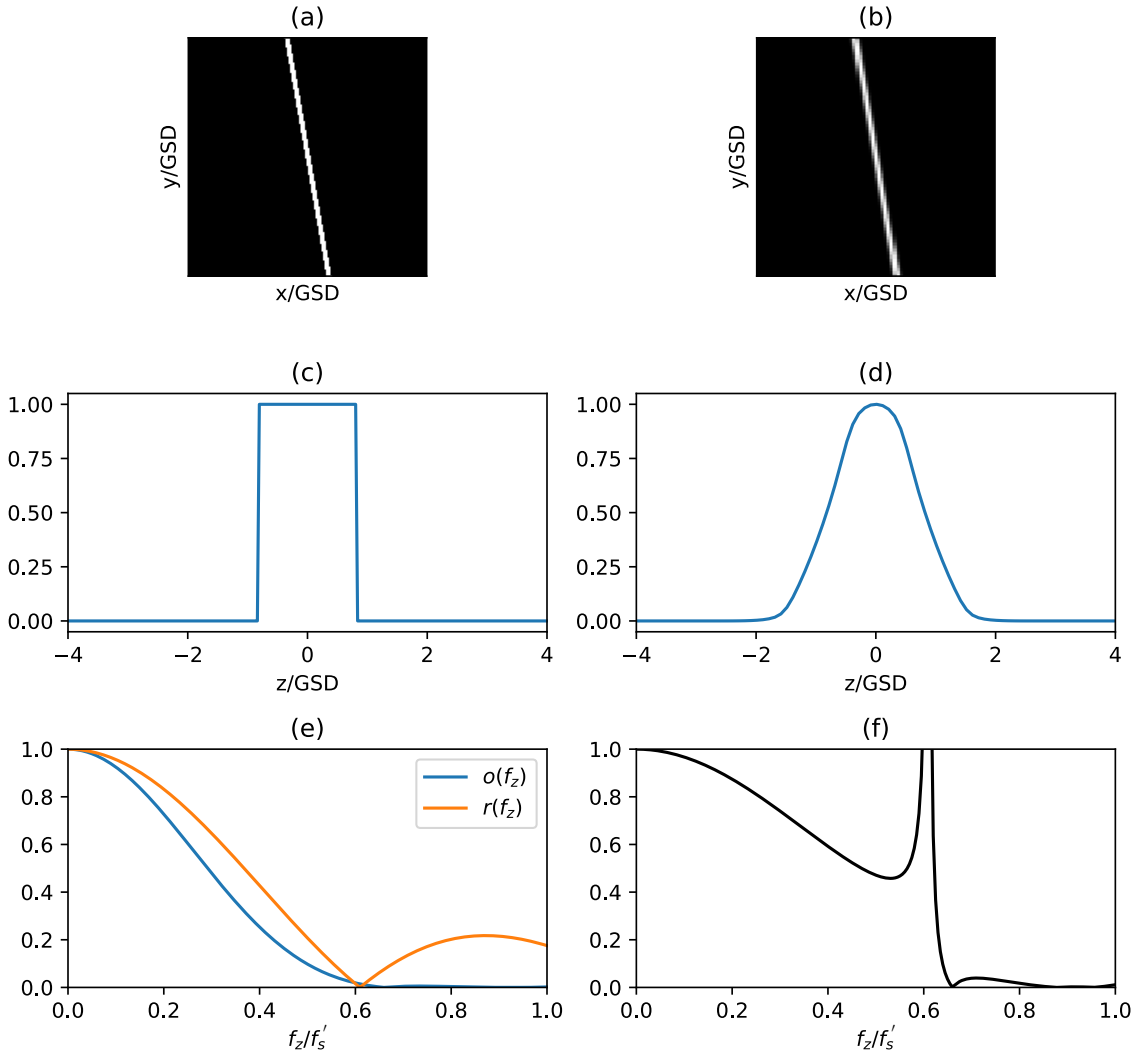

Figure 3.12: Pulse target technique to estimate the MTF: (a) high resolution image, (b) instrument image, (c) high resolution model $r(z)$, (d) output profile model $o(z)$, (e) Fourier transforms of $r(z)$ and $o(z)$, and (f) final estimated MTF. In this case, $W_z = (5/3) \cdot GSD\cos(\theta)$.

This W_x width translates onto a pulse width along the z-axis of $W_z = W_x\cos(\theta)$. Figures 3.12(a) and 3.12(b) correspond to the high resolution and the instrument images, respectively. Figure 3.12(c) shows the estimated high resolution profile $r(z)$ after combining several centered profiles along the x-axis and projecting them onto the z-axis, while Figure 3.12(d) shows the instrument filtered centered and oversampled profile $o(z)$. The Fourier transforms of both profiles are depicted in Figure 3.12(e) and, as can be observed, the Fourier transform of the pulse profile exhibits a zero value at the frequency $f_z/f_s' = GSD\cos(\theta)/W_z = 3/5 = 0.6$. Thus, this pulse target does not fulfill the condition established at Equation 3.43, which yields to the MTF estimation error near spatial frequencies $f_z/f_s' = 0.6$, as shown in Figure 3.12(f). To decrease this error, a narrower pulse target should be used.

If required, the LSF of the instrument can also be estimated as the inverse Fourier transform

of the MTF, that is,

$$LSF(z) = |\mathcal{F}_z^{-1}\{MTF(f_z)\}|. \tag{3.44}$$

3.3.3 Double-pulse target

The MTF can also be calculated from two pulse targets separated a distance d_z, following the same procedure as in the single pulse target case. This case corresponds, for instance, to a bridge with two spans. Thus, if we consider an ideal pulse model, the high resolution response is given by

$$r(z) = A \cdot \text{rect}\left(\frac{z + d_z/2}{W_A}\right) + B \cdot \text{rect}\left(\frac{z - d_z/2}{W_B}\right), \tag{3.45}$$

where A and W_A are the amplitude and width of the left span, respectively, and B and W_B are the amplitude and width of the right span.

The frequency response of this high resolution model can be calculated as

$$r(f_z) = AW_A \cdot \text{sinc}(W_A f_z)e^{j\pi d_z f_z} + BW_B \cdot \text{sinc}(W_B f_z)e^{-j\pi d_z f_z}. \tag{3.46}$$

If the width of both spans is approximately the same ($W_A \cong W_B \cong W_z$), which tends to be the case with real bridges, the above equation can be expressed as

$$r(f_z) = W_z \text{sinc}(W_z f_z)e^{-j\pi d_z f_z}\left(Ae^{j2\pi d_z f_z} + B\right). \tag{3.47}$$

Once the high resolution model is obtained, an oversampled profile of the instrument image has to be calculated, as in the single pulse target technique. Then, the MTF can be estimated using Equation 3.39:

$$MTF(f_z) = \frac{|o(f_z)|}{W_z|\text{sinc}(W_z f_z)\left(Ae^{j2\pi d_z f_z} + B\right)|}. \tag{3.48}$$

Analogously to the single pulse target case, the denominator in Equation 3.47 will tends to 0 for spatial frequencies multiple of $f_z = 1/W_z$, and therefore to avoid MTF estimation errors the condition of Equation 3.43 has to be fulfilled. In addition, from Equation 3.47, it can be deduced that the spatial frequency response of the high resolution model will have a local minimum when both bridge spans are in phase opposition, that is, $2\pi d_z f_z = (2n-1)\pi$, being $n = 1, 2, 3, ...$ This means that there will be additional MTF estimation errors near spatial frequencies

$$f_z = \frac{(2n-1)}{2d_z}. \tag{3.49}$$

Therefore, in order to reduce the estimation error of the destructive interference between the Fourier transform of both bridge spans, the following condition has to be fulfilled:

$$\frac{1}{2d_z} > f_s' \rightarrow 2d_z < GSD\cos(\theta). \tag{3.50}$$

Figure 3.13 depicts a simulation for a double pulse target with pulse widths $W_x = (3/10)\cdot GSD$ along the across-track directions, span separation $d_x = (13/15) \cdot GSD$, and equal amplitudes ($A = B = 1$), with an inclination of $\theta = 10°$. Thus, the double pulse target fulfills the first

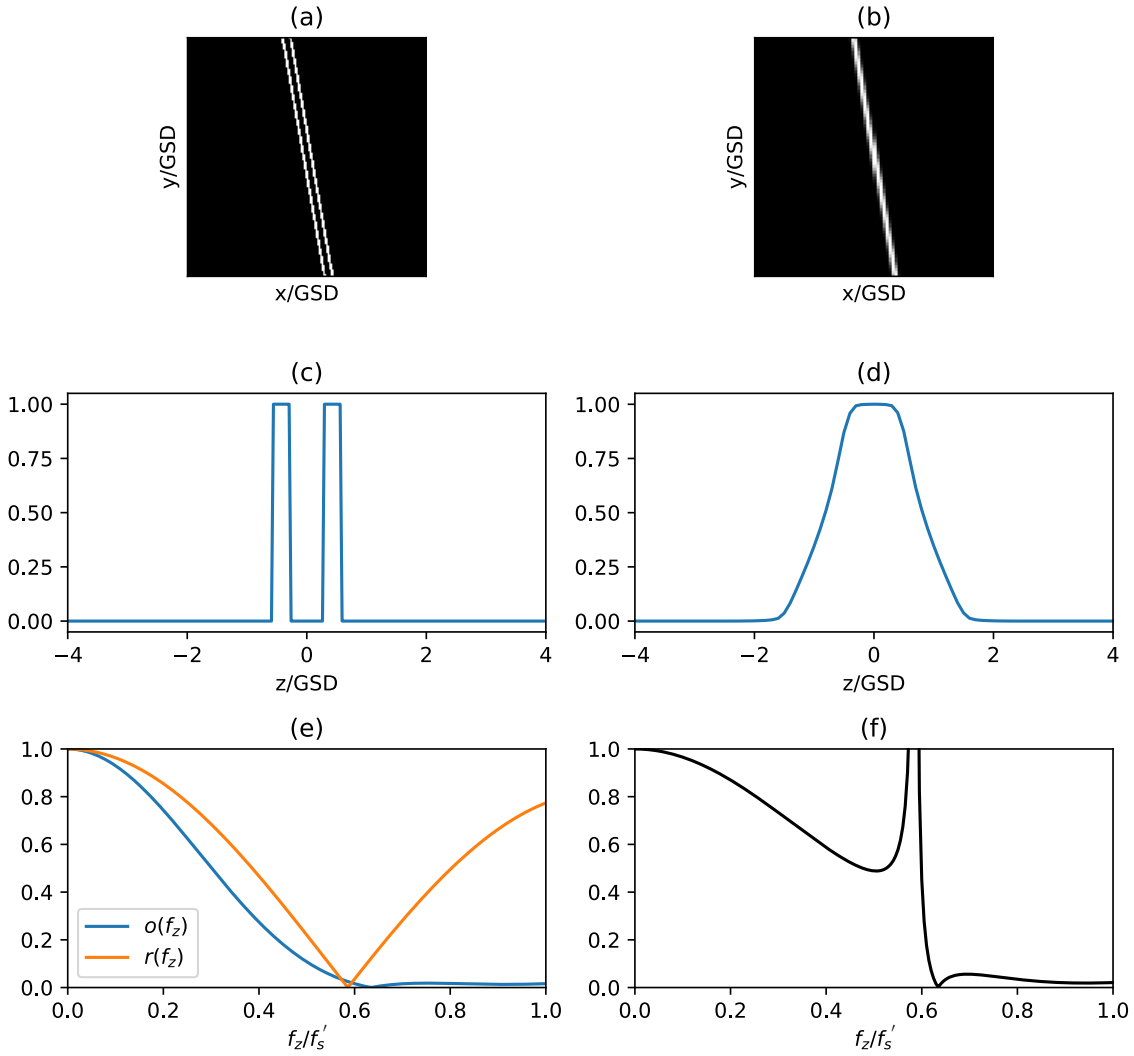

Figure 3.13: Double-pulse target technique to estimate the MTF: (a) high resolution image, (b) instrument image, (c) high resolution model $r(z)$, (d) output profile model $o(z)$, (e) Fourier transforms of $r(z)$ and $o(z)$, and (f) final estimated MTF. In this case, $W_z = (3/10) \cdot GSD\cos(\theta)$ and $d_z = (13/15) \cdot GSD\cos(\theta)$.

condition to avoid estimation errors, as $W_z < GSD\cos(\theta)$. However, the second condition is not fulfilled, as in this case $GSD\cos(\theta) < 2d_z$. Therefore, as shown in Figures 3.13(e) and 3.13(f), the spatial frequency response of the high resolution model is zero at $f_z/f_s' = 15/(2 \cdot 13) = 0.58$, which yields to high MTF errors near that frequency. To decrease the estimation error, the double-pulse ground target used to perform MTF estimations should have a shorter span separation.

3.4 Implemented estimation algorithms

Two MTF estimation algorithms have been developed for this work. One of them performs the MTF estimation using the slanted edge method, while the other performs the MTF estimation

using the pulse and double-pulse target techniques. Both algorithms have been implemented in Python 3.6.6 [19], a programming language widely used by scientist and engineers due to its easy programming workflow and good performance. The Python interpreter has been installed within the Anaconda distribution [20], which provides a large number of libraries commonly used for data science, signal processing, and artificial intelligence. Specifically, the developed algorithms make use of functions available in the Numpy [21], SciPy [22], Matplotlib [23], and Spectral python [24] libraries. The Numpy library provides useful functions for array data manipulation and basic math operations, the SciPy library provides optimized functions for cross-correlation and least-squares optimization problems (among many other), the Matplotlib library implements functions for data visualization; and the Spectral python library implements functions to read, write and manipulate spectral satellite data.

3.4.1 Slanted edge

The slanted edge algorithm is based on the theoretical model explained in Section 3.3.1. This MTF estimation approach is based on the ESF estimation. Thus, at the first step, each row profile $ESF_i(x)$ –or column $ESF_i(y)$, depending on the MTF estimation direction– of the slanted edge has to be centered. Once the different $ESF_i(x)$ are centered, they are combined to form a single oversampled $ESF(x)$. Then, the inclination angle of the slanted edge, θ, has to be estimated, which allows to project the $ESF(x)$ profile from the x or y-axis onto the z-axis, perpendicular to the contrast edge, which then has to be interpolated to provide an evenly sampled $ESF(z)$. Finally, the $LSF(z)$ is numerically calculated as the first derivative of the $ESF(z)$, and the $MTF(f_z)$ is obtained as the absolute value of the Fast Fourier Transform (FFT) of the $LSF(z)$.

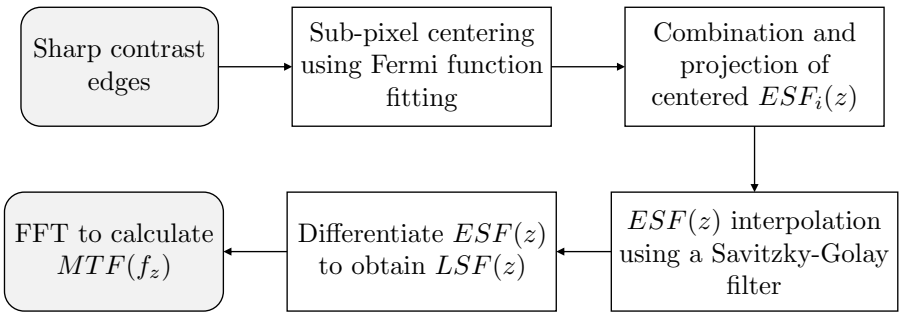

Figure 3.14: Flow diagram of the slanted edge estimation algorithm.

Figure 3.14 depicts a flow diagram of the different steps implemented to estimate the MTF. As shown in the figure, the first step is to center the different $ESF_i(x)$. This centering process is implemented fitting the $ESF_i(x)$ profile to a Fermi function, $f(x)$, which is given by

$$f(x) = \frac{a}{e^{-\frac{x-b}{c}} + 1} + d, \tag{3.51}$$

where a and d are amplitude constants, b is the center of the function, and c is a factor that controls the function slope.

Therefore, the different $ESF_i(x)$ are fitted to a Fermi function using a non-linear least square approach, available in the SciPy library, which minimizes the mean squared error between the Fermi function and the data. This allows to obtain the parameter b of the function, which can be

used to center each $ESF_i(x)$ profile with sub-pixel resolution. Figure 3.15 shows an example of a Fermi function fitted to a real $ESF_i(x)$ profile obtained from a L1C Sentinel-2 image. In this specific example, the center of the profile is located at the pixel $b = 1969.25$.

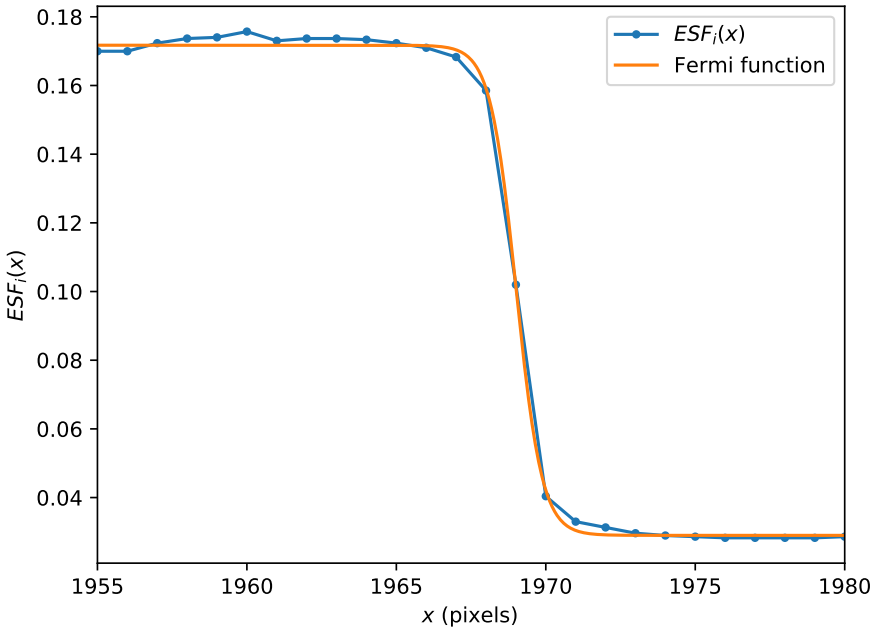

Figure 3.15: $ESF_i(x)$ **(blue) and Fermi function (orange) along the across-track direction.**

Once each $ESF_i(x)$ is centered, the center of each profile is used to estimate the inclination angle (θ) of the slanted edge. Thus, the center of each $ESF_i(x)$ profile is represented as a function of the y-axis, and then a linear function is fitted to the data:

$$b(y) = my + n, \tag{3.52}$$

where m is the line slope and n is a constant. Therefore, the inclination angle is estimated from the fitted line slope as

$$\theta = \tan^{-1}(m). \tag{3.53}$$

Figure 3.16 depicts the different steps of the $ESF_i(x)$ centering and edge angle estimation process for a contrast edge extracted from a real satellite image. Figure 3.16(a) shows the input slanted edge along the across-track direction, while Figure 3.16(b) shows the different $ESF_i(x)$ profiles obtained for each row of the image. Figure 3.16(c) depicts the different $ESF_i(x)$ profiles after being centered using a Fermi function fitting, and, finally, Figure 3.16(d) shows the center of each $ESF_i(x)$, $b(y)$, as a function of the y-axis. The linear fit of Figure 3.16(d) is used to estimate the inclination angle, which in this case is $\theta = 13.18°$.

The next step is to combine all $ESF_i(x)$ into a single $ESF_i(x)$. This is performed by arranging the different profiles into a single Numpy array. Once all the profiles are combined, the resulting $ESF(x)$ is projected onto the z-axis using Equation 3.32 and the edge inclination angle obtained from the linear fit. As the projected $ESF(z)$ is unevenly spatially sampled along the z-axis as

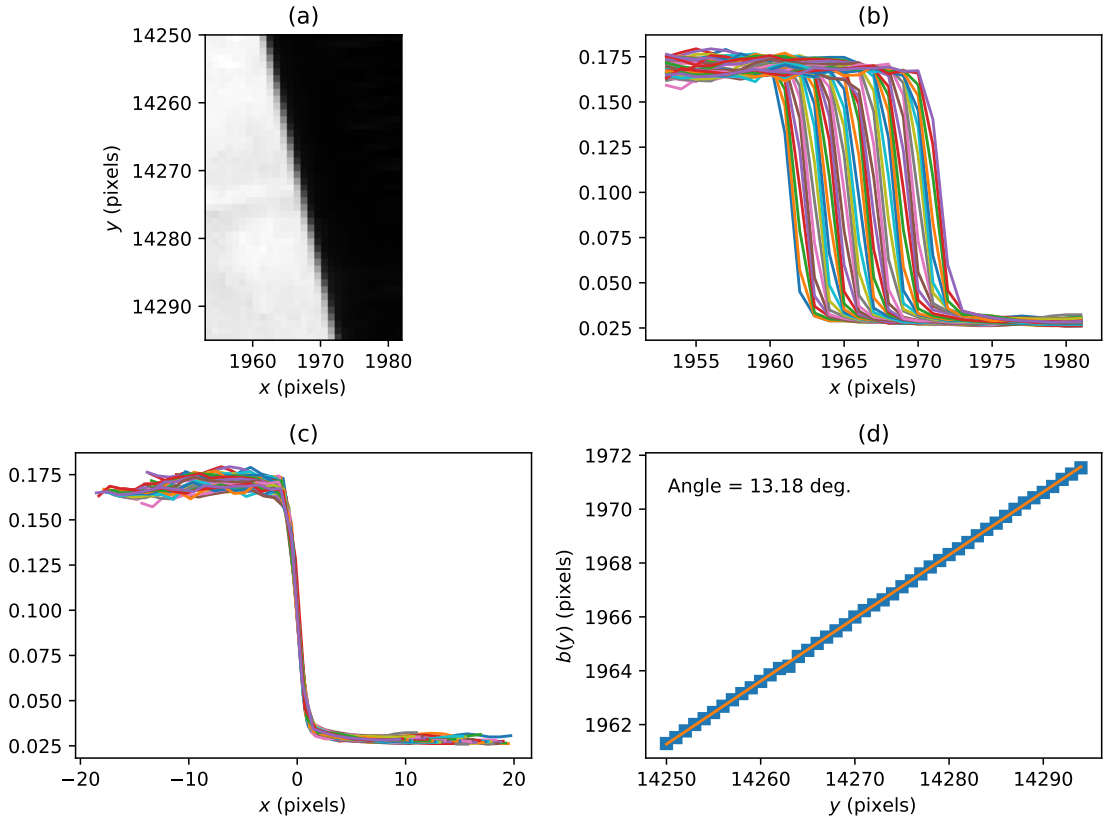

Figure 3.16: (a) Slanted across-track edge, (b) $ESF_i(x)$ profiles, (c) centered $ESF_i(x)$ profiles, and (d) center of each $ESF_i(x)$ as a function of y.

a consequence of the sub-pixel centering, the $ESF(z)$ has to be interpolated. This interpolation is performed using a modified Savitzky-Golay filter [10]. The Savitzky-Golay filter fits the input data to an M-degree polynomial function using a sliding-window. The pixel values that are within the range of the sliding window, are used to fit a polynomial function. The M-degree polynomial follows the equation

$$y_i = c_0 + c_1 u_i + c_2 u_i^2 + c_3 u_i^3 + \cdots + c_M u_i^M, \tag{3.54}$$

where u_i is the x-axis input value centered respect to the x-value of the output point, that is, $u_i = x_i - x_0$, being x_i the x-axis input point and x_0 the interpolated x-axis output point. The main objective of the filter is to calculate the different c_m coefficients of the polynomial. The output of the filter is given by the 0-degree coefficient of the polynomial, that is, c_0. Therefore, for a given group of (x_i,y_i) input points, where $i = 1, 2, ..., N$, being N the total number of points within the sliding window, the output value of the Savitky-Golay filter (x_0,y_0) can be calculated by solving a linear least squares problem. In matrix form, the problem can be expressed as

$$\begin{bmatrix} y_1 \\ y_2 \\ \vdots \\ y_N \end{bmatrix} = \begin{bmatrix} u_1 & u_1 & u_1^2 & \cdots & u_1^M \\ u_2 & u_2 & u_2^2 & \cdots & u_2^M \\ \vdots & \vdots & \vdots & \ddots & \vdots \\ u_N & u_N & u_N^2 & \cdots & u_N^M \end{bmatrix} \begin{bmatrix} c_0 \\ c_1 \\ \vdots \\ c_M \end{bmatrix}, \tag{3.55}$$

which in matrix notation is equivalent to

$$\mathbf{y} = \mathbf{U}\mathbf{c}. \tag{3.56}$$

The least-squares solution of the above equation is given by

$$\mathbf{c} = \left(\mathbf{U}^T\mathbf{U}\right)^{-1}\mathbf{U}^T\mathbf{y}, \tag{3.57}$$

where the superindex T represents the transpose matrix. Thus, for an M-degree polynomal fitting, $M+1$ points that are within the range of the sliding window are needed to fit the polynomial. Equation 3.57 is applied to calculate each (x_0,y_0) output point of the filter.

In this work, a 3-degree Savitzky-Golay filter is employed, with a sliding window width of 1.2 pixels. Figure 3.17 depicts as blue dots the input centered and oversampled $ESF(z)$ profile obtained by combining and projecting the different $ESF_i(x)$ shown in Figure 3.16(c) onto the z-axis. The z-axis of the figure is converted from pixel to metric units by multiplying by the GSD, which in this case is $GSD = 10$ m. Figure 3.17 also depicts in orange color the interpolated $ESF(z)$ profile calculated using a 3-degree Savitzky-Golay filter with a window width of 1.2 pixels. The interpolation is implemented with a resolution of $1/10$ pixels.

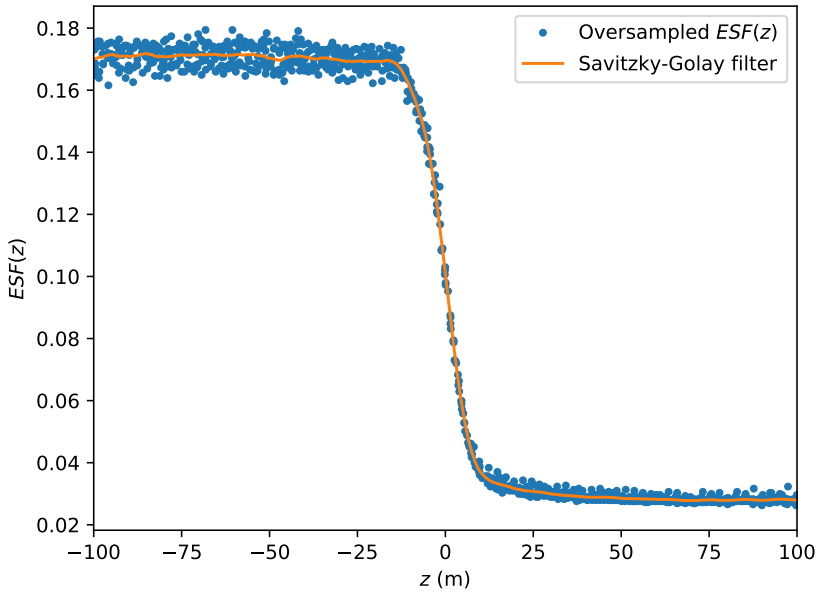

Figure 3.17: Centered and projected $ESF(z)$ (blue) and interpolated $ESF(z)$ using a 3-degree Savitzky-Golay filter (orange).

Following the flow diagram of Figure 3.14, the next step is to calculate the first derivative the interpolated $ESF(z)$ profile which, as demonstrated in section 3.3.1, provides the $LSF(z)$. This derivative is numerically calculated for each z_i point using the gradient function of the Numpy library, which calculates the derivative using second order accurate central differences:

$$LSF(z_i) \cong \frac{ESF(z_{i+1}) - ESF(z_{i-1})}{2\Delta_i}, \tag{3.58}$$

where Δ_i represents the interpolation resolution, measured in pixels, which in this case is $\Delta_i = 1/10$ pixels.

Once the $LSF(z)$ is calculated, the final step is to estimate the $MTF(f_z)$ response of the instrument, which can be directly calculated as

$$MTF(f_z) = |\text{FFT}_{n_{fft}}\{LSF(z)\}|, \tag{3.59}$$

where $\text{FFT}_{n_{fft}}\{\cdot\}$ represents the Fast Fourier Transform operation with n_{fft} spatial frequency points. At this step, it is worth noting that, in order to avoid estimation errors, the spatial frequency axis, f_z, has to be calculated carefully. Thus, the discrete spatial frequency axis, f_z^d, can be calculated as a uniform array ranging from 0 to $(n_{fft}-1)/n_{fft}$ with $1/n_{fft}$ steps. This discrete frequency axis can be then converted to a continuous spatial frequency array by multiplying all its values by the spatial sampling frequency, which is calculated as $f_s^i = 1/\Delta z_i$, being Δz_i the spatial resolution of the $LSF(z)$ along the z-axis. In this case, the spatial resolution is given as a function of the $LSF(z)$ interpolation resolution, the GSD of the instrument, and the inclination angle of the edge:

$$\Delta z_i = \Delta_i \Delta z, \tag{3.60}$$

where Δz is the sampling distance of the satellite projected onto the z-axis. Therefore, using Equation 3.34, the continuous spatial frequency axis, measured in m^{-1}, can be finally calculated as

$$f_z = f_z^d \cdot f_s^i = \frac{f_z^d}{\Delta_i \Delta z} = \frac{f_z^d}{\Delta_i GSD \cos(\theta)}. \tag{3.61}$$

Usually, the spatial frequency axis is represented normalized by the sampling frequency of the instrument along the z-axis, $f_s' = 1/(GSD\cos(\theta))$, which finally yields to

$$f_z/f_s' = \frac{f_z^d}{\Delta_i}. \tag{3.62}$$

Figures 3.18(a) and 3.18(b) show the $LSF(z)$ profile calculated from the interpolated $ESF(z)$ depicted in Figure 3.17, and the $MTF(f_z)$ response calculated from the $LSF(z)$, respectively. The spatial resolution of the instrument can be obtained from the $LSF(z)$ depicted in Figure 3.18(a). In this particular case, the instrument presents an across-track resolution of $FWHM_x = 12.3$ m. However, it is worth noting that, as discussed in section 3.3.1, this is not exactly the across-track resolution, but the resolution along the z-axis, which, given that $\theta = 13.18°$, should be very similar to the actual across-track value. On the other hand, Figure 3.18(b) depicts the $MTF(f_z)$ response, calculated with $n_{fft} = 2048$ frequency points. As shown in the figure, the MTF value at Nyquist frequency ($f_z/f_s' = 0.5$) is $MTF^{nyq} = 0.235$. As stated in previous sections, this is a good trade-off MTF^{nyq} value between resolution and aliasing.

3.4.2 Pulse and double-pulse targets

The pulse target algorithm is based on the theoretical models described in sections 3.3.2 and 3.3.3. As both single and double-pulse target approaches are very similar, they can be implemented using a single algorithm. Figure 3.19 shows a flow diagram of the different algorithm steps. Basically, the objective of the method is to obtain a high resolution model of the pulse or double-pulse target ($r(z)$) using high resolution images of the target, and to obtain a model of the target filtered by the

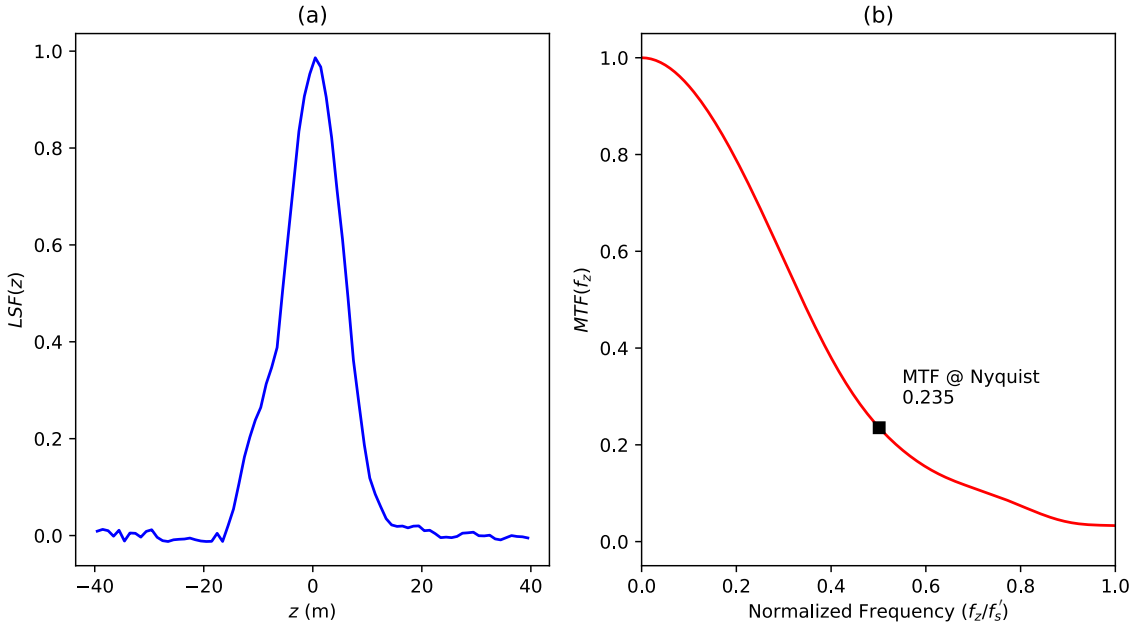

Figure 3.18: (a) Calculated $LSF(z)$ profile and (b) estimated $MTF(f_z)$ response.

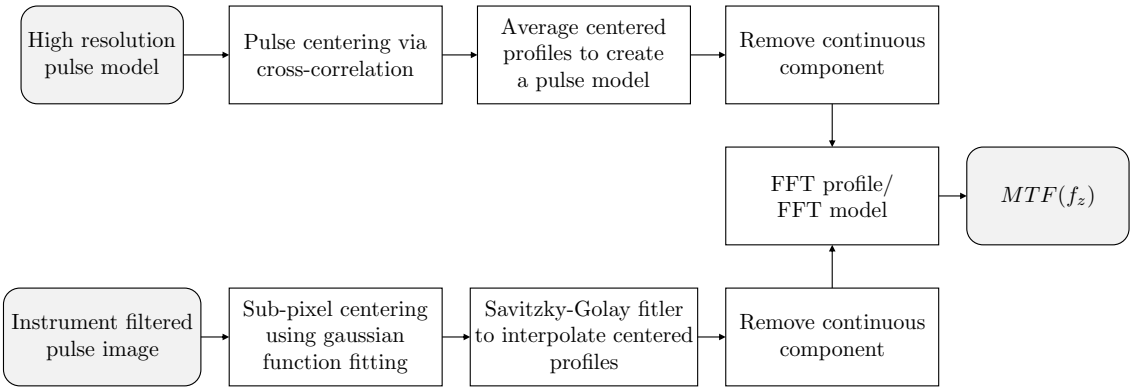

Figure 3.19: Flow diagram of the pulse and double-pulse target estimation algorithm.

instrument ($o(z)$) using satellite images. Once both models are obtained, the MTF is calculated using Equation 3.39.

The high resolution model is created by averaging centered profiles of the high resolution image. Thus, at the first step, each $r_i(x)$ (or $r_i(y)$, if the target is aligned across-track) profile, where $i = 1, 2, ..., N$, being N the total number of target profiles, is centered using a cross-correlation method. Thus, a cross-correlation function $\phi(x)$ of each $r_i(x)$ with a reference $r_0(x)$ profile of the target is calculated as

$$\phi(x) = \int r_i(\tau) r_0(\tau - x) d\tau. \tag{3.63}$$

In discrete form, this cross-correlation is given by

$$\phi[x_i] = \sum_{\tau=0}^{L_r-1} r_i[\tau] r_0[\tau - x_i], \tag{3.64}$$

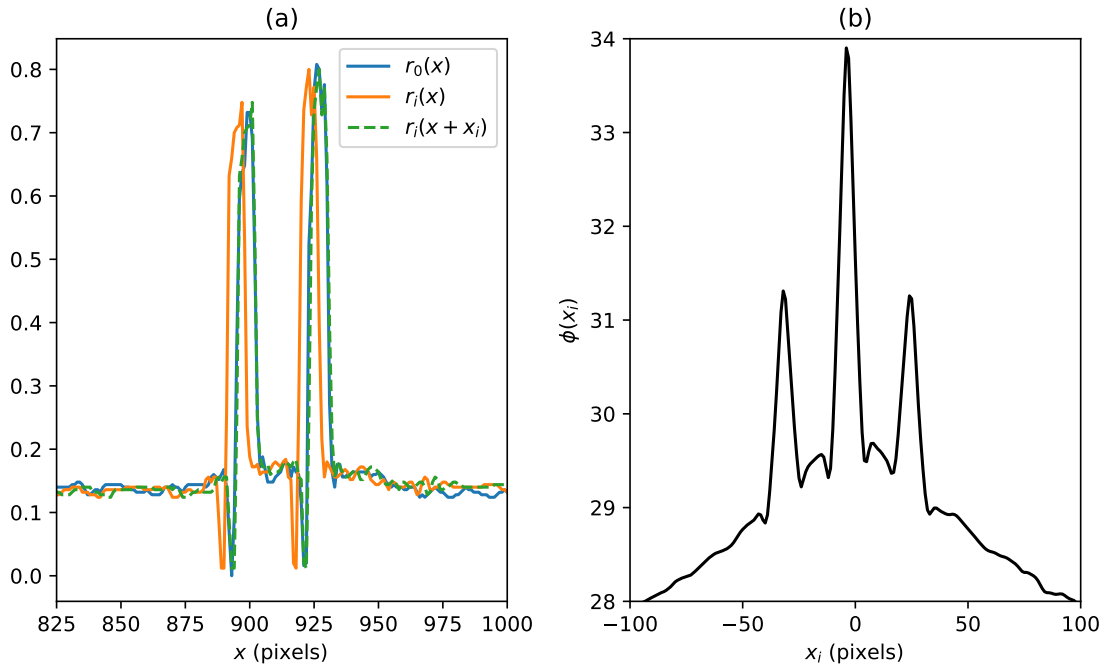

Figure 3.20: (a) reference $r_0(x)$ profile (blue), $r_i(x)$ profile (orange), and centered $r_i(x+x_i)$ (dashed green); (b) cross-correlation function $\phi(x_i)$.

where L_r is the length of both arrays. Therefore, when the two profiles $r_i(x)$ and $r_0(x)$ overlap completely, the cross-correlation function reaches its maximum value. Thus, once the cross-correlation function is calculated, the x_i point at which it reaches the maximum value is considered as the shift of the $r_i(x)$ profile respect to the $r_0(x)$ reference, such as that $r_i(x) \cong r_0(x - x_i)$. This means that the $r_i(x)$ profile is centered as $r_i(x + x_i)$. Thus, all $r_i(x)$ profiles will be centered respect to the reference $r_0(x)$ profile. This $r_0(x)$ reference profile can be selected arbitrarily among the different $r_i(x)$. Once all $r_i(x)$ profiles are centered, the high resolution model is created as the average of all profiles. Then, the inclination angle of the target, θ, is estimated similarly to the slanted edge case, by fitting a linear function to the different x_i centers along the y-axis. Thus, once θ is calculated using Equation 3.53, the averaged high-resolution profile is projected onto the z-axis using Equation 3.32.

Figure 3.20 depicts an example of the centering process of a double-pulse target using the cross-correlation function. Figure 3.20(a) depicts the reference profile $r_0(x)$, the $r_i(x)$ profile, and the centered $r_i(x+x_i)$ profile. As can be observed, both $r_0(x)$ and $r_i(x+x_i)$ profiles overlap perfectly, meaning that the centering algorithm provides the desired outcome. The x_i value used to center the profile is extracted from the cross-correlation $\phi(x_i)$ function shown in Figure 3.20(b). As seen in the figure, $\phi(x_i)$ has a maximum value at $x_i = -4$, which is exactly the moment when both profiles overlap. Finally, Figure 3.21 shows the final $r(x)$ high resolution double-pulse model obtained by averaging the centered $r_i(x)$ profiles.

Once the high resolution model is created, its continuous component has to be removed in order to avoid MTF estimation errors. Let $r'(z)$ be the high resolution model of the target with a

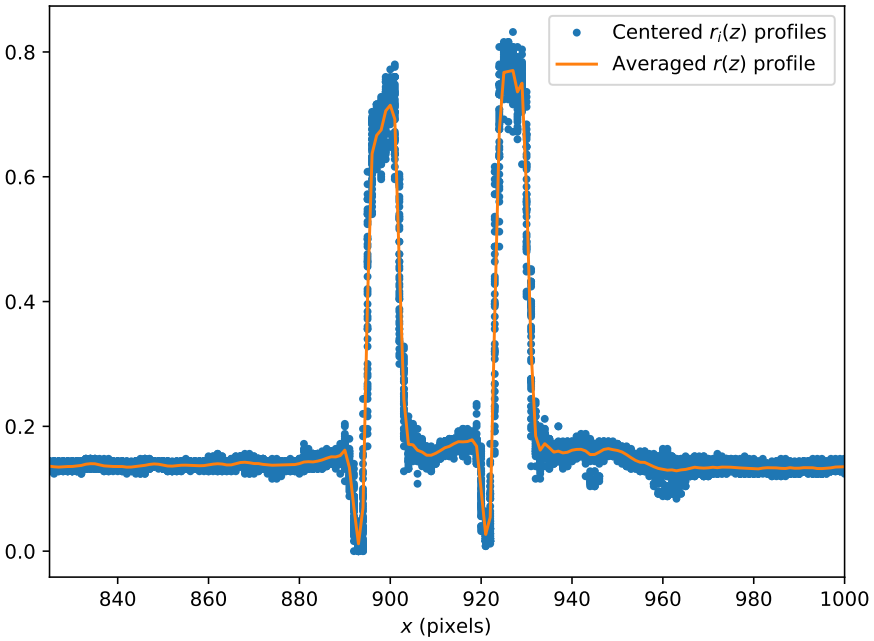

Figure 3.21: High-resolution model $r(x)$ (orange) created by averaging the different combined $r_i(x)$ profiles (blue dots).

continuous component, defined as

$$r'(z) = r(z) + K \cdot \text{rect}\left(\frac{z}{L_z}\right), \tag{3.65}$$

where K is a constant value, i.e. the continuous component of the model, and L_z is the observation window length of the model. $r(z)$ is the ideal target model without the continuous component. The frequency response of the model will be given by

$$r'(f_z) = \mathcal{F}_z\{r'(z)\} = r(f_z) + KL_z \cdot \text{sinc}(Lzf_z). \tag{3.66}$$

Thus, the sinc$(L_z f_z)$ term of Equation 3.66 will cause estimation errors, specially for the low frequency components of the MTF. Indeed, the narrower the observation window of the high resolution model, the higher the estimation error, as the sinc$(L_z f_z)$ term gets wider. Therefore, it is important to remove the continuous component of the model to avoid this kind of error.

On the other hand, as described in the flow diagram of Figure 3.19, the different $o_i(x)$ profiles of the instrument filtered image have to be centered and combined to create a filtered $o(x)$ model of the target. The centering process is achieved using a 1D gaussian function fitting, which provides sub-pixel accuracy. Once the different profiles are centered, they are combined into a single array to obtain an oversampled $o(x)$ profile, and then projected onto the z-axis. Similarly to the slanted edge case, the oversampled profile is unevenly sampled and, therefore, a 3-degree Savitzky-Golay filter is used to create an interpolated $o(z)$ profile. Then, as in the $r(z)$ case, the continuous component of the model is removed. Finally, the MTF is calculated as

$$MTF(f_z) = \frac{|\text{FFT}_{n^o_{fft}}\{o(z)\}|}{|\text{FFT}_{n^r_{fft}}\{r(z)\}|}, \tag{3.67}$$

where n^o_{fft} and n^r_{fft} represent the number of frequency points of the filtered model and the high resolution model. It is important to keep in mind that, in order to be able to calculate the above equation, both model and filtered target frequency responses have to be evaluated at the same frequency points. Fulfilling this condition requires that

$$\frac{f^o_s}{n^o_{fft}} = \frac{f^r_s}{n^r_{fft}}, \tag{3.68}$$

with $f^o_s = 1/(\Delta_i GSD_o \cos(\theta))$ and $f^r_s = 1/(GSD_r \cos(\theta))$ being the sampling frequencies of the interpolated filtered target model and the high resolution model, respectively. Analogously to the slanted edge case, Δ_i represents the interpolation resolution of the Savitzky-Golay filter, measured in pixels. Thus, the above condition can be finally expressed as

$$n^r_{fft} = \frac{\Delta_i GSD_o}{GSD_r} \cdot n^o_{fft}. \tag{3.69}$$

The procedure used in this work consists on fixing n^o_{fft}, and then calculate the resolution of the Savitzky-Golay filter Δ_i so that n^r_{fft} is an integer multiple of n^o_{fft}. As in the slanted edge method, if the MTF response is represented as a function of the normalized frequency axis, f_z must be normalized by the sampling frequency along the z-axis, that is, $f'_s = 1/(GSD_o \cos(\theta))$.

Figure 3.22 shows the MTF estimation results for a real satellite image of a bridge with two spans. In this case, the high-resolution model has a spatial sampling resolution of $GSD_r = 0.9$ m, while the spectral instrument has a sampling resolution of $GSD_o = 30$ m. The number of frequency points of the filtered profile is set to $n^o_{fft} = 2048$ points and the interpolation resolution is set to $\Delta_i = 0.3$ pixels, which yields to a number of high-resolution model frequency points of $n^r_{fft} = 20480$ points. Figures 3.22(a) and 3.22(b) represent the high-resolution image and the instrument filtered image, respectively, whereas Figures 3.22(c) and 3.22(d) represent their corresponding high-resolution profile $r(z)$ and instrument filtered profile $o(z)$, before removing the continuous component. Using the high resolution model of Figure 3.22(c), the bridge dimensions can be estimated. Thus, the width of each span bridge is $W_z \cong 8.5$ m and the span separation is $d_z \cong 25.3$ m, with an inclination of $\theta = -8.96°$. With these dimensions, the double-pulse target only fulfills the first of the two conditions required to avoid MTF estimation errors explained in section 3.3.3. The first condition requires that the width of each span is lower than the sampling distance of the satellite instrument, that is, $GSD_o \cos(\theta) > W_z$, which in this case is fulfilled by a considerable margin. In contrast, the second condition does not hold, as in this case $GSD_o \cos(\theta) > 2d_z$. This means that the frequency response of the high-resolution model, $r(f_z)$, has its first local minimum at the normalized frequency

$$f_z/f'_s \cong \frac{GSD_o \cos(\theta)}{2d_z} = 0.586, \tag{3.70}$$

as described by Equation 3.49. This local minimum can be clearly observed at Figure 3.22(e), which represents both the high-resolution and the filtered model frequency responses. Therefore, as expected from the results discussed in section 3.3.3, the MTF response depicted in Figure 3.22(f) presents a large estimation error in the spatial frequencies nearby the first local minimum of the high-resolution model. Thus, for this specific bridge, the MTF value at Nyquist frequency can not be estimated from this image using the double-pulse target approach.

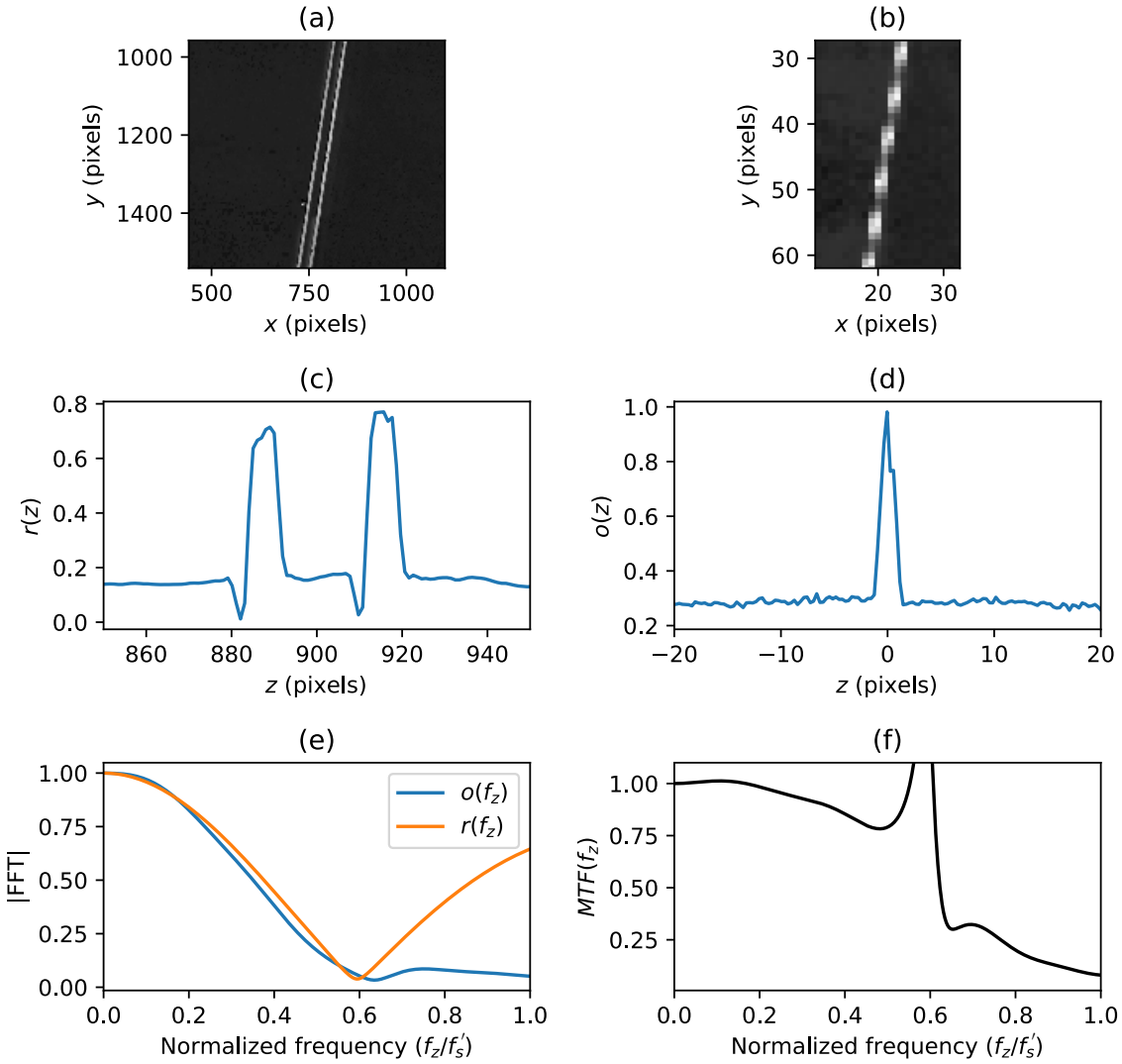

Figure 3.22: Results of a real double-pulse target MTF estimation: (a) high-resolution image, (b) instrument filtered target, (c) averaged $r(z)$ model, (d) interpolated $o(z)$ profile, (e) spatial frequency responses of both profiles, and (f) estimated $MTF(f_z)$ response.

3.4.3 Discussion

Both estimation algorithms presented in this chapter have advantages and disadvantages. On the one hand, the slanted edge algorithm does not require a high resolution model. However, it does not estimate the MTF exactly in the across-track nor the along-track, as it performs the estimation in the direction perpendicular to the edge. This restriction is intrinsic to the theoretical model, as the derivative of the step function is a delta function only in the direction perpendicular to the edge. On the other hand, the pulse and double-pulse target techniques are able to estimate the MTF using targets smaller than the pixel size. However, the estimation can yield to high estimation errors depending on the bridge/target dimensions, and the MTF is estimated along the perpendicular axis to the target, as in the slanted edge case. In addition, the estimation also requires a high-resolution model of the target, which cannot always be obtained.

Overall, the slanted edge approach is preferred over the pulse or double-pulse target technique in the literature, as it can be used without needing any high-resolution model, and only the instrument image is required. Moreover, it avoids the estimation errors caused by the pulse width or the span separation.

Chapter 4

Results

4.1 Sensitivity analysis

In order to test the performance of both slanted edge and pulse/double-pulse target MTF estimation methods, an ideal simulation algorithm has been developed. The main objective of this task is to generate either perfect slanted edges or pulse/double-pulse targets filtered with an input PSF function, and sampled at the desired output GSD. Thus, the input PSF can be specified from its resolution ($FWHM$ in the across-track and along-track directions), or from the MTF response. As both PSF and MTF are known, the performance of the algorithms can be tested by comparing the estimated responses with the input responses.

The main steps of the ideal simulation algorithm are:

1. Create an ideal high-resolution slanted edge or pulse/double-pulse target, with a sampling distance GSD_{in}.

2. Calculate the instrument PSF. The PSF is calculated as an ideal 2D Gaussian function (Equation 3.9). In this case, the input parameters are the total PSF resolutions $FWHM_x$ and $FWHM_y$. The MTF response is calculated from the PSF. The sampling distance of the PSF is the same as in the ideal target case, that is, GSD_{in}.

3. Perform a 2D convolution of the ideal target and the generated PSF. The convolution is performed in the spatial domain.

4. Resample the filtered target at the specified output sampling distance, GSD_{out}.

Figure 4.1 depicts the output of the different steps of the ideal simulation algorithm. As can be observed, first, the ideal target and the instrument PSF are generated, with a resolution GSD_{in}. In this particular case, the high-resolution sampling distance is $GSD_{in} = 1$ m, and the target is a slanted edge with an inclination of $\theta = 10°$. The PSF resolution is $FWHM = 32$ m for both across-track and along-track directions. The output spatial sampling distance is set to $GSD_{out} = 30$ m. In order to obtain an accurate convolution result, the ideal edge sampling distance has to be considerably lower than the PSF resolution. A value of $GSD_{in} = GSD_{out}/10$ or lower is recommended. Finally the filtered target image is obtained by performing a 2D convolution of the

PSF and the ideal target, and the output filtered image is obtained by resampling the filtered image at GSD_{out}. As the GSD_{out} is set to an integer multiple of GSD_{in}, no interpolation is required.

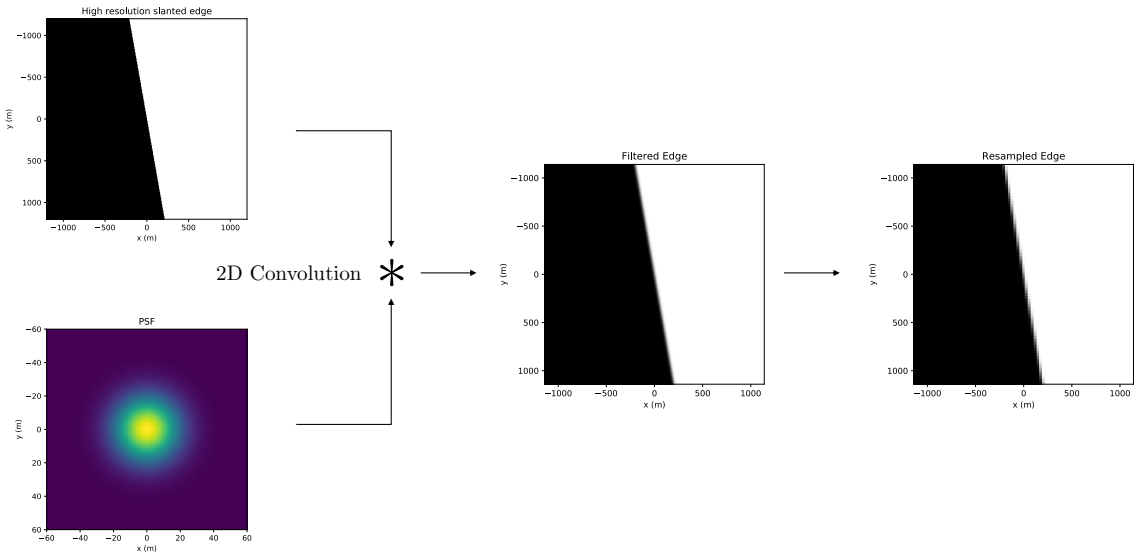

Figure 4.1: Schematic view of the ideal simulation steps.

4.1.1 Slanted edge

The slanted edge simulations have been performed for three different GSD values: 10, 20, and 30 m. For each GSD, $FWHM$ resolutions ranging from $1GSD$ to $2GSD$ have been simulated, with equal resolution in both across-track and along-track. In addition, two edge inclinations have been considered: $\theta = 8°$ and $\theta = 10°$.

Figure 4.2 represents the simulation results for the three GSD cases. Figures 4.2(a) and 4.2(b) correspond to $GSD = 10$ m, while 4.2(c) and 4.2(d) correspond to $GSD = 20$ m, and 4.2(e) and 4.2(f) correspond to $GSD = 30$ m. The left column (Figures 4.2(a), 4.2(c), and 4.2(e)) represents the estimated resolution $FWHM_z$ as a function of the simulated resolution, whereas the right column (Figures 4.2(b), 4.2(d), and 4.2(f)) shows the corresponding $FWHM_z$ estimation errors, given also as a function of the simulated resolution. The estimation error, $FWHM_e$, is defined as

$$FWHM_e = FWHM_z^{sim} - FWHM_z^{est}, \tag{4.1}$$

being $FWHM_z^{sim}$ and $FWHM_z^{est}$ the simulated and estimated PSF resolutions, respectively.

As can be observed from Figure 4.2, the algorithm provides an accurate estimation of the instrument resolution, obtaining similar results for both $\theta = 8°$ and $\theta = 10°$ edge inclinations. In addition, in all three GSD cases the algorithm provides analogous results, showing a similar error tendency. The maximum estimation errors of approximately 0.4 m for the $GSD = 10$ m case, 0.8 m for the $GSD = 20$ m case, and 1.35 m for the $GSD = 30$ m case.

Table 4.1 shows the accuracy and precision parameters for both $\theta = 8°$ and $\theta = 10°$ edge inclination cases. All the results are normalized by the corresponding GSD of each simulation. The accuracy, μ_e^{fwhm}, is calculated as the mean value of the resolution estimation error, while the precision, σ_e^{fwhm}, is defined as the standard deviation of the estimation error. As shown in the

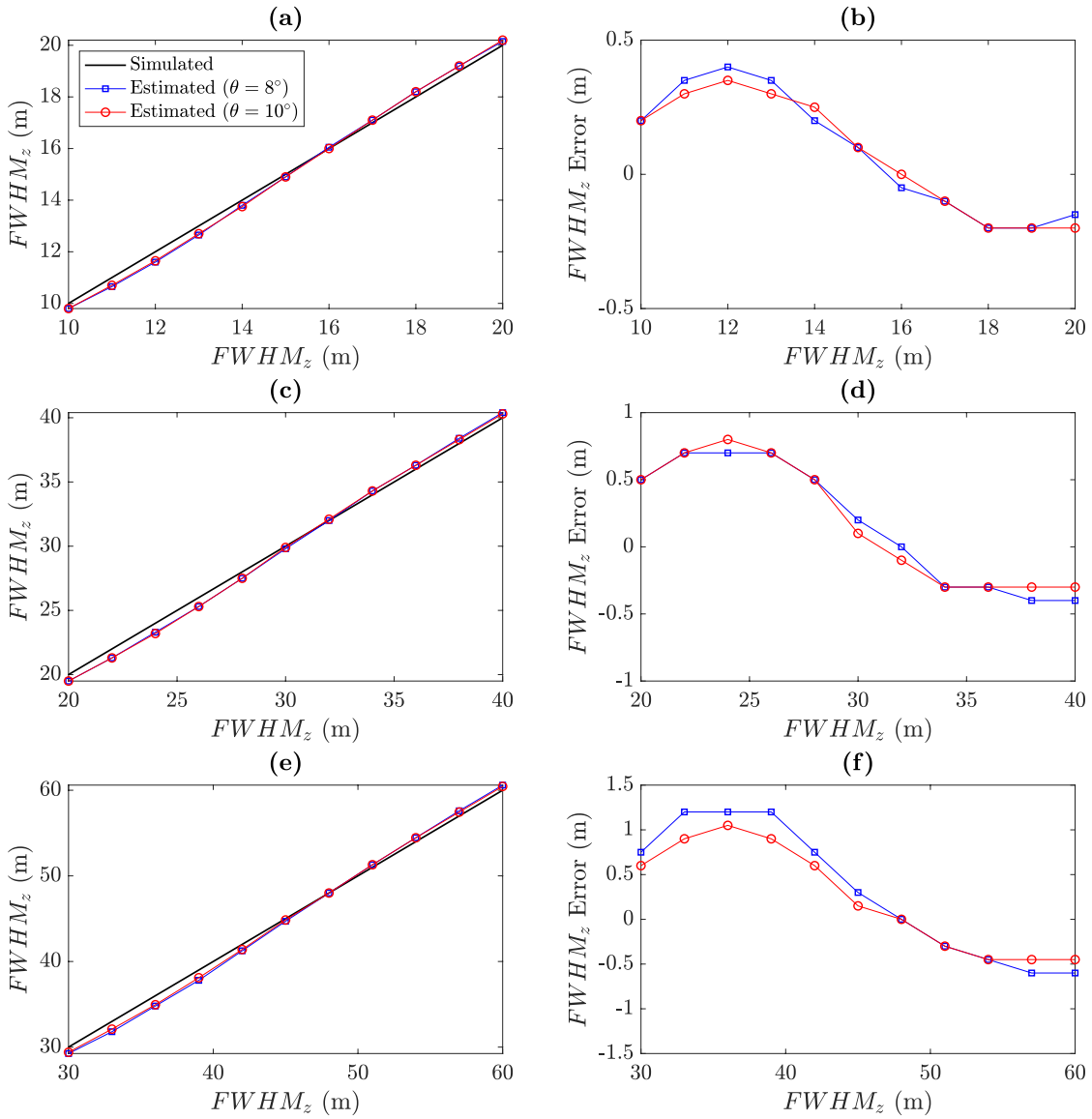

Figure 4.2: Slanted edge algorithm: (a, c, e) estimated $FWHM_z$ and (b, d, f) estimation error $FWHM_e$ as a function of the simulated $FWHM_z$. (a, b) correspond to $GSD = 10$ m,(c, d) correspond to $GSD = 20$ m, and (e, f) correspond to $GSD = 30$ m.

table, the algorithm performs similarly for all GSD cases. This happens because the simulated resolution range is the same in terms of the GSD in the three cases, that is, for each GSD, the $FWHM$ is shifted from $FWHM = 1GSD$ to $FWHM = 2GSD$, at $0.1GSD$ steps. Thus, the estimation performance depends on the $FWHM/GSD$ ratio. The global accuracy of the algorithm for the $\theta = 8°$ slanted edge, calculated as the mean value between the three accuracies, is $\mu_e^{fwhm} = 0.0091 \cdot GSD$ (0.91% of the GSD), while the global precision is $\sigma_e^{fwhm} = 0.024 \cdot GSD$ (2.4% of the GSD). On the other hand, for the $\theta = 10°$ slanted edge, the global accuracy is $\mu_e^{fwhm} = 0.0089 \cdot GSD$ (0.89% of the GSD) and the global precision is $\sigma_e^{fwhm} = 0.023 \cdot GSD$ (2.3% of the GSD), which are very similar to the $\theta = 8°$ case.

θ (°)	GSD (m)	μ_e^{fwhm} (GSD)	σ_e^{fwhm} (GSD)
8	10	0.00818	0.02316
	20	0.00864	0.02336
	30	0.01045	0.02464
10	10	0.00727	0.02206
	20	0.00909	0.02311
	30	0.01045	0.02285

Table 4.1: Resolution estimation: accuracy (μ_e^{fwhm}) and precision (σ_e^{fwhm}) parameters normalized by the GSD.

Figure 4.3 depicts the MTF estimation results of the ideal slanted edge simulations. The left column of the figure represents the estimated MTF values at Nyquist frequency as a function of the simulated resolution $FWHM$, while the right column depicts the MTF estimation errors at Nyquist for each case, also as a function of the simulated $FWHM$. The first row of the figure shows the results of the $GSD = 10$ m case, the second row corresponds to $GSD = 20$ m, and the third row depicts the $GSD = 30$ m results. Analogously to the resolution error, the MTF estimation error, MTF_e, is defined as

$$MTF_e = MTF_z^{sim} - MTF_z^{est}, \tag{4.2}$$

where MTF_z^{sim} and MTF_z^{est} correspond to the simulated and estimated MTF values at Nyquist frequency, respectively. As shown in the figure, the algorithm provides a good MTF^{nyq} estimation, showing similar error tendencies in all GSD cases. In addition, the estimation error of the $\theta = 10°$ case is almost exactly the same than that of the $\theta = 8°$ case. Simulations show that good MTF estimations are obtained for inclination angles between $\theta = 5°$ and $\theta = 20°$, although the error increases with θ, as reported in [10, 14]. Moreover, it is important to use edge inclination and GSD combinations that provide a uniformly sampled oversampled ESF. If the GSD and θ combination is not optimum, the oversampled ESF profile will present data points clustered together, which can yield to bad ESF interpolation results. For instance, Figure 4.4(a) shows the ESF interpolation results for $\theta = 8°$ and $GSD = 30$ m, whereas Figure 4.4(b) represents the ESF results for $\theta = 10°$ and $GSD = 30$ m. As can be observed, the $\theta = 8°$ edge inclination provides a more uniform oversampled ESF, especially at the slope of the ESF.

Table 4.2 represents the MTF estimation accuracy (μ_e^{mtf}) and precision (σ_e^{mtf}) parameters of the algorithm for the three GSD and the two considered edge inclinations. In this case, the global accuracy and precision of the algorithm are $\mu_e^{mtf} = 0.0059$ and $\sigma_e^{mtf} = 0.0035$ for both $\theta = 8°$ and $\theta = 10°$ inclinations.

4.1.2 Pulse target

Pulse target simulations have been carried out considering a pulse width of $W = 0.8GSD$, which fulfills Equation 3.43 to avoid high MTF estimation errors. As in the slanted edge case, the simulations have been performed for PSF resolutions ranging from $FWHM = 1GSD$ to $FWHM = 2GSD$, at $0.1GSD$ steps. In this case, a pulse inclination of $\theta = 8°$ has been considered. Figures 4.5(a) and 4.5(b) represent the estimated resolution and the estimation error,

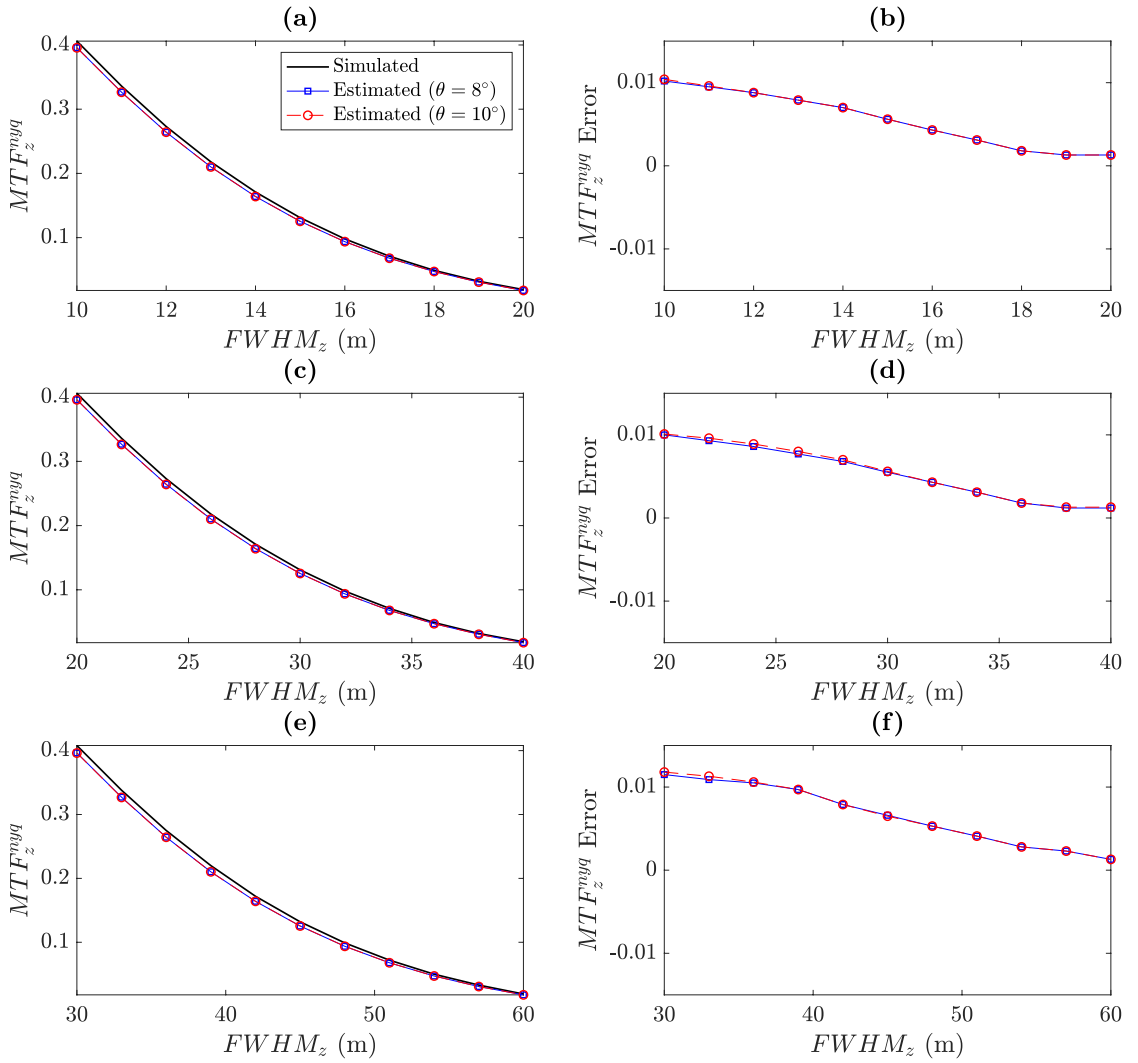

Figure 4.3: Slanted edge algorithm: (a, c, e) estimated MTF_z and (b, d, f) estimation error MTF_e as a function of the simulated resolution $FWHM_z$. (a, b) correspond to $GSD = 10$ m,(c, d) correspond to $GSD = 20$ m, and (e, f) correspond to $GSD = 30$ m.

respectively, as a function of the normalized simulated resolution. Both the estimated $FWHM$ and the estimation error $FWHM_e$ are normalized by the GSD. As shown in the figure, the algorithm achieves a good $FWHM$ estimation, with maximum estimation errors of $0.06GSD$. The spatial accuracy and precision of the algorithm are $\mu_e^{fwhm} = 0.024 \cdot GSD$ (2.4% of the GSD) and $\sigma_e^{fwhm} = 0.018 \cdot GSD$ (1.8% of the GSD).

On the other hand, Figure 4.6 depicts the estimated MTF value at Nyquist frequency and the MTF estimation error at that specific spatial frequency. As can be observed, the algorithm provides good MTF estimation results, with a maximum estimation error of $MTF_e^{nyq} = 0.005$. The MTF estimation accuracy is $\mu_e^{mtf} = 0.0032$, while the precision is $\sigma_e^{mtf} = 0.0014$. Therefore, the pulse target technique provides precision and accuracy values of the same order of magnitude than the slanted edge method for $\theta = 8°$.

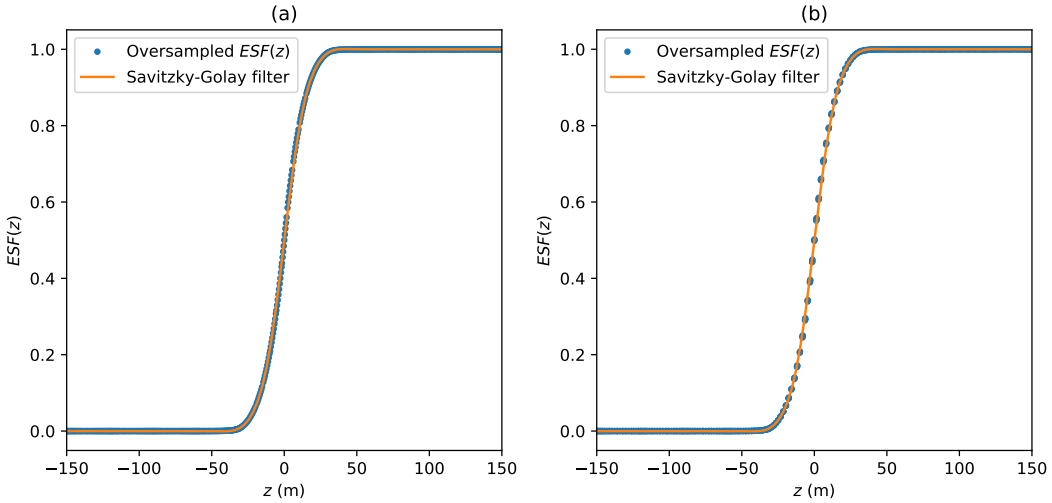

Figure 4.4: (a) ESF interpolation for $\theta = 8°$ and (b) ESF interpolation for $\theta = 10°$. In both cases, $GSD = 30$ m.

θ (°)	GSD (m)	μ_e^{mtf}	σ_e^{mtf}
8	10	0.00553	0.00336
	20	0.00541	0.00330
	30	0.00663	0.00371
10	10	0.00555	0.00340
	20	0.00555	0.00338
	30	0.00669	0.00381

Table 4.2: MTF estimation: accuracy (μ_e^{mtf}) and precision (σ_e^{mtf}) parameters for the different GSD values.

4.1.3 Double-pulse target

Double-pulse target simulations have been performed for a double-pulse considering equal amplitude spans, with widths of $W_z = 0.2 \cdot GSD$ and a separation of $d_z = 0.4 \cdot GSD$. The target inclination is set to $\theta = 8°$. These target dimensions fulfill the conditions established at Equations 3.43 and 3.50, which avoids the estimation error caused by the interference between the Fourier transform of both spans. The simulated PSF resolutions are the same than those used in both slanted edge and pulse target cases. Figures 4.7(a) and 4.7(b) depict the estimated resolution and the estimated resolution error, respectively, as a function of the normalized simulated PSF resolution. Figures 4.8(a) and 4.8(b) represent the estimated MTF^{nyq} values and the MTF estimation errors. As can be observed from both figures, the algorithm provides very similar results to those obtained in the case of pulse target simulations. This result was expected, as the developed algorithm is the same in both cases, and the only difference between the pulse target and double-pulse simulations is the type of input target. Thus, the resolution accuracy and precision are, in this case, $\mu_e^{fwhm} = 0.019 \cdot GSD$ and $\sigma_e^{fwhm} = 0.014 \cdot GSD$, whereas the MTF accuracy and precision are $\mu_e^{mtf} = 0.0033$ and $\sigma_e^{mtf} = 0.0014$.

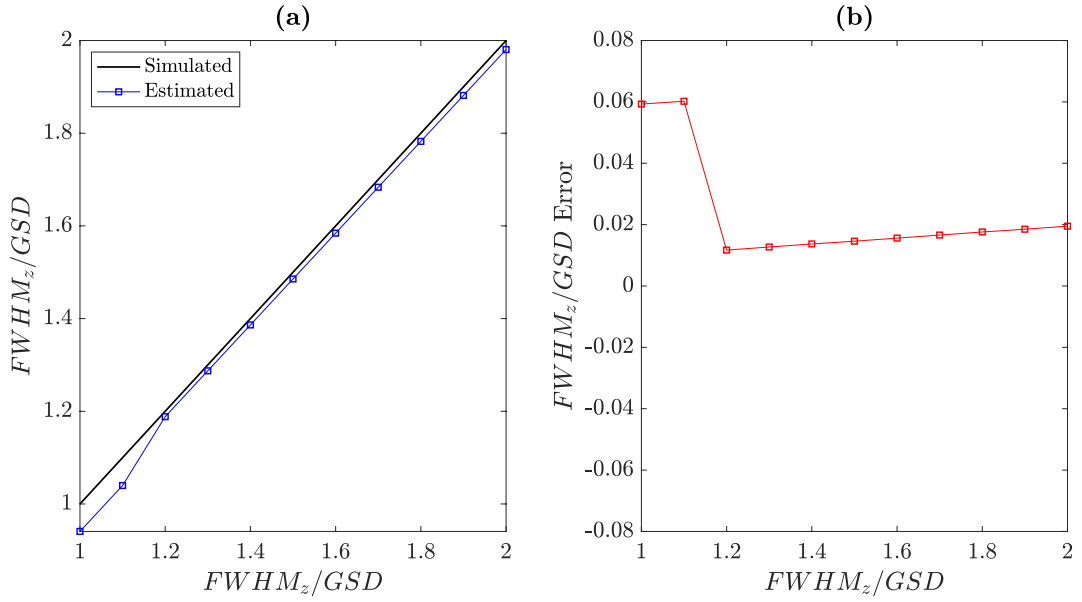

Figure 4.5: Pulse target algorithm: (a) Estimated $FWHM$ normalized by the GSD as a function of the normalized simulated resolution and (b) estimation error as a function of the normalized simulated resolution.

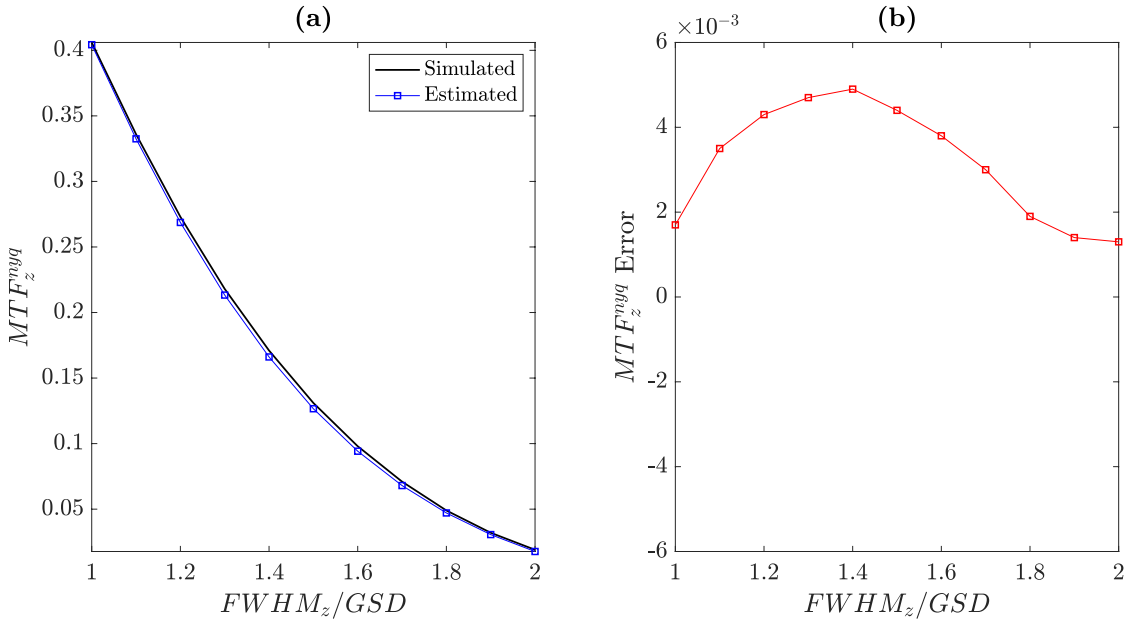

Figure 4.6: Pulse target algorithm: (a) Estimated MTF at Nyquist frequency as a function of the normalized simulated resolution and (b) MTF^{nyq} estimation error as a function of the normalized simulated resolution.

4.1.4 Discussion

Ideal simulation results of the previous section show that, for the same target inclination ($\theta = 8°$), the slanted edge algorithm provides MTF estimation at Nyquist frequency with similar accuracy

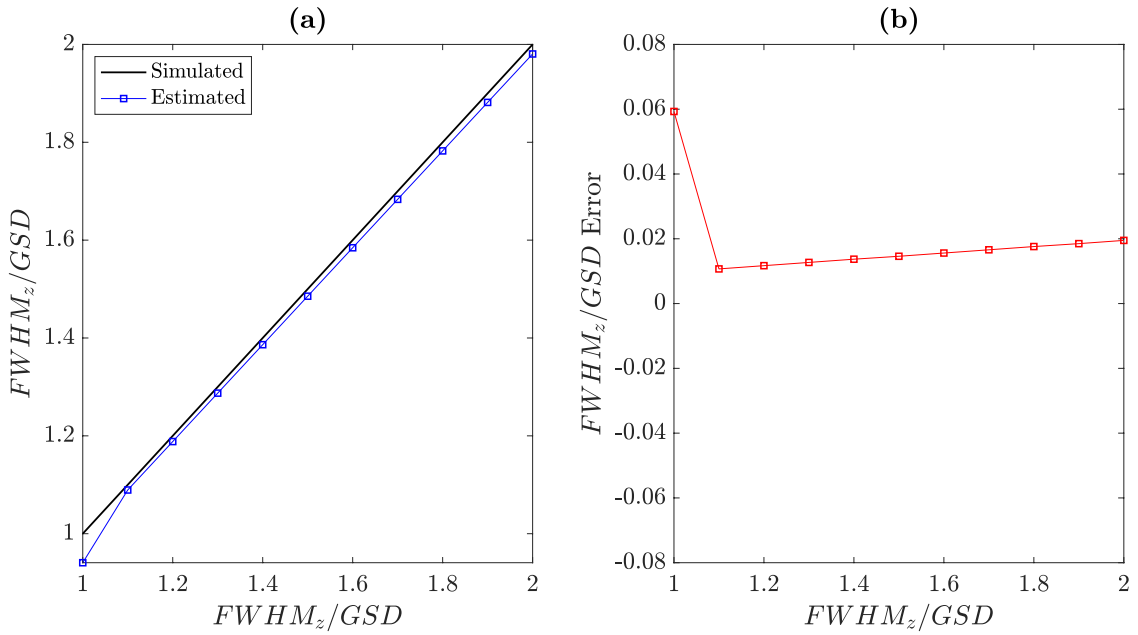

Figure 4.7: Double-pulse algorithm: (a) Estimated $FWHM$ normalized by the GSD as a function of the normalized simulated resolution and (b) estimation error as a function of the normalized simulated resolution.

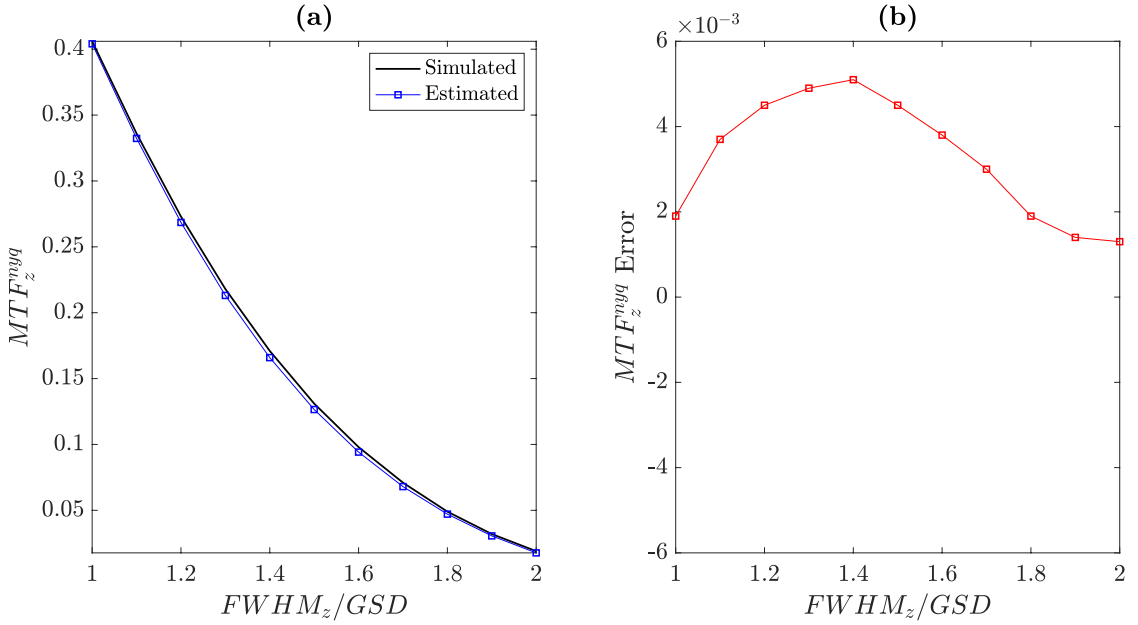

Figure 4.8: Double-pulse algorithm: (a) Estimated MTF at Nyquist frequency as a function of the normalized simulated resolution and (b) MTF^{nyq} estimation error as a function of the normalized simulated resolution.

than the pulse/double-pulse algorithm ($\mu_e^{mtf} = 0.0059$ vs $\mu_e^{mtf} = 0.0032$ and $\mu_e^{mtf} = 0.0033$). However, the slanted edge approach provides more accurate PSF resolution estimations than the

pulse/double-pulse techniques ($\mu_e^{fwhm} = 0.0091 \cdot GSD$ vs $\mu_e^{fwhm} = 0.024 \cdot GSD$ and $\mu_e^{fwhm} = 0.019 \cdot GSD$). Thus, if both sharp contrast edges and pulse targets are present on the spectral image, the slanted edge approach is preferred over the pulse/double-pulse technique, as the slanted edge algorithm does not require any high-resolution image and provides similar estimation performance.

4.2 Real data

Once the algorithm performance was tested using ideal simulations, MTF estimations of real passive optical instruments were carried out. The estimations were performed using one reference dataset from the Committee on Earth Observation Satellites (CEOS), and L1B products from the Earth observation Sentinel-2 mission from the European Space Agency (ESA). The reference dataset is used to validate the algorithm with spectral images obtained using instruments which MTF has been previously characterized by experts. On the other hand, in-flight Sentinel-2 products are used to perform MTF estimations, comparing them to the results reported at the Data Product Quality Reports [25] generated by ESA experts.

4.2.1 Calibration and validation reference dataset

The reference dataset consists on a combination of simulated and real images of slanted edge targets. This dataset is available at the Validation and Calibration portal from the CEOS [26], under the section "MTF Reference Dataset". The dataset was created by a team of researchers and professionals from different parts of the world who deal with MTF measurements, with the objective to create a reference dataset to check the performance of MTF estimation algorithms. The results and methodology used to create the dataset can be found at [14]. The Cal/Val dataset is formed by a total of 6 slanted edge targets, classified from letters A to F. This reference Cal/Val dataset is a blind test. Thus, at the first step, the reference images are downloaded and their corresponding MTF responses are estimated using the developed slanted edge algorithm. Then, the estimation results are uploaded to the Cal/Val website and, once all the results have been uploaded, the MTF reference responses are provided by the Cal/Val site admins, so that the uploaded estimated MTF responses can be compared to the reference responses.

Figure 4.10(a) depicts the across-track MTF estimation results obtained using the "Image A" target of the Cal/Val dataset, compared to the reference MTF response. In this case, only across-track MTF assessment is possible because of the slanted edge orientation (Figure 4.9(a)). On the other hand, Figure 4.10(b) represents the MTF estimation error as a function of the normalized spatial frequency. As can be seen in the figure, the estimated MTF response fits to the reference MTF very well, especially in higher frequencies. The difference between reference and estimated MTF at lower frequencies could be caused by a bad continuous component compensation, among other factors. Figures 4.11, 4.12, 4.13, 4.14, and 4.15 show the estimated MTF responses and the MTF estimation errors for images B, C, D, E, and F, respectively. As shown in the figures, the algorithm achieves a reliable MTF estimation in all cases. In general, the higher estimation error is located at lower spatial frequencies, as in the image A results. It is worth noting that the best estimation result is achieved for the Image D case (Figure 4.13). This fact is a consequence of the algorithm calibration, as the different algorithm parameters (sliding window width, interpolation resolution, Savitzky-Golay polynomial degree, etc.) were tuned using input edges filtered with a gaussian function, which is the PSF type used to filter the slanted edge of Image D. Thus, the

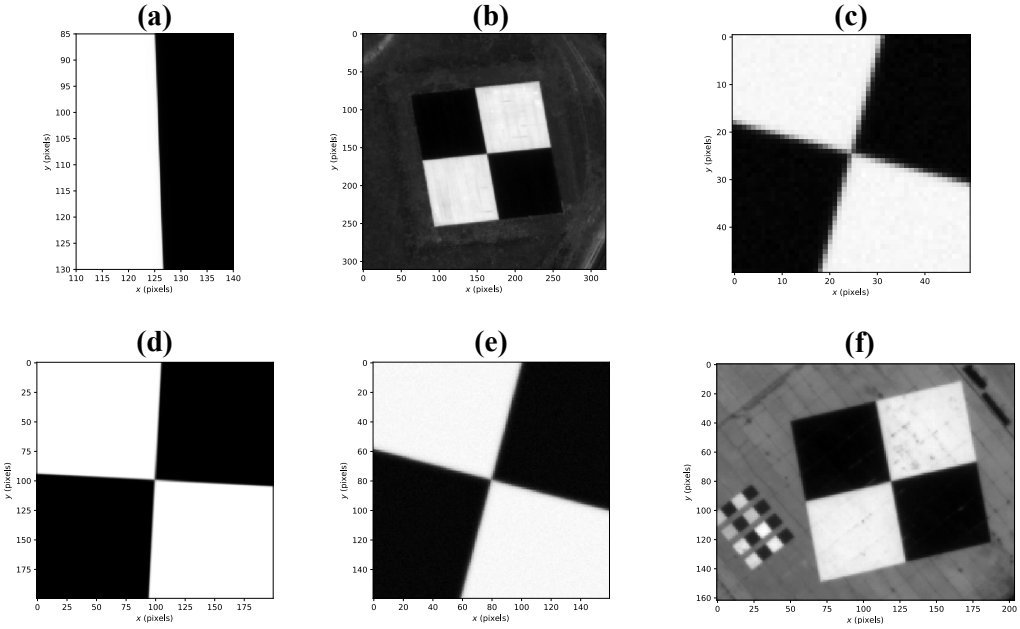

Figure 4.9: Slanted edge targets from the reference Cal/Val dataset: (a) image A, (b) image B, (c) image C, (d) image D, (e) image E, and (f) image F.

tuning process of the different algorithm parameters could yield to a biased estimation of other PSF types, and the algorithm performance may depend on the shape of the MTF response under estimation, which agrees with the results reported in [14].

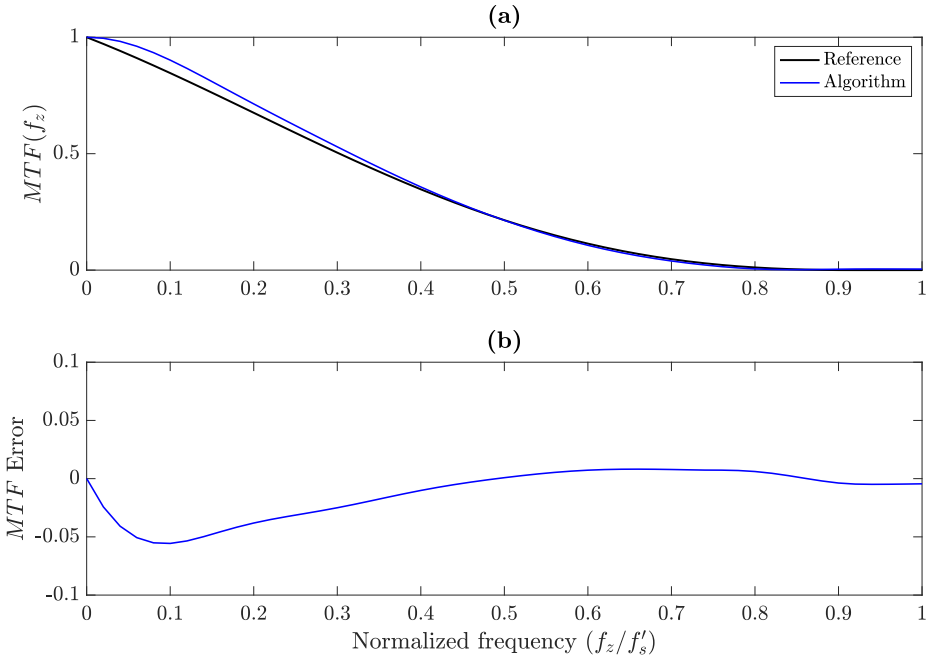

Figure 4.10: Image A: (a) across-track MTF estimation results and (b) across-track MTF estimation error as a function of the normalized spatial frequency.

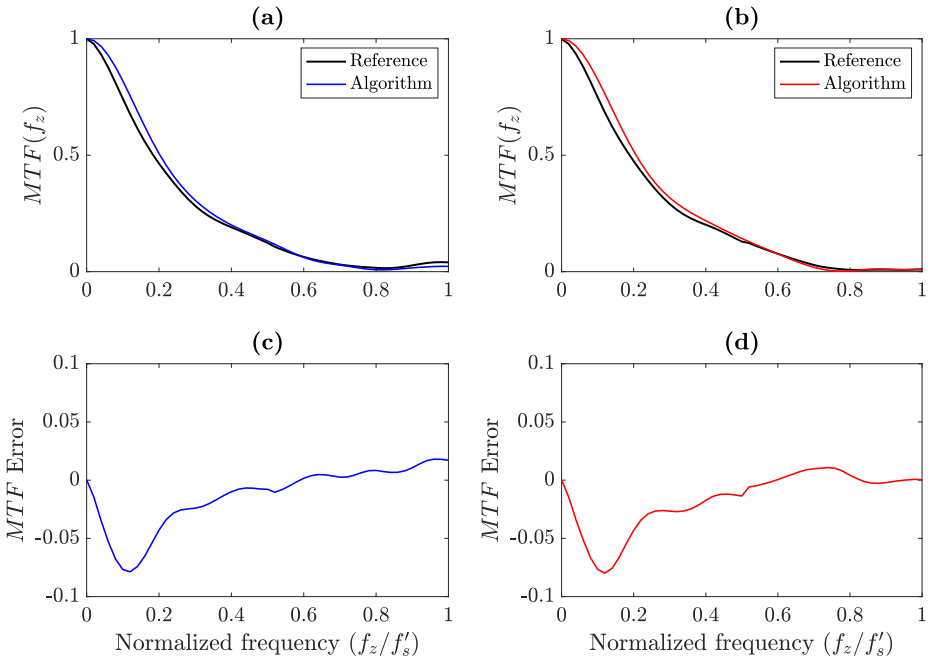

Figure 4.11: Image B: (a) across-track and (b) along-track MTF estimation results. (b) across-track and (d) along-track MTF estimation errors.

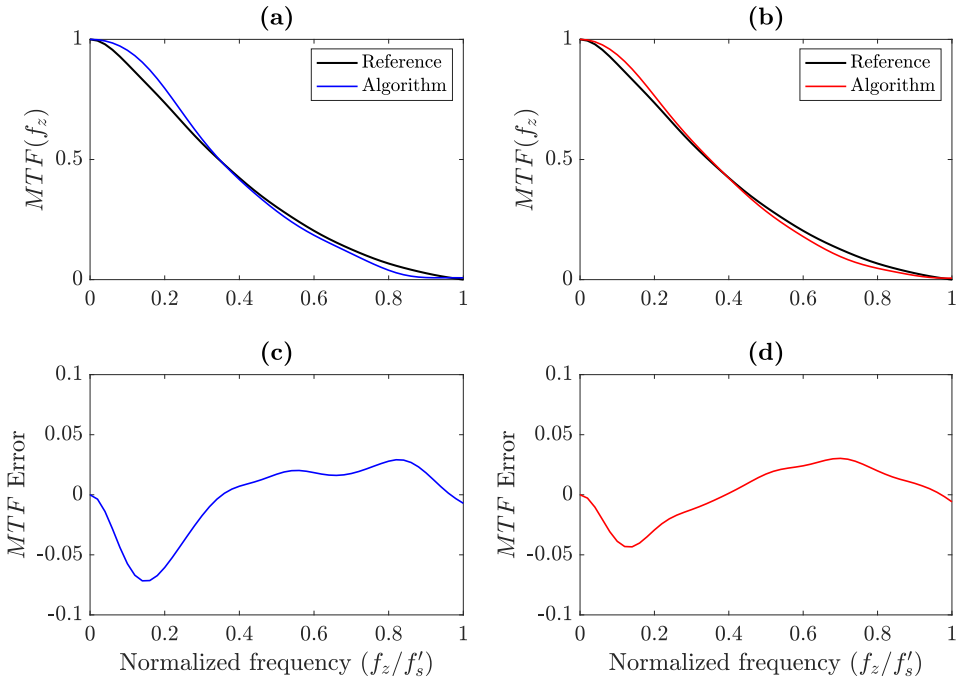

Figure 4.12: Image C: (a) across-track and (b) along-track MTF estimation results. (b) across-track and (d) along-track MTF estimation errors.

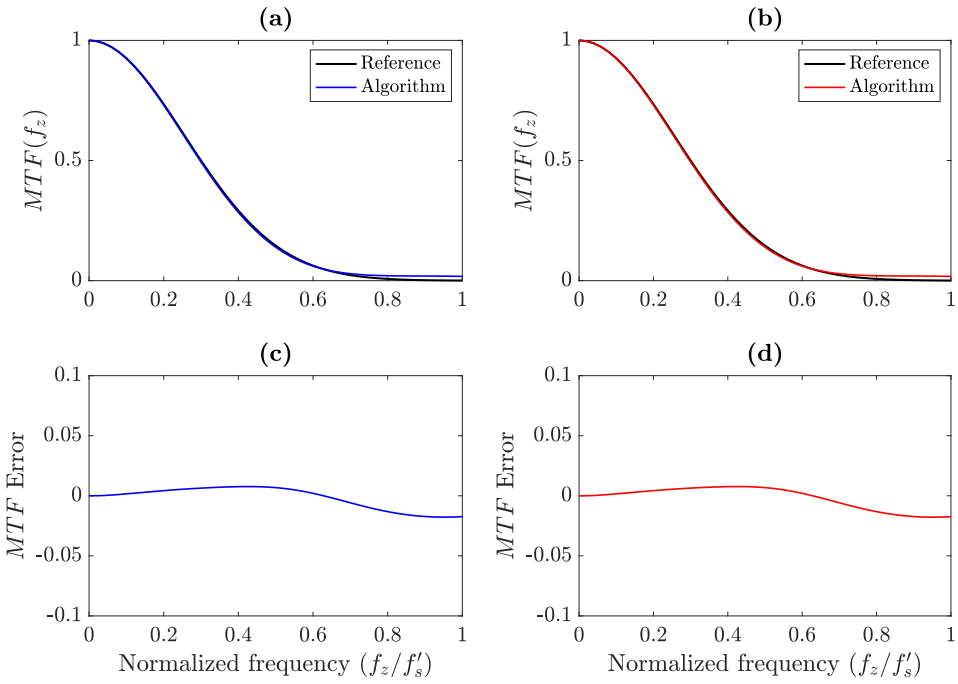

Figure 4.13: Image D: (a) across-track and (b) along-track MTF estimation results. (b) across-track and (d) along-track MTF estimation errors.

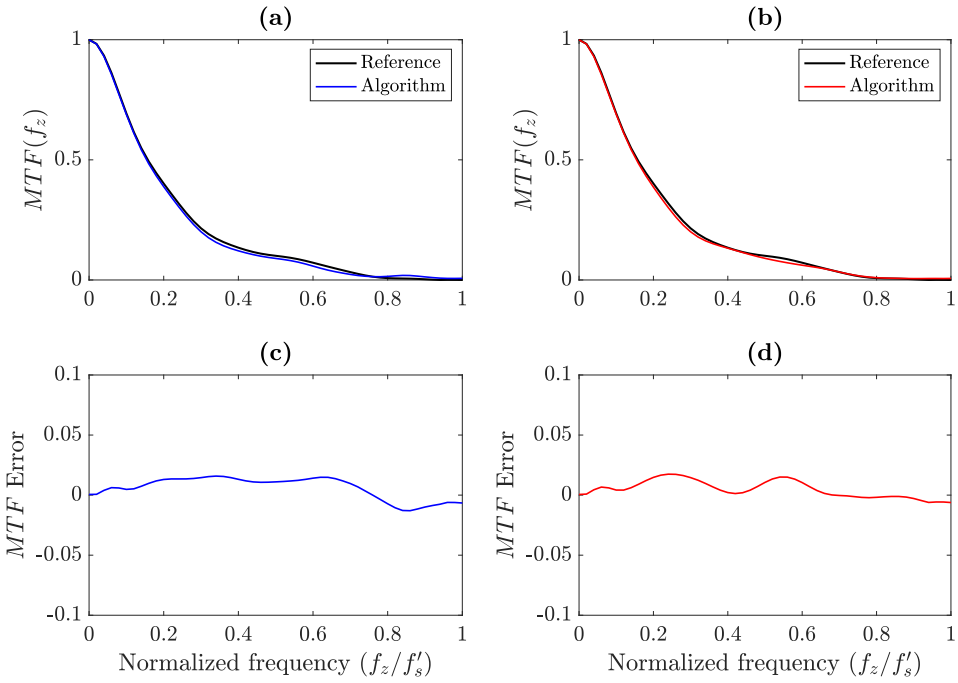

Figure 4.14: Image E: (a) across-track and (b) along-track MTF estimation results. (b) across-track and (d) along-track MTF estimation errors.

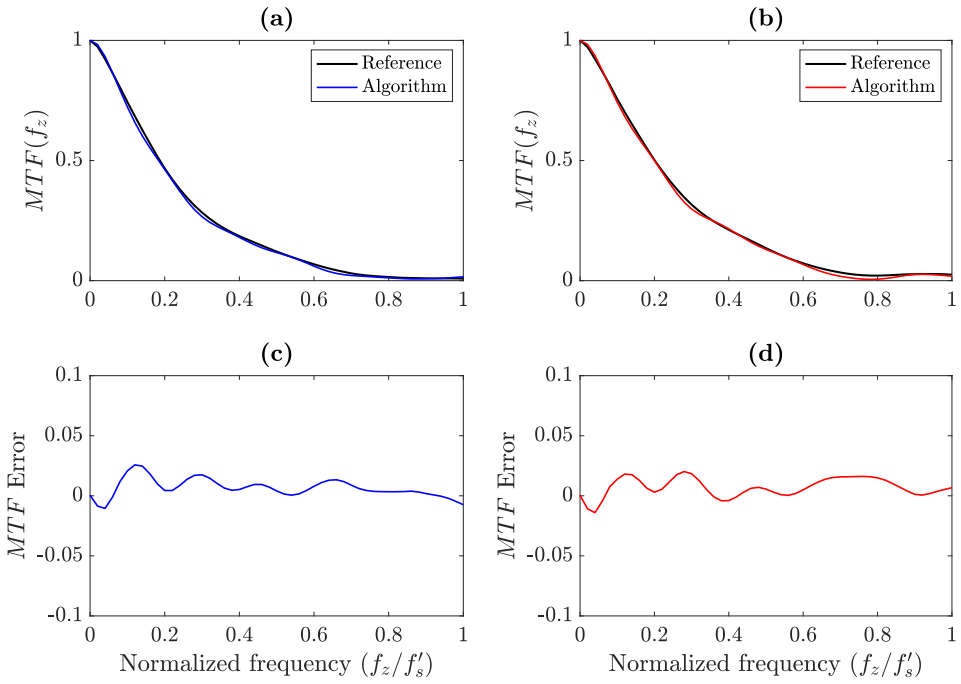

Figure 4.15: Image F: (a) across-track and (b) along-track MTF estimation results. (b) across-track and (d) along-track MTF estimation errors.

4.2.2 Sentinel-2

Sentinel 2 is an Earth observation mission providing high quality spectral images of the Earth's surface with high revisit frequency [27]. This spectral images can be used, for instance, to monitor climate change effects, water content and chlorophyll plant indexes, or forestal areas, among many other applications. The mission consists on two polar-orbiting satellites, Sentinel-2A and Sentinel-2B, each one equipped with a passive optical multispectral instrument (MSI) with a swath width ($GFOV$) of 290 km and a total of 13 spectral bands, ranging from the visible and and VNIR bands to the SWIR band, with different spectral and spatial resolutions. The MSI features 4 high spatial resolution bands with $GSD = 10$ m centered at 490 nm (blue), 560 nm (green), 665 nm (red), and 842 nm (near infrared). In addition, it features 6 narrow spectral bands with $GSD = 20$ m for vegetation characterization at 705, 740, 783, and 865 nm; and two wider SWIR bands at 1610 and 2190 nm for snow, ice, and cloud detection. The MSI also features 3 low spatial resolution bands with $GSD = 60$ m mainly for atmospheric corrections and cloud screening, centered at 443, 945, and 1375 nm. The instrument employs the pushbroom scanning technique. The latitude coverage ranges from $56°$ south to $84°$ north, with 10 days of revisit time at the equator. The first satellite, Sentinel-2A, was launched at 23^{rd} June of 2015, while the second one, Sentinel-2B, was launched at 7^{th} March of 2017. The main specifications for each spectral band of the mission are shown in Table 4.3. In the table, the radiance sensibility column represents the radiance range $L^s_{min} < L^s_{ref} < L^s_{max}$ that the sensor is able to detect, measured in $\text{Wm}^{-2}\text{srad}^{-1}\mu\text{m}^{-1}$.

Sentinel-2 products include L1C and L2A images, available for free at the Copernicus Open Access Hub [28]. L1B products are also available for scientific and professional users under previous request. Usually, the generation of L2A products is on user's side, and can be obtained using

Band	GSD (m)	λ_0 (nm)	$\Delta\lambda$ (nm)	Radiance sensibility range	SNR @ L^s_{ref} (dB)
1	60	443	20	16<129<588	129
2	10	490	65	11.5<128<615.5	154
3	10	560	35	6.5<128<559	168
4	10	665	30	3.5<108<484	142
5	20	705	15	2.5<74.5<449.5	117
6	20	740	15	2<68<413	89
7	20	783	20	1.5<67<387	105
8	10	842	115	1<103<308	174
8a	20	865	20	1<52.5<308	72
9	60	945	20	0.5<9<233	114
10	60	1375	30	0.05<6<45	50
11	20	1610	90	0.5<4<70	100
12	20	2190	180	0.1<1.5<24.5	100

Table 4.3: Sentinel-2 mission specifications for each spectral band.

the SNAP Toolbox [29] and the *sen2cor* algorithm. Thus, the Sentinel-2 mission products are:

- L1B: top of atmosphere radiometrically corrected radiances in sensor geometry.
- L1C: top of atmosphere radiometrically corrected reflectance in a map projection.
- L2A: bottom of atmosphere radiometrically corrected reflectance in a map projection.

The calibration and validation methods of the different satellite parameters can be found at the Sentinel-2 Calibration and Validation Plan for the Operational Phase [30]. The MTF response of the instrument must be performed using L1B products, as L1C products implement geometric corrections that include interpolation and resampling operations that affect the effective MTF and PSF responses. The MTF specifications for both Sentinel-2A and Sentinel-2B satellites are:

- $GSD = 10$ m bands: $0.15 < MTF^{nyq} < 0.3$ (specification S2-MP-045).
- $GSD = 20$ m and $GSD = 60$ m bands: $MTF^{nyq} < 0.45$ (specification S2-MP-045).
- MTF in-orbit stability of 10% during lifetime (specification S2-MP-050).

Sentinel-2 MTF validations are performed once per year by the Mission Performance Centre (MPC) and Expert Support Laboratories (ESL) groups. The validation results are reported at the Data Product Quality Reports [25] as MTF estimations at Nyquist frequency. In order to double check the MTF estimations reported at the Data Product Quality reports, MTF estimations for the high spatial resolution red, green, and blue bands have been performed using the developed slanted edge algorithm. As suggested in the Sentinel-2 Cal/Val plan [30], the selected location to perform the estimation is Maricopa, Arizona, USA. Maricopa has many crop fields slightly slanted respect to the along-track axis, which makes this location a suitable choice to detect contrast edge targets. The $L1B$ product requested to the ESA was acquired with the Sentinel-2A satellite in April 2017, with product ID S2A_MSIL1B_20170405T181441_N0204_R041_20200203T162745. Estimations were performed using the data from detector 2. Figure 4.16(a) depicts an image of the

Band 3 with some Maricopa fields with a red rectangle highlighting the slanted edge used for the estimations, which can be found in more detail at Figure 4.16(b).

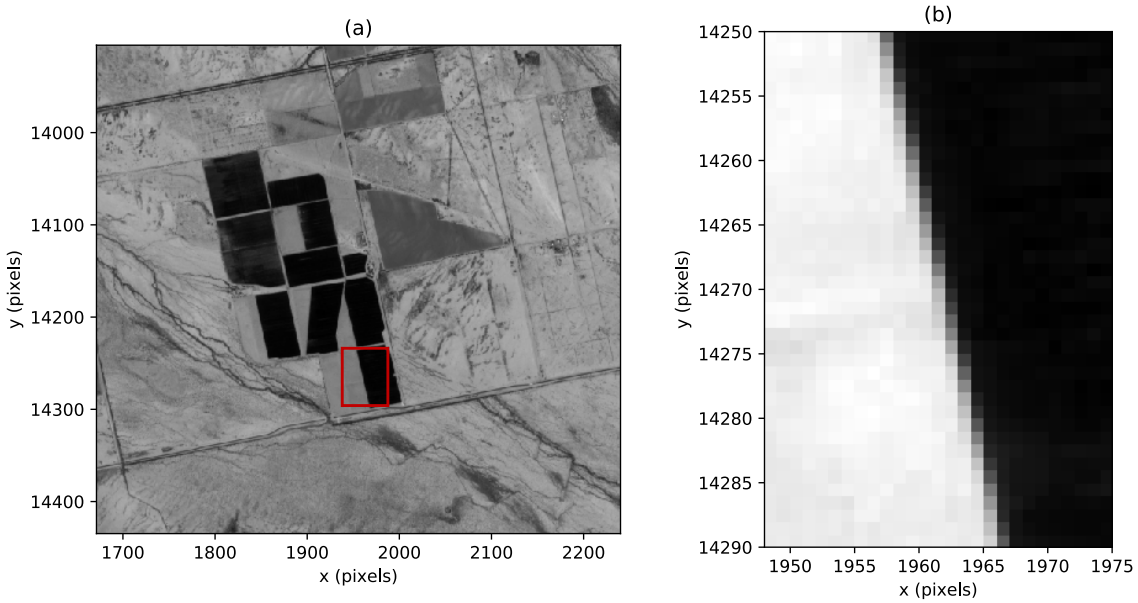

Figure 4.16: (a) Input image from Band 3 of the Detector 2, and (b) sharp edges used to estimate the MTF response.

Figures 4.17(a) and 4.17(b) depict the estimated across-track $ESF(z)$ and $LSF(z)$ profiles, respectively. The $ESF(z)$ has been obtained by interpolating the oversampled $ESF(z)$ profile, created from the combination and projection of the different $ESF_i(z)$ centered using the Fermi function fitting technique. In this case, the estimated inclination of the edge is $\theta = 13.03°$. On the other hand, the $LSF(z)$ was calculated by differentiating the $ESF(z)$. The across-track resolution estimated from the $LSF(z)$ is $FWHM_x = 12.4$ m. Finally, Figure 4.18 shows the MTF response calculated as the Fourier transform of the LSF. As can be observed, in this case the across-track MTF value at Nyquist frequency is $MTF_x^{nyq} = 0.27$

Figure 4.19 depicts the estimation results of high-resolution Bands 2, 3, and 4. All the results have been obtained using images from Detector 2 of the MSI. Figures 4.19(a), 4.19(c), and 4.19(e) correspond to Band 2, 3, and 4 LSF estimations, respectively, while Figures 4.19(b), 4.19(d), and 4.19(f) represent their corresponding MTF responses. Blue lines are for across-track results and red lines are for along-track estimations. As can be observed from the figure, all three bands present similar resolutions and MTF responses, with no significant differences between across-track and along-track responses.

Table 4.4 shows the across and along-track MTF values at Nyquist frequency reported at the Data Product Quality Report of April 2017 with the estimation uncertainty of each estimation for Bands 2, 3, and 4. On the other hand, Table 4.5 show the estimation results of both $FWHM$ and MTF^{nyq} obtained from the LSF and MTF responses depicted in Figure 4.19. As can be observed from the comparison of Tables 4.4 and 4.5, the estimated MTF values at Nyquist frequency obtained using the developed slanted edge algorithm are in good agreement with those reported at the Data Product Quality Report, and fall within the uncertainty range provided by the ESA. In addition, the estimation results also agree with the results presented by the ESA in [31]. The

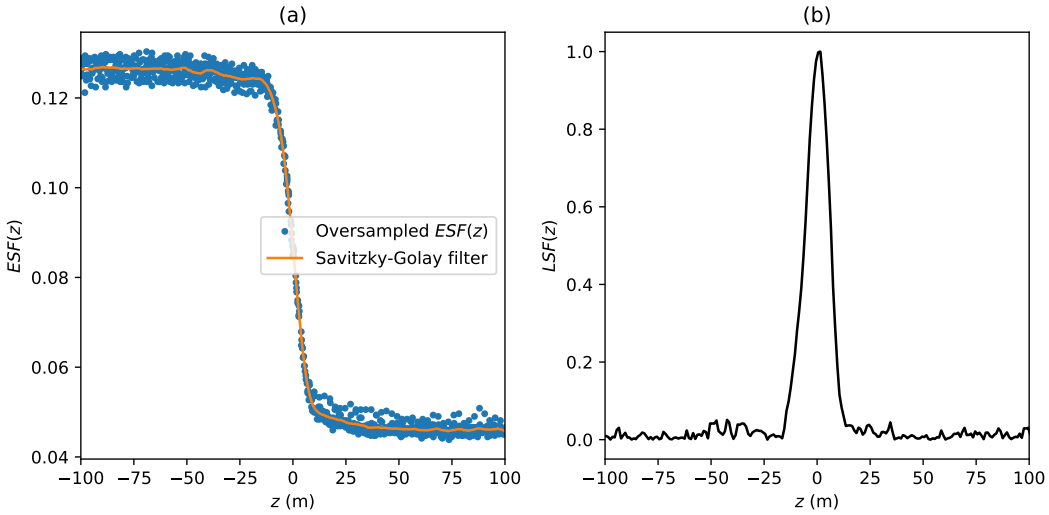

Figure 4.17: (a) oversampled and interpolated $ESF(z)$ across-track profile, and (b) estimated $LSF(z)$.

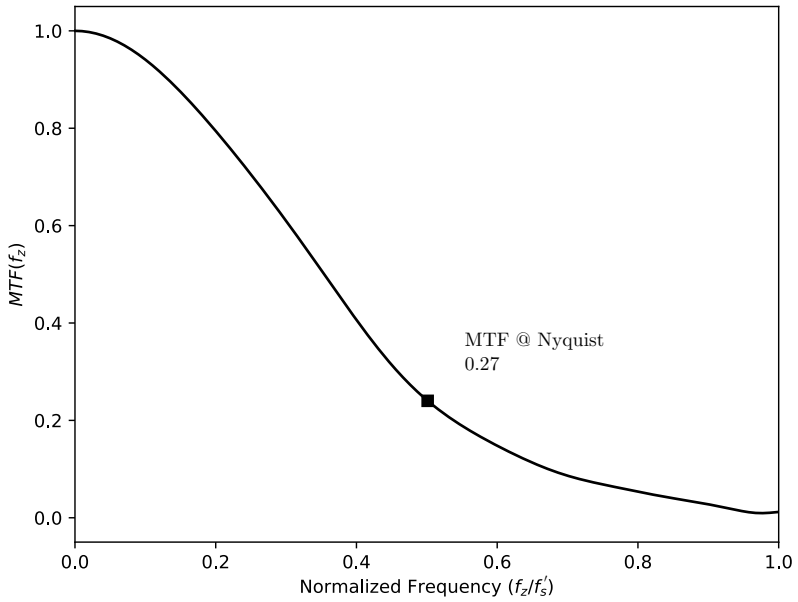

Figure 4.18: Estimated across-track $MTF(f_z)$ response.

estimated resolutions are in the range of $FWHM = 1.2 \cdot GSD$ and $FWHM = 1.3 \cdot GSD$.

4.2.3 L1C vs. L1B products

As mentioned before, MTF estimations must be carried out using L1B and not L1C products. However, it is important to point out that final users employ not L1B, but L1C products, which means that MTF and PSF resolution degradations due to the interpolation and resampling process used to project L1B products onto conventional map coordinates should be considered, as

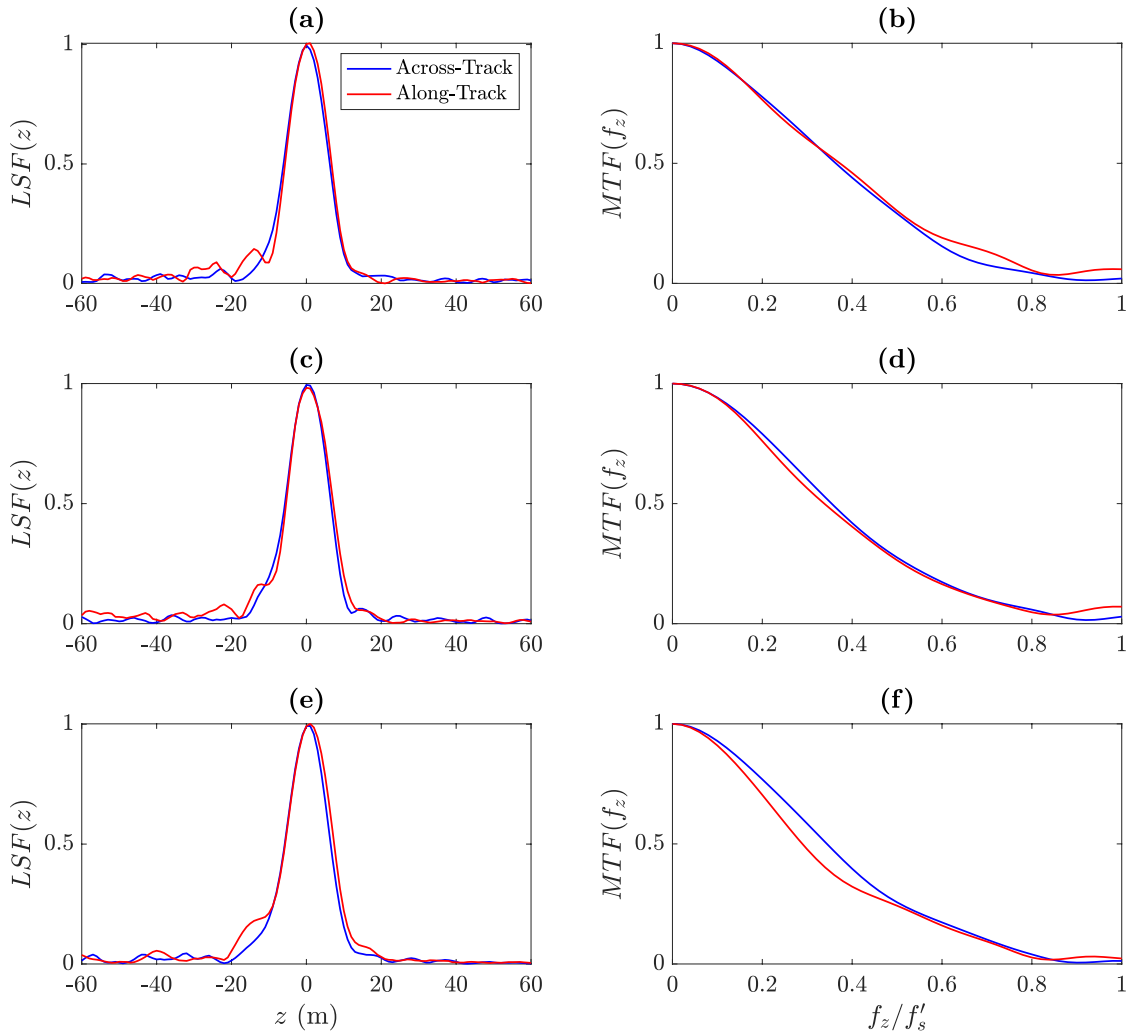

Figure 4.19: (a, c, e) Estimated LSF for Bands 2, 3, and 4, respectively; (b, d, f) MTF responses of Bands 2, 3, and 4, respectively. Blue lines are for across-track results, while red lines are for along-track estimations.

they will be present at final user's products. In order to study this degradation, MTF and LSF estimations of the L1C product associated to the employed L1B product used for the Sentinel-2 assessment have been carried out. The corresponding product ID is:

- S2A_MSIL1C_20170405T181441_N0204_R041_T12SVB_20170405T181440.

Figure 4.20 depicts the estimation results obtained from the L1B image and its associated L1C product, for Band 4. Figures 4.20(a) and 4.20(b) correspond to across-track results, while 4.20(c) and 4.20(d) correspond to along-track estimations. As shown in the figure, there is a noticeable degradation in terms of both resolution and MTF. For the across-track direction, the resolution is reduced from $FWHM_x = 12.4$ m to $FWHM_x = 15.5$ m for the L1B and L1C cases, respectively, while the MTF at Nyquist is reduced from $MTF_x^{nyq} = 0.253$ to $MTF_x^{nyq} = 0.109$. Likewise, for the along-track direction the resolution changes from $FWHM_x = 13.2$ m in the $L1B$

Band	MTF_x^{nyq}	MTF_y^{nyq}
2	0.25±0.06	0.27±0.06
3	0.27±0.03	0.28±0.04
4	0.25±0.04	0.23±0.03

Table 4.4: Sentinel-2: MTF^{nyq} values reported at the Data Product Quality Report from April 2017. Subindex x denotes across-track results, while subindex y denotes along-track values.

Detector	Band	$FWHM_x$ (m)	MTF_x^{nyq}	$FWHM_y$ (m)	MTF_y^{nyq}
2	2	12.5	0.287	12.5	0.298
2	3	12.4	0.272	12.7	0.260
2	4	12.4	0.253	13.2	0.241

Table 4.5: Sentinel-2: MTF^{nyq} and $FWHM$ estimation results for Bands 2, 3, and 4. Subindex x denotes across-track results, while subindex y denotes along-track values.

product, to $FWHM_x = 16.1$ m in the L1C case; while the MTF is degraded from $MTF_x^{nyq} = 0.241$ to $MTF_x^{nyq} = 0.103$.

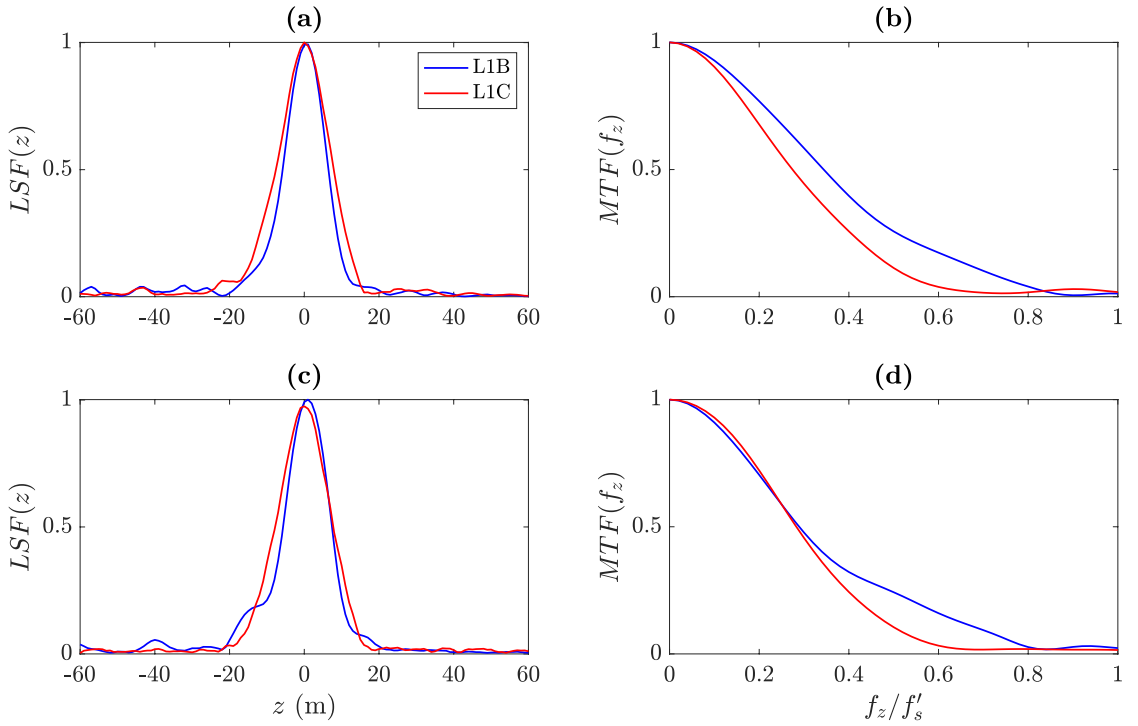

Figure 4.20: (a) Estimated across-track LSF and (b) its corresponding MTF, (c) estimated along-track LSF and (d) its corresponding MTF. Blue lines are for $L1B$ results, while red lines are for $L1C$ estimations.

Therefore, the MTF degradation due to the interpolation and resampling process applied to

$L1B$ products should be considered when analyzing the spatial performance of the optical instrument, as it plays an important role on the final MTF response of $L1C$ products delivered to final users.

Chapter 5

Conclusions

In this master thesis, two algorithms to perform estimations of the modulation transfer function (MTF) of passive optical instruments have been developed. The MTF represents the instrument response as a function of the spatial frequency. Thus, it relates the input amplitude of a given spatial frequency component with its output amplitude. The MTF of an instrument is usually characterized in the literature by its value at the Nyquist frequency. As explained in previous chapters, spatial frequencies higher than the Nyquist frequency will translate onto aliasing artifacts at the final image. Thus, ideally, a low MTF value at this frequency should be required. However, a narrower MTF response translates in the spatial domain onto a wider point spread function (PSF), which means that the spatial resolution decreases. Therefore, the estimation of the MTF response is an important task to assess the spatial quality of satellite images.

The implemented algorithms are able to estimate the MTF using in-flight spectral images. Both algorithms are developed in Python with Open Source libraries, and implement two different MTF estimation techniques: the slanted edge method, and the pulse/double-pulse target method. The estimation results obtained with the two methods have been compared, showing similar results. However, in general, the slanted edge approach is preferred over the pulse/double-pulse target method, as it avoids MTF estimation errors due to the target dimensions and it does not require a high-resolution model of the target. The performance of the algorithms has been analyzed using both ideal simulations and real data, with good accuracy and precision values. Sentinel-2 MTF assessments are presented, which are in good agreement with the MTF values reported by the ESA calibration and validation teams. Finally, the image degradation on spatial quality due to the interpolation and resampling process used to obtain L1C products from L1C data of Sentinel-2 images is discussed.

Further improvements of the developed algorithms could be implemented in future work. For instance, automatic slanted edge or pulse/double-pulse target detection could improve the usability of the algorithms, as on its current version the target detection has to be configured manually. Additional estimation methods could also be implemented, as, for instance, the frequency method developed by ONERA at [12, 14]. Increasing the number of estimation methods can improve significantly the robustness of the estimation results. Finally, the developed algorithms could be adapted so that the could be included as a plug-in in the SNAP Toolbox of the ESA, allowing final users to estimate the spatial quality of Sentinel-2 spectral images.

References

[1] Robert Schowengerdt. *Remote Sensing: Models and Methods for Image Processing*. 2nd Editio. Academic Press, 1997. ISBN: 0-12-628981-6.

[2] Arthur P. Cracknell and Ladson Hayes. *Introduction to Remote Sensing*. 2nd Editio. CRC Press, 2007. ISBN: 0-8493-9255-1.

[3] NASA. *Landsat 1*. URL: https://landsat.gsfc.nasa.gov/landsat-1/.

[4] Alexander F.H. Goetz et al. "Imaging Spectrometry for Earth Remote Sensing". In: *Science* 228.4704 (June 1985), pp. 1147–1153. ISSN: 0036-8075. DOI: 10.1126/science.228.4704.1147. URL: http://www.sciencemag.org/cgi/doi/10.1126/science.228.4704.1147.

[5] Hsien-Wei Chen and Ke-Sheng Cheng. "A Conceptual Model of Surface Reflectance Estimation for Satellite Remote Sensing Images Using in situ Reference Data". In: *Remote Sensing* 4.4 (Mar. 2012), pp. 934–949. ISSN: 2072-4292. DOI: 10.3390/rs4040934. URL: http://www.mdpi.com/2072-4292/4/4/934.

[6] Luis Guanter. "New algorithms for atmospheric correction and retrieval of biophysical parameters in Earth Observation. Application to ENVISAT/MERIS data." PhD thesis. Universitat de València, 2006.

[7] Earth and Mission Science Division. *Copernicus Hyperspectral Imaging Mission for the Environment - Mission Requirements Document*. Tech. rep. 2019. URL: http://esamultimedia.esa.int/docs/EarthObservation/Copernicus%7B%5C_%7DCHIME%7B%5C_%7DMRD%7B%5C_%7Dv2.1%7B%5C_%7DIssued20190723.pdf.

[8] Karl Segl et al. "Simulation of Spatial Sensor Characteristics in the Context of the EnMAP Hyperspectral Mission". In: *IEEE Transactions on Geoscience and Remote Sensing* 48.7 (July 2010), pp. 3046–3054. ISSN: 0196-2892. DOI: 10.1109/TGRS.2010.2042455. URL: http://ieeexplore.ieee.org/document/5446369/.

[9] S.E. Reichenbach, D.E. Koehler, and D.W. Strelow. "Restoration and reconstruction of AVHRR images". In: *IEEE Transactions on Geoscience and Remote Sensing* 33.4 (July 1995), pp. 997–1007. ISSN: 01962892. DOI: 10.1109/36.406685. URL: http://ieeexplore.ieee.org/document/406685/.

[10] Taeyoung Choi and Dennis L Helder. "Generic Sensor Modeling for Modulation Transfer Function (MTF) Estimation". In: *Pecora 16 "Global Priorities in Land Remote Sensing" October 23 – 27, 2005 * Sioux Falls, South Dakota* (2005).

[11] ISO12233. *Photography — Electronic still picture imaging — Resolution and spatial frequency responses*. Tech. rep. International Organization for Standardization, 2017.

[12] Françoise Viallefont-Robinet and Dominique Léger. “Improvement of the edge method for on-orbit MTF measurement”. In: *Optics Express* 18.4 (Feb. 2010), p. 3531. ISSN: 1094-4087. DOI: 10.1364/OE.18.003531. URL: https://www.osapublishing.org/oe/abstract.cfm?uri=oe-18-4-3531.

[13] Taeyoung Choi, Xiaoxiong Xiong, and Zhipeng Wang. “On-Orbit Lunar Modulation Transfer Function Measurements for the Moderate Resolution Imaging Spectroradiometer”. In: *IEEE Transactions on Geoscience and Remote Sensing* 52.1 (Jan. 2014), pp. 270–277. ISSN: 0196-2892. DOI: 10.1109/TGRS.2013.2238545. URL: http://ieeexplore.ieee.org/document/6471199/.

[14] Françoise Viallefont-Robinet et al. “Comparison of MTF measurements using edge method: towards reference data set”. In: *Optics Express* 26.26 (Dec. 2018), p. 33625. ISSN: 1094-4087. DOI: 10.1364/OE.26.033625. URL: https://www.osapublishing.org/abstract.cfm?URI=oe-26-26-33625.

[15] P. Blanc and L. Wald. “A review of earth-viewing methods for in-flight assessment of modulation transfer function and noise of optical spaceborne sensors”. In: *Working Paper* (2009). URL: https://hal-mines-paristech.archives-ouvertes.fr/hal-00745076.

[16] Robert Schowengerdt, Charnchai Archwamety, and Robert C. Wrigley. “Operational MTF for Landsat Thematic Mapper”. In: *Image Quality: An Overview*. Ed. by Lionel R. Baker and Edward M. Granger. July 1985, p. 110. DOI: 10.1117/12.948812. URL: http://proceedings.spiedigitallibrary.org/proceeding.aspx?doi=10.1117/12.948812.

[17] James C. Storey. “Landsat 7 on-orbit modulation transfer function estimation”. In: *Sensors, Systems, and Next-Generation Satellites V*. Ed. by Hiroyuki Fujisada, Joan B. Lurie, and Konradin Weber. Dec. 2001, p. 50. DOI: 10.1117/12.450647. URL: http://proceedings.spiedigitallibrary.org/proceeding.aspx?doi=10.1117/12.450647.

[18] Claire Thomas and Lucien Wald. “A MTF-Based Distance for the Assessment of Geometrical Quality of Fused Products”. In: *2006 9th International Conference on Information Fusion*. IEEE, July 2006, pp. 1–7. ISBN: 1-4244-0953-5. DOI: 10.1109/ICIF.2006.301687. URL: http://ieeexplore.ieee.org/document/4085973/.

[19] Python. *Python 3.6.6*. URL: https://www.python.org/downloads/release/python-366/ (visited on 02/17/2020).

[20] Anaconda. *Anaconda Documentation*. (Visited on 02/17/2020).

[21] Numpy. *Numpy Documentation*. URL: https://numpy.org (visited on 02/17/2020).

[22] Scipy. *SciPy Documentation*. URL: https://www.scipy.org (visited on 02/17/2020).

[23] Matplotlib. *Matplotlib Documentation*. URL: https://matplotlib.org/ (visited on 02/17/2020).

[24] Spectral. *Spectral Python Documentation*. URL: http://www.spectralpython.net/index.html (visited on 02/17/2020).

[25] ESA. *Data Product Quality Reports*. URL: https://sentinels.copernicus.eu/web/sentinel/data-product-quality-reports.

[26] CEOS. *MTF Reference Dataset*. URL: http://calvalportal.ceos.org/mtf-reference-dataset.

[27] ESA. *Sentinel-2 mission*. URL: https://sentinel.esa.int/web/sentinel/missions/sentinel-2.

[28] ESA. *Copernicus Open Access Hub*. URL: https://scihub.copernicus.eu.

[29] ESA. *SNAP Toolbox*. URL: https://step.esa.int/main/toolboxes/snap/.

[30] Sentinel-2 PDGS Project Team. *Sentinel-2 Calibration and Validation Plan for the Operational Phase*. Tech. rep. 2014.

[31] Ferran Gascon et al. "Copernicus Sentinel-2A Calibration and Products Validation Status". In: *Remote Sensing* 9.6 (June 2017), p. 584. ISSN: 2072-4292. DOI: 10.3390/rs9060584. URL: http://www.mdpi.com/2072-4292/9/6/584.